

## APPROVAL SHEET

Title of Dissertation: Development and Characterization of a Dither-Based Super-Resolution Reconstruction Method for Fiber Imaging Arrays

Name of Candidate: Eric Robert Languirand  
Doctorate of Philosophy, 2017

Dissertation and Abstract Approved: \_\_\_\_\_  
Dr. Brian M. Cullum  
Associate Professor  
Department of Chemistry and Biochemistry

Date Approved: \_\_\_\_\_

## ABSTRACT

Title of Document:

### DEVELOPMENT AND CHARACTERIZATION OF A DITHER- BASED SUPER-RESOLUTION RECONSTRUCTION METHOD FOR FIBER IMAGING ARRAYS

Eric Robert Languirand, Ph.D. Chemistry, 2017

Directed By:

Dr. Brian M. Cullum, Associate Professor,  
Department of Chemistry and Biochemistry

Abstract:

Chemical imaging is an important tool for providing insight into function, role, and spatial distribution of analytes. This thesis describes the use of imaging fiber bundles (IFB) for super-resolution reconstruction using surface enhanced Raman scattering (SERS) showing improvement in resolution with arrayed bundles for the first time. Additionally this thesis describes characteristics of the IFB with regards to cross-talk as a function of aperture size.

The first part of this thesis characterizes the IFB for both tapered and untapered bundles in terms of cross-talk. Cross-talk is defined as the amount of light leaking from a central fiber element in the imaging fiber bundle to surrounding fiber elements. To make this measurement ubiquitous for all imaging bundles, quantum dots were employed. Untapered and tapered IFB possess cross-talk of 2% or less, with fiber elements down to 32nm.

The second part of this thesis employs a super resolution reconstruction algorithm using projection onto convex sets for resolution improvement. When using IFB arrays, the point spread function (PSF) of the array can be known accurately if the fiber elements over fill the pixel detector array. Therefore, the use of the known PSF compared to a general blurring kernel was evaluated. Relative increases in resolution of 12% and 2% at the 95% confidence level are found, when compared to a reference image, for the general blurring kernel and PSF, respectively.

The third part of this thesis shows for the first time the use of SERS with a dithered IFB array coupled with super-resolution reconstruction. The resolution improvement across a step-edge is shown to be approximately 20% when compared to a reference image. This provides an additional means of increasing the resolution of fiber bundles beyond that of just tapering. Furthermore, this provides a new avenue for nanoscale imaging using these bundles.

Lastly, synthetic data with varying degrees of signal-to-noise (S/N) were employed to explore the relationship S/N has with the reconstruction process. It is generally shown that increasing the number images used in the reconstruction process and increasing the S/N will improve the reconstruction providing larger increases in resolution.

DEVELOPMENT AND CHARACTERIZATION OF A DITHER-BASED SUPER-  
RESOLUTION RECONSTRUCTION METHOD FOR FIBER IMAGING ARRAYS

By

Eric Robert Languirand

Dissertation submitted to the Faculty of the Graduate School of the  
University of Maryland, Baltimore County, in partial fulfillment  
of the requirements for the degree of  
Ph.D. in Chemistry

© Copyright by

Eric Robert Languirand

2017



## Dedication

This thesis is dedicated to my daughter, Lauren. Your unconditional love and wonder provide more inspiration than anyone could ask for. And to my wife, Courtney. Your love and support on this journey together has made it all possible.

## Acknowledgements

I would like to express my gratitude to my research advisor, Dr. Brian Cullum, for his encouragement, guidance, and thoughtful inquiries for which this research was possible. Our many conversations, his helpful insights, and the freedom provided to pursue research of personal interest has pushed me to grow as an independent scientist, for which I am extremely thankful for. I would like to thank the rest of my committee, Dr. Ryan White, Dr. Lisa Kelly, Dr. Songon An, and Dr. Yordan Kostov for their helpful discussions, insights, and perspectives on my research project.

My gratitude to the Cullum Lab members past and present. Specifically, Dr. Sudhir Dahal for your early friendship and guidance in this program. Dr. Pietro Strobbia, for your friendship that you and your family have provided and many long conversations ranging from specific research questions to existential questions of being. And to the new members, Dan Kazal and Steven Lowery for helping me hone my explanation of my research and for good BBQ.

My gratitude to my friends and family for their constant encouragement, which is always inspirational. My mother and father who have continuously supported and encouraged me to become the person I wanted to be. My brother, for his thoughtful conversations with me and his encouragement.

Lastly and most importantly, my gratitude for my wife and daughter is inexpressible. Their love and support is a continuous source of hope, encouragement, and inspiration to be the best husband, best father, and best person I can possibly be.



## Table of Contents

Chapter 1: Introduction to Chemical Based Imaging	1
1.1 Introduction.....	1
1.2 Chemical Imaging.....	1
1.2.1 Raster Scanning .....	4
1.2.2 Hyper- and multispectral imaging .....	5
1.2.3 Spatial Resolution .....	8
1.2.3 Electronic-transition based imaging.....	11
1.2.3.1 Fluorescence .....	11
1.2.3.2 Absorption based imaging .....	14
1.3 Vibrational-transition based imaging.....	15
1.3.1 Infrared Absorption .....	15
1.3.2 Raman .....	16
1.4 Surface Enhanced Techniques .....	18
1.4.1 Surface Enhanced Raman Scatter.....	20
1.5 Super resolution chemical imaging.....	22
1.5.1 Fluorescence-based Super Resolution Chemical Imaging .....	22
1.5.2 Vibrational super-resolution chemical imaging .....	24
1.5.1.1 Structured illumination for Raman based SRCI .....	24
1.5.1.2 Tip-enhanced methods .....	25

1.5.1.3 SERS.....	26
1.6 Conclusion .....	28
 Chapter 2: Optical Cross Talk 44	
2.1. Introduction.....	44
2.2. Experimental .....	48
2.2.1 Fiber Bundle Preparation.....	48
2.2.2 Quantum Dots .....	49
2.2.3 Spectroscopy System .....	50
2.2.4 Microscopic Imaging System .....	51
2.3. Results and Discussion .....	51
2.3.1 Quantum Dot Loading .....	51
2.3.2 Cross-talk evaluation .....	53
2.3.2.1 Untapered Fiber Bundles.....	53
2.3.2.2 – Tapered Fiber Bundles .....	58
2.4. Conclusion .....	63
2.5. Acknowledgments.....	63
 Chapter 3: Super-Resolution Reconstruction with a Magnified Fiber Imaging Bundle 67	
3.1 Introduction.....	67
3.1.1 Image Registration.....	69
3.1.2 Image Interpolation .....	71

3.1.3 <i>Image reconstruction</i> .....	71
3.1.4 <i>The POCS Algorithm</i> .....	73
3.2 <i>Materials and Methods</i> .....	74
3.2.1 <i>Fiber bundle Preparation</i> .....	74
3.2.2 <i>Imaging System</i> .....	74
3.2.3 <i>Data Processing</i> .....	76
3.3 <i>Results and Discussion</i> .....	76
3.3.1 <i>Translational Calibration</i> .....	76
3.3.2 <i>Point Spread Function</i> .....	78
3.3.3 <i>Reconstruction</i> .....	80
3.3.3.1 <i>Standard blurring kernel</i> .....	80
3.3.3.2 <i>Custom Blurring Kernel</i> .....	85
3.4 <i>Conclusions</i> .....	85
Chapter 4: Surface Enhanced Raman Based Dithering	90
4.1 <i>Introduction</i> .....	90
4.2 <i>Materials and Methods</i> .....	93
4.2.1 <i>Fiber Bundle Preparation</i> .....	93
4.2.2 <i>Substrate Preparation</i> .....	94
4.2.2.1 <i>Slide Preparation</i> .....	94
4.2.2.2 <i>Microsphere Preparation</i> .....	95

4.2.2.3 <i>Physical Vapor Deposition</i> .....	95
4.2.2.4 <i>Pattern Formation and Analyte Incubation</i> .....	96
4.2.3 <i>Instrumental Arrangement</i> .....	96
4.2.5 <i>Data Processing</i> .....	98
4.3 <i>Results and Discussion</i> .....	100
4.3.1 <i>Translational Calibration</i> .....	100
4.3.2 <i>Substrate Analysis</i> .....	101
4.3.3 <i>Reconstruction Analysis</i> .....	101
4.3.4 <i>Signal-to-noise Limitations to Image Reconstruction</i> .....	108
4.4 <i>Conclusions</i> .....	113
Chapter 5: Concluding Remarks	118
5 Conclusion .....	118
Appendix A: Physical Vapor Deposition	121
Appendix B: Sutter P-2000 Instrument and Tapering	121
Appendix C: POCS Algorithm	126
Bibliography	144

## List of Tables

Table 2.1: Cross-talk.....	57
Table 4.1: Translations for SERS dithering.....	104
Table A1: Multiline program for tapering .....	122

## List of Figures

Figure 1.1: The electromagnetic spectrum.....	3
Figure 1.2: Types of chemical imaging .....	4
Figure 1.3: Pictorial representation of an AOTF .....	6
Figure 1.4: Pictorial representation of an LCTF.....	7
Figure 1.5: Description of spatial resolution.....	9
Figure 1.6: Partial Jablonski diagram .....	12
Figure 1.7: Surface enhanced techniques.....	19
Figure 2.1: Cross-talk measurement .....	46
Figure 2.2: Imaging and spectroscopy arrangements .....	50
Figure 2.3: Luminescence of quantum dots.....	53
Figure 2.4: Cross-talk ROI selection .....	54
Figure 2.5: Example of cross-talk.....	55
Figure 2.6: Optical image of a tapered bundle.....	59
Figure 3.1: Flow chart of super-resolution reconstruction.....	69
Figure 3.2: Pictorial example of dithering for reconstruction.....	70
Figure 3.3: Optical arrangement for dithering study .....	75
Figure 3.4: Translational Calibration.....	77
Figure 3.5: PSF acquisition.....	79

Figure 3.6: Blurring kernels used.....	81
Figure 3.7: Increased resolution through dithering.....	83
Figure 4.1: Schematic of substrate preparation.....	94
Figure 4.2: Optical arrangement for SERS dithering study.....	97
Figure 4.3: SERS chemical image used in dithering .....	102
Figure 4.4: Low and high resolution threshold chemical images .....	104
Figure 4.5: Cross-sectional line profile.....	105
Figure 4.6: Sigmoidal fitting.....	106
Figure 4.7: Gaussian fitting.....	107
Figure 4.8: High to low profile comparisons .....	108
Figure 4.9: Signal-to-noise synthetic and reconstructed data .....	110
Figure 4.10: Signal-to-noise reconstructed .....	112
Figure A1: Pictorial representation of micropipette puller .....	123
Figure B1: Pictorial representation of the PVD .....	124
Figure B2: Circuit diagram for rotating motor .....	125
Figure C1: AOTF Reproducibility .....	127
Figure C2: Spectrally resolved HgAr Peak with AOTF .....	128
Figure C3: Gaussian fit for spectral resolution .....	130
Figure C4: Spectral resolution .....	131

Figure C5: Spectral response curve .....	132
--	-----



## **Chapter 1: Introduction to Chemical Based Imaging**

### **1.1 Introduction**

Since the late nineteenth century, the light microscope has provided a visual representation of objects that are not seen by the naked eye.<sup>1</sup> Understanding the spatial orientation of components within a sample can glean insight into function, role, or physical characteristics. As such, determining the spatial orientation and concentrations of chemicals have far-reaching effects from biomedical inquiries to issues of national security.<sup>2</sup>

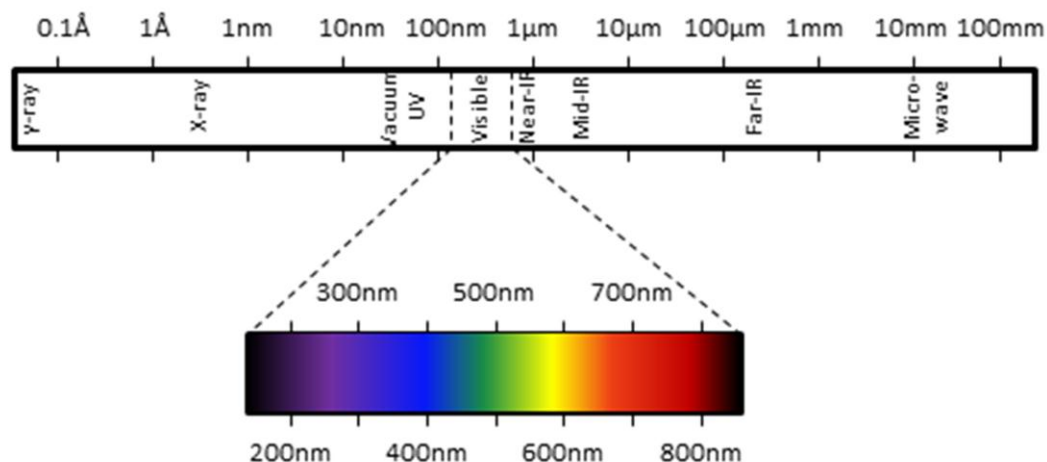
The goal of this introductory chapter is to provide first an overview of imaging. Secondly, this chapter is to provide insight into what goes into the digital acquisition of chemical information. Lastly, this chapter discusses chemical-specific imaging as it primarily pertains to the spectroscopic investigation of the molecules providing a fingerprint of the species being imaged.

### **1.2 Chemical Imaging**

The combination of microscopy and spectroscopy can provide chemical specific information. When combining the two, a two-dimensional chemical representation of the sample can be obtained when imaged with a camera (a charged coupled device (CCD) or complementary metal oxide semiconductor (CMOS)) with contrasting picture elements called pixels. A single picture element is a semiconductor that uses the photovoltaic effect to produce voltage from incident radiation. The amount of contrast in an image is dependent on the bits of information for the analog-to-digital conversion, for example a one bit system will have contrast of 0 or 1; a two bit system will have contrast values of

0, 1, 2, or 3. Typical systems will be eight bit (contrast of zero – 255) or 16-bit (contrast of zero – 65535) providing sufficient levels of contrast to identify areas of high or low intensity and therefore high or low concentrations of chemicals. The electrons (and subsequently voltage) produced by the incoming radiation is proportional. Therefore, chemical images that are obtained will have areas of higher intensity (more chemical information) and areas of lower or no intensity (less or no chemical information) and is proportional to the concentration of the analyte under investigation at that point. However, the manner in which the concentration and intensity are proportional is dependent on the spectroscopic technique chosen.

Optical chemical images provide the visualization (i.e. spatial orientation) afforded through microscopy with the chemical specificity inherent in molecular transitions. Visualizing the spatial orientation aids in understanding the composition (i.e. quantification or classification) of the samples under investigation and range from quality assurance in the pharmaceutical industry<sup>3</sup> to terrestrial monitoring of biomass via satellite.<sup>4</sup> Chemical imaging can also provide real time (kinetic) interactions and is often used in the biomedical disciplines for cellular imaging.<sup>5</sup> However, some limitations to what information (temporal or spatial) can be obtained are due to the technique chosen and the method of light collection.



**Figure 1.1:** A portion of the electromagnetic spectrum with the representative wavelengths and type of radiation in their relevant regions.

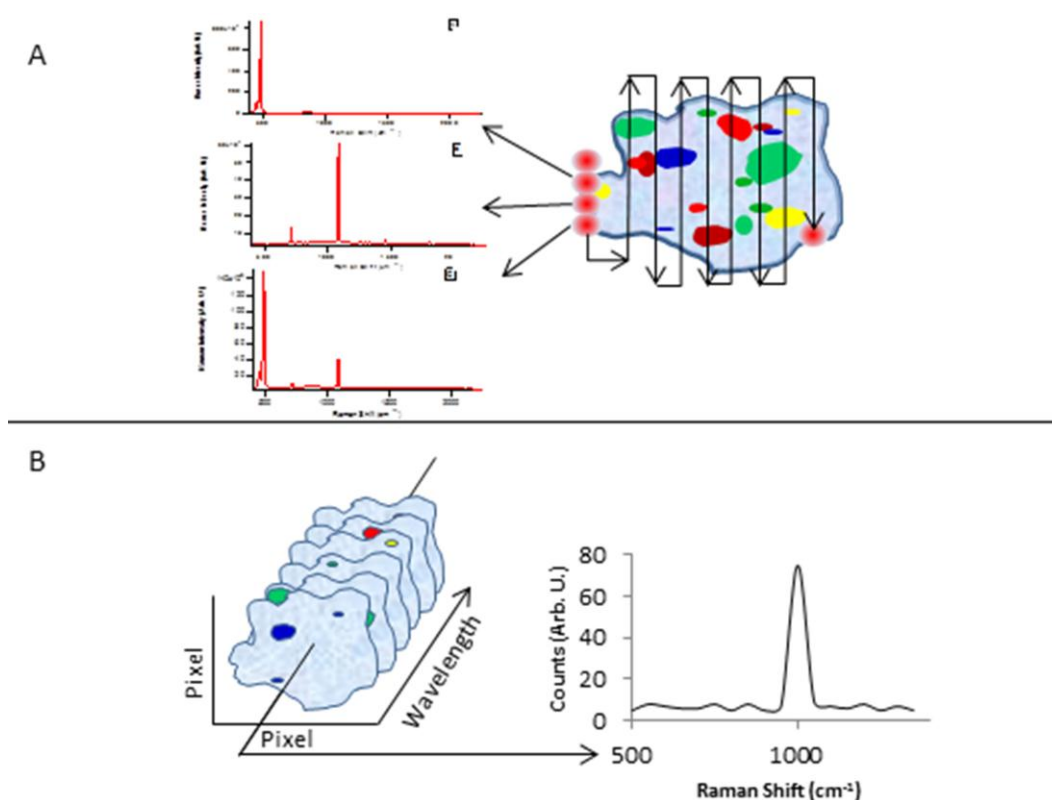
The focus of this introductory chapter is limited to the use of optical spectroscopies used to obtain images employing the use of ultra-violet (UV) through the near infrared (NIR) portions of the electromagnetic spectrum. Figure 1.1 provides a cartoon representation of a portion of the electromagnetic spectrum and highlights different regions with their wavelengths. The main spectroscopies that employ these wavelengths are fluorescence, absorption, Raman, and IR. Fluorescence and absorption spectroscopies obtain information about the electronic transitions within a molecule while Raman and IR obtain information regarding the vibrational transitions within a sample. The latter tends to provide more detailed “fingerprint” information while the former has more broadened luminescence and often lacks chemical specificity. Details of these spectroscopies will be expounded upon further in Section 1.3.

Two primary techniques can be employed to obtain chemical specific images. These are 1) raster scanning across a sample (Figure 1.2A), or 2) obtaining multiple images at

different frequencies to obtain spectral information (Figure 1.2B). In both cases, spectral information is obtained for an area of a sample and can produce chemical specific images.

### 1.2.1 Raster Scanning

One way of obtaining a chemical image is by using a focused light source (e.g. a laser) and raster scanning it across the image obtaining a spectrum at each point (see Figure 1.2A). After a spectrum is obtained at the first point, the focused beam is moved (just



**Figure 1.2:** The two ways of obtaining images. (A) Raster scanning a focused beam and obtaining a spectrum at each point across the sample provides a full spectral image. (B) Hyperspectral imaging (or multispectral imaging) provides a wide-field image at specific frequencies where a 3-D hypercube of information can be obtained resulting in x- and y- pixel information and frequency information in the z-dimension.

passed where it was previously) and a new spectrum is obtained. This is repeated across the entire sample for a complete chemical image. Advantageously, no prior knowledge of the sample is required and a spectrum is recorded for each focal spot across the sample. This provides a complete spectrum at each point of the raster and can be used to create a chemical image at any frequency that was spectrally obtained. However, two disadvantages that prevail are longer acquisition times and resolution.

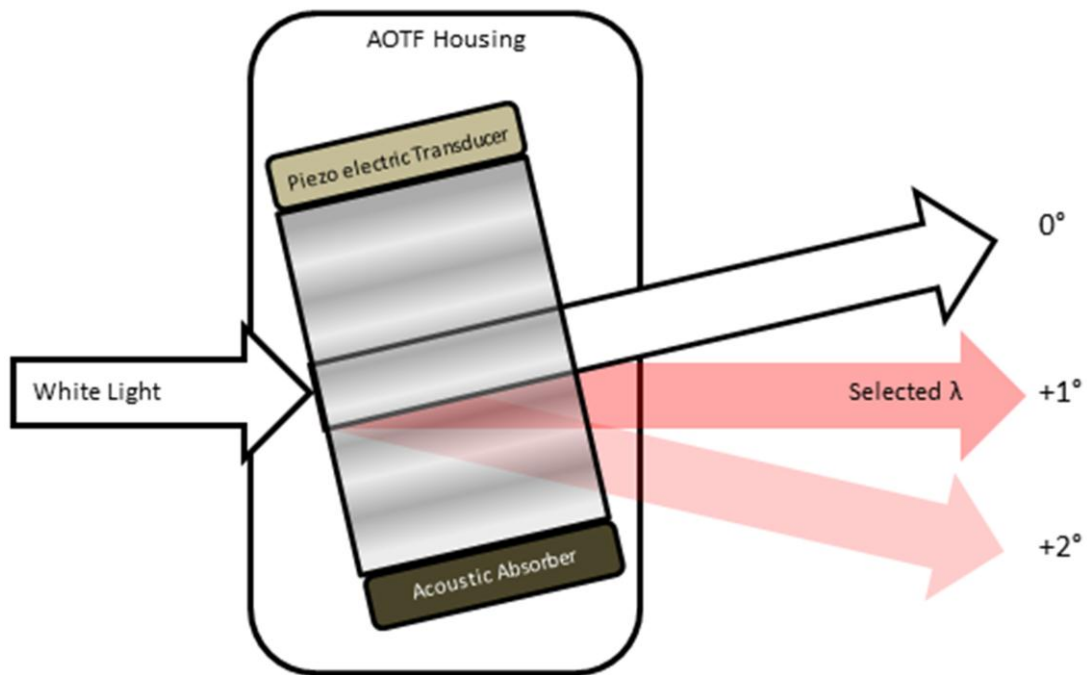
The total acquisition time for a particular sample is surface area dependent. Larger surface areas to be imaged require more total time to image considering a focused beam (< 1 mm in diameter) is used to scan across the surface. While each spectrum (i.e. each point of the raster) can be obtained quickly (ideally the millisecond time scale) hundreds to thousands of points may need to be acquired. Automated systems reduce the amount of time between points and reduce human error, though can be costly.

### *1.2.2 Hyper- and multispectral imaging*

A second way of obtaining an image is through hyper- (many) or multi- (several) spectral imaging. Instead of utilizing a diffraction-limited spot and raster scanning it across the sample, an entire image is obtained in one acquisition at a particular wavelength of light. See Figure 1.2B for a cartoon representation. To obtain hyperspectral images, an entire image is obtained at each wavelength of light spectrally shifting the frequency using a light modulating device. To this end, there are two primary types of light-modulating devices: an acousto-optic tunable filter (AOTF) or a liquid crystal tunable filter (LCTF).

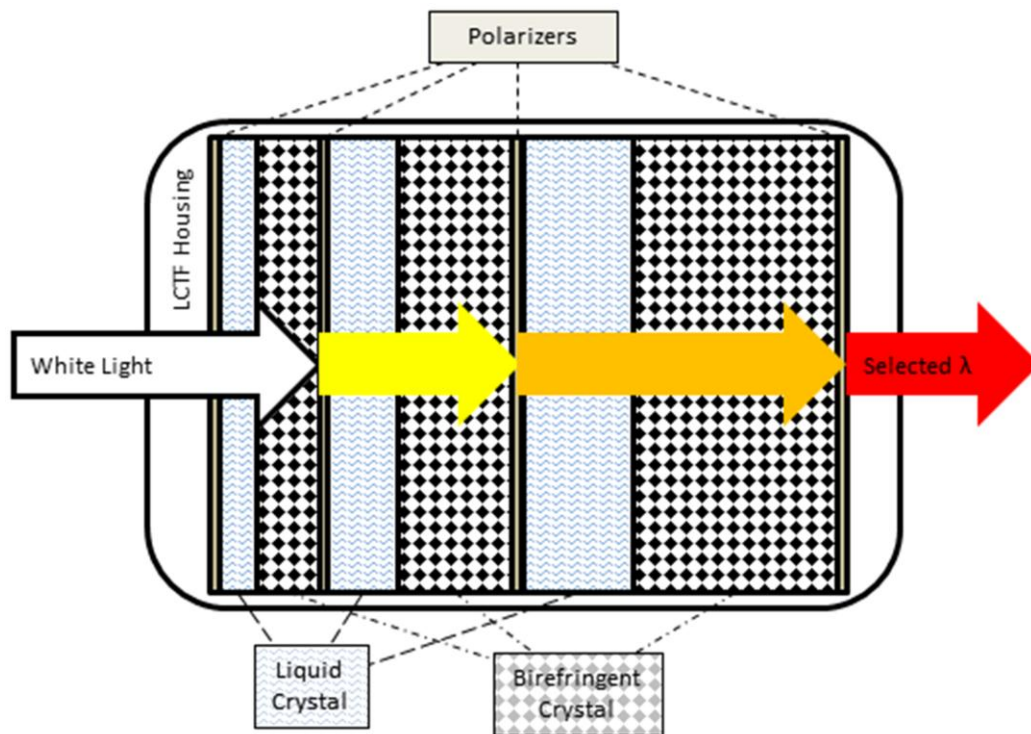
An AOTF is based on an interaction between acoustic waves and light propagating through a crystal (typically  $\text{TeO}_2$  when in the visible region of the electromagnetic

spectrum); as seen in Figure 1.3. A piezo electric transducer and an absorber are cemented to either side of the crystal. The transducer transmits radio frequencies (RF) through the crystal inducing periodic areas of high and low density. Because this acts through the thickness of the crystal, a small bandwidth of light is diffracted (much like a grating) providing transmission of a specific narrow band pass of light while retaining an image. An AOTF allows for rapid selection of frequency about microseconds and has no parts that physically move.



**Figure 1.3:** A cartoon representation of an acousto-optic tunable filter (AOTF). White light (or a large bandpass of light) enters the AOTF and due to periodic areas of high and low density produced by a radio frequency driver, a crystal (typically  $\text{TeO}_2$  in the visible region of the spectrum) diffracts selected frequencies of light.

Alternatively, a LCTF is based on light interactions between a series polarizers and liquid crystals. A retardation effect that arises as light travels through a liquid crystal medium of a certain polarization coupled with the birefringent crystals and polarizers in series allow for the selection of a specific wavelength of light. This is shown in Figure 1.4. Bandwidths of LCTFs are typically larger than that of AOTFs, approximately several nanometers (as opposed to a fraction of a nanometer in AOTFs), and the rise time is slower on the millisecond time scale. One main advantage of multispectral imaging is a reduction in the imaging time by imaging at only one or several select wavelengths at frequencies of interest. When obtaining hyperspectral images, the entire spectrum is scanned and *a priori* knowledge of the frequencies of interest is not necessary and still



**Figure 14:** A cartoon representation of a liquid crystal tunable filter (LCTF). White light (or a large bandpass of light) enters the LCTF and through a series of stacked polarizers, liquid crystals and birefringent crystals, a small bandpass ( $\sim 1\text{-}2\text{nm}$ ) of light is selected.

takes less time than raster scanning. Additionally, if the researcher is interested in only observing one frequency to show whether or not a chemical is present only one image would be required, significantly reducing imaging time.

An image that has passed through a light modulating device (i.e. AOTF or LCTF) would now consist of the chemical information at one (or several) wavelengths of light and can be imaged on a camera. This analog-to-digital conversion occurs in a series of picture elements, called pixels, patterned in an array. Typical arrays for scientific research are 512x512, 1024x1024, 1024x256, etc. and are usually application dependent

### *1.2.3 Spatial Resolution*

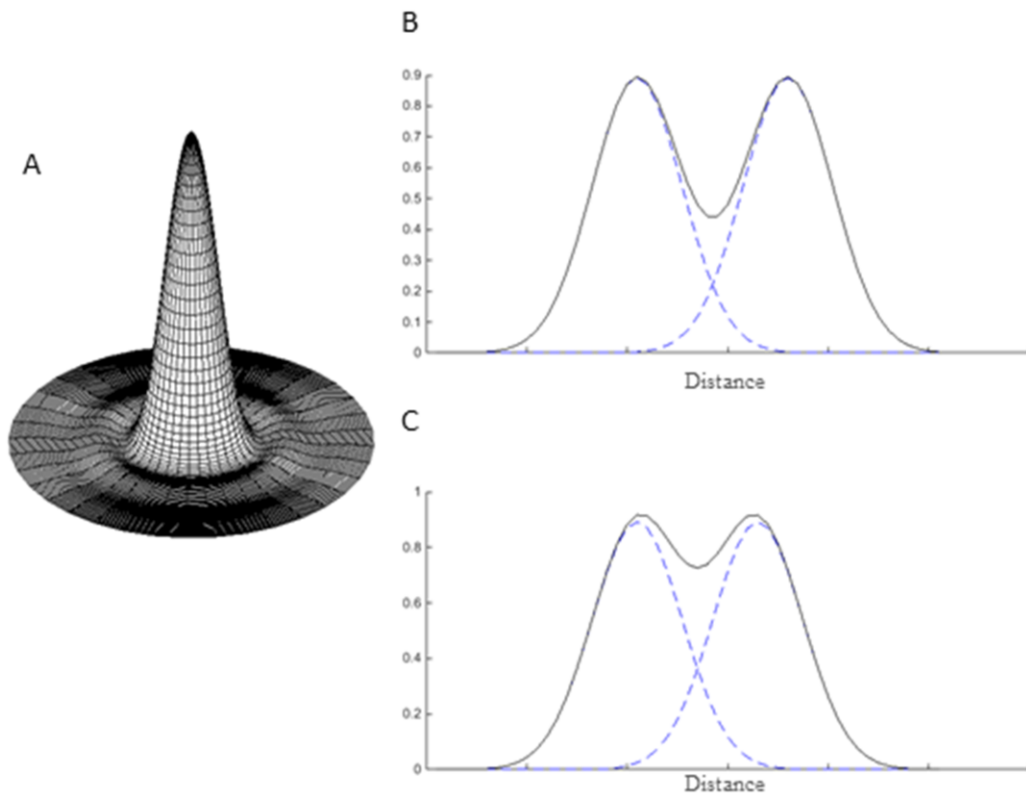
The resolution of images are primarily defined by two parameters, 1) the diffraction-limit of light and 2) the optics used for delivering light to and collecting light from the sample. The diffraction-limit of light is due to interference of the light waves at a focal point. This produces a central spot (zeroth order diffraction) surrounded by one or more rings (first order diffraction, second order diffraction, etc.), as seen in Figure 1.5A. The central spot surrounded by concentric rings is an airy disk pattern. The central spot, as described below in Eq 1.1., is partially dependent on the wavelength of the light employed. The diffraction-limited theory was first described by Ernst Abbe in 1873<sup>3</sup> with lateral resolution defined as:

$$Abbe\ resolution = \frac{\lambda}{2NA} \quad \text{Eq. 1.1}$$

Where  $\lambda$  is the wavelength of light being used to interrogate the sample and  $NA$  is the numerical aperture of the objective (or lens) being used to focus the light. For example, if a microscope objective being used had an  $NA$  of 0.75 and a HeNe laser was being used at



a wavelength of 632.8nm, this would result in a diffraction-limited resolution of approximately 422nm. This definition (Eq. 1.1) provides sufficient contrast (50%) between the centers of two points to consider them separate (see Figure 1.5B) and is often approximated to one-half the wavelength of light used to interrogate the system. In the following years, Lord Rayleigh later refined the criterion of the lateral resolution to the amount needed to contrast two objects at 20% between them (see Figure 1.5C) and is defined as:



**Figure 1.5:** (A) A theoretical airy disk pattern created by a perfectly focused laser beam in which the central location is of highest intensity of the 0 order diffraction while the less intense rings of higher order diffraction. (B) A representation of Abbe resolution resulting in approximately 50% contrast between two points. (C) A representation of Rayleigh resolution resulting in approximately 20% contrast between two points.

$$\text{Rayleigh resolution} = \frac{0.61\lambda}{NA} \quad \text{Eq. 1.2}$$

These definitions (Eq. 1.1 and Eq. 1.2) are the generally accepted definitions of resolution, though several others exist based on different amounts of contrast and therefore different statistical parameters. From equations 1.1 and 1.2, it can be seen that the lateral resolution is partially dependent on both wavelength of light used to interrogate the system and the optics which are used for focusing. When building an optical system, using better optics (and/or optics with a larger NA) aids in the reduction of the diffraction-limited spot (point spread function; PSF), and ultimately increase the resolution of the image being obtained. However, this is practically limited to NA's with a maximum value between 1 – 1.5 when using conventional optics; though, many have NAs between 0.25 and 0.65.

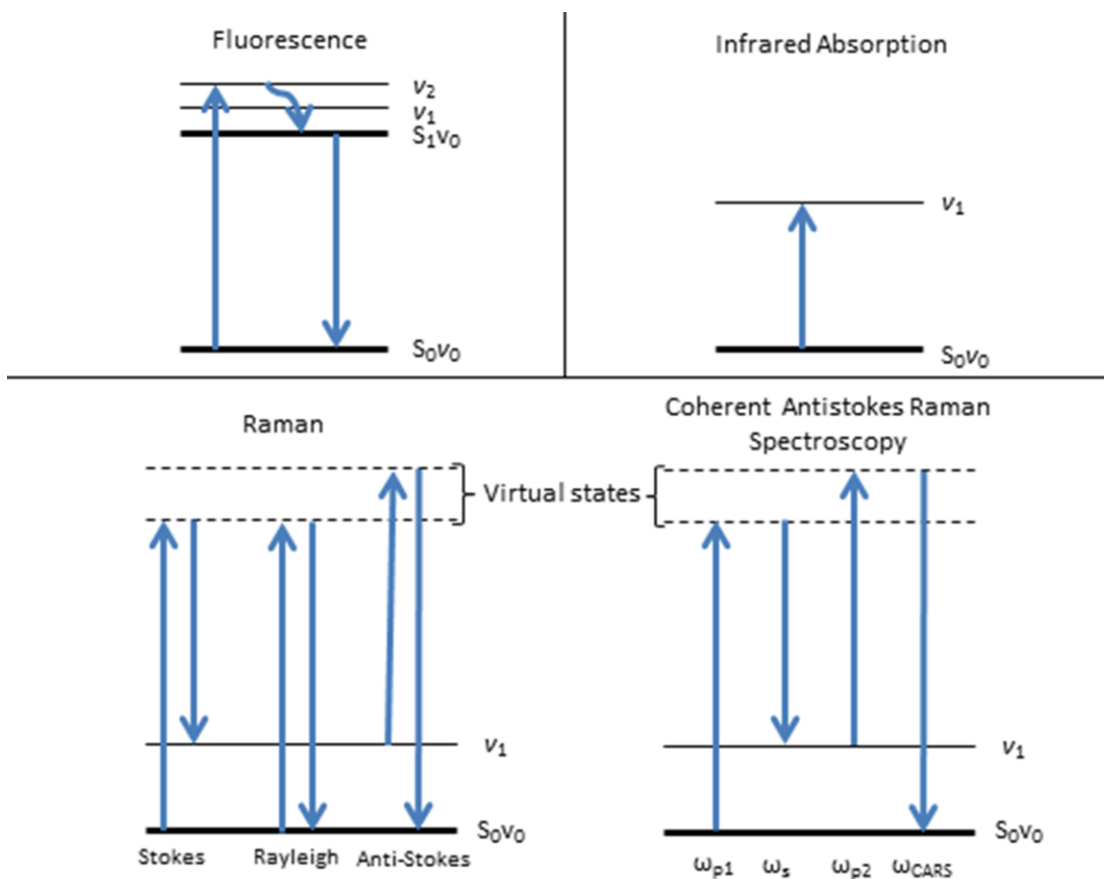
The spatial resolution of an image is also partially dependent on imaging equipment employed (i.e. camera, pixel array, etc.). The equipment used will define the size and density of the pixels in the image. As the size of each pixel decreases (and therefore an increase in pixel density on a chip of the same size) the spatial resolution will also increase (i.e. higher resolving power) when using identical optics. Increasing pixel density allows for smaller differences in objects to be differentiated when the signal is converted from analog-to-digital because the individual picture elements are physically smaller. However, current technology is limited to micron-sized pixels and, even as technology progresses towards smaller pixels, the light from an image cannot be focused tighter than the diffraction-limit using conventional techniques described previously.

### *1.2.3 Electronic-transition based imaging*

Light-matter interactions for imaging exist from X-ray (angstrom wavelength) to thermal (micron wavelength). UV – NIR ( $\sim 400\text{nm}$  – several thousand nanometers) light interacts with the electronic and vibrational transitions of the molecule providing molecular interactions. Ideally, these interactions will provide a “fingerprint” of the molecule in the form of a molecular spectrum unique to the molecule (or group of molecules) under investigation. Typically, though, electronic spectra are broadened due to interactions with and population of higher-order vibrational and rotational states within the excited electronic state. Electronic-transition based imaging is usually done via absorption or fluorescence. These phenomena will be briefly introduced in the following sections.

#### *1.2.3.1 Fluorescence*

Fluorescence is due to the absorption of a photon of light corresponding to a specific electronic transition (typically as an indirect measure of the presence of an analyte in imaging applications) followed by an emission of a photon of the same spin state (singlet-singlet transition). This most often occurs in the UV – visible range in the electromagnetic spectrum and is quite often associated with biological imaging. Figure 1.6 represents a partial Jablonski diagram highlighting this and other types of transitions. In Figure 1.6,  $S_0$  and  $\nu_0$  are the ground state electronic and ground vibrational states, respectively.  $S_1$ ,  $\nu_1$ ,  $\nu_2$ , and  $\nu_3$  are excited electronic and vibrational states. Vertical lines represent photonic transitions, while curved lines represent non-radiative transitions. The vertical axis represents energy, while the horizontal axis is the reaction coordinate. The photonic transitions (i.e. absorption and emission) typically occur prior to any nuclear rearrangement and therefore represented as vertical lines. The emitted photon has less



**Figure 1.6:** Partial Jablonski diagrams of fluorescence, infrared absorption, Raman scatter and coherent anti-Stokes Raman scatter. In these diagrams,  $S_i$  and  $v_i$  represent electronic and vibrational states, respectively. Vertical arrows represent photonic interaction with the material while curved arrows represent non-radiative energy transfers. See text for further discussion.

energy than the incoming photon due to non-radiative relaxation and as a result is spectrally red-shifted, and will occur within nanoseconds after excitation. Broadband emission spectra are characteristic of fluorescent probes and are often 10's of nanometers broad. Fluorescent molecules often have high quantum yields making fluorescence measurements very sensitive. The characteristics (quantum yield, broadness, etc.) are dependent on the solvent system that is employed as well. Often, fluorescence images are acquired using cellular components and therefore typically in an aqueous environment.

The use of fluorescence has delivered a wide range of fluorophores and many application-specific fluorophores are available.<sup>6, 7</sup>

Fluorescent molecules or proteins are often used as an indirect measure of the subject under investigation. Therefore, the activity, presence, or concentration of the analyte is often implied by the fluorescence observed. Measurements can usually be multiplexed (two or more fluorescent probes simultaneous used in a sample) with an upper limit of four fluorophores due to their broadband emission which limits the number of functions or analytes that can be observed in any one measurement. Despite these, fluorescence is widely used in biological imaging.

Natural (e.g. proteins, single conjugated molecules, etc.)<sup>8, 9</sup> and synthetic (e.g. metallic and polymeric quantum dots)<sup>10, 11</sup> fluorescent probes have been used recently for fluorescence imaging. Development and improvement of colored fluorescent proteins have aided in the differentiation and targeting of cellular constructs.<sup>8</sup> Furthermore, kinetic information can be gleaned from fluorescence imaging such as in one example where photocatalysis was measured across a photocatalytic site, showing improved catalytic activity on one of the crystal facets.<sup>9</sup> Polymer dots and quantum dots have also been used in biological imaging for the exploitation of their higher quantum yields and lower photobleaching characteristics.<sup>10, 11</sup> Both natural and synthetic fluorescent probes can be used for targeting specific biological functions and used in imaging to provide location, concentration, or activity.<sup>12</sup>

### 1.2.3.2 Absorption-based imaging

Absorption-based imaging occurs with an electronic transition corresponding to the frequency of light impinging on the material under investigation. The excited state of the molecule will then relax to its ground state through non-radiative relaxation. This type of imaging is realized through the *loss* of photons instead of photon emission at a different wavelength. Light will also reflect off the material. In this case, the reflectance image will consist of the light *not* absorbed by the material. If the sample is transparent, then a transmission image can also be obtained consisting of all the frequencies that are not absorbed and not scattered by the material. These techniques are sensitive as well, owing the sensitivity to the larger cross sections (i.e. extinction coefficients) of the molecules resulting in an increased probability of the light interacting with the molecule. Absorption-based imaging is widely used in physics and in biomedical applications.<sup>13-15</sup> In biomedical applications, absorption-based imaging has been used for identification of cancers, retinal disease and use within biliary surgeries.<sup>16</sup> In physics, absorption of ultra-cold gases can provide images of ground state molecules as a different approach to investigating these model quantum systems.<sup>13</sup>

Large cross sections and high quantum yields will often make both absorption and fluorescent techniques quite sensitive. However, while an electronic absorption may be unique to a particular molecule under investigation, the broadband nature of absorption and fluorescence spectra often do not provide the molecular specificity required for molecular identification, especially in complex environments with multiple absorbers and emitters. It is therefore often useful to proceed with a technique (i.e. vibrational-based

imaging) that does provide the chemical specificity required for molecular identification when needed.

### **1.3 Vibrational-transition based imaging**

This section discusses the vibrational interactions that light can have with matter. Both Raman scatter and infrared absorption interact with stable vibrational levels of a molecule through two different mechanisms and can probe different information about vibrations. The two techniques are therefore inherently complementary. This section introduces the reader to these techniques and discusses the differences between the two.

#### *1.3.1 Infrared Absorption*

Infrared (IR) absorption occurs with the absorption of a photon of light corresponding to the energy of a vibrational transition within a molecule. This results in large cross-sections and provides sensitivity within the fingerprint region of the electromagnetic spectrum. IR absorption corresponds to wavelengths of approximately 0.750 - 1000 $\mu\text{m}$ . This results in lower-resolution images due to the wavelength dependence of the diffraction-limit of light. See Figure 1.1 for a visual relationship between the regions of the electromagnetic spectrum.

IR absorption is sensitive due to it being an absorptive phenomenon. IR absorption relies on a change in the dipole moment of the molecule during a vibration and that the absorption takes place between two adjacent vibrational energy levels (i.e.  $\nu = 0$  to  $\nu = 1$  or  $\nu = 1$  to  $\nu = 2$  where  $\nu$  is the vibrational energy level). As such, this provides a chemical vibrational fingerprint of the molecule and allows for the detection of several (or more) analytes in a single sample. Biological and inorganic species are easily

measured with IR.<sup>17-19</sup> While IR imaging has been historically difficult to use in aqueous media due to broad-band water absorption ( $\nu(\text{O-H})$ ), the use of attenuated total reflection (ATR) IR has made this possible through interrogation of a short path length whereby the analyte should be in- or close-contact with the surface of the substrate.<sup>19, 20</sup> IR imaging has applications within forensics in the identification of biological fluids,<sup>21</sup> and in the pharmaceutical industry<sup>22</sup> providing that different analytes and potential containments can be differentiated with this technique. Due to the diffraction-limit of light, however, the image quality will always have a lower resolution than similar measurements analyzed with fluorescence and absorption (in the visible portion of the electromagnetic spectrum). Therefore, implementation of a wavelength-independent phenomenon providing fingerprint vibration information is necessary for higher-resolution, far-field images.

### *1.3.2 Raman*

Raman scattering is an inelastic scattering of light due to interactions with a molecule or particle significantly smaller than the wavelength of light used to interrogate a sample providing vibrational information as a fingerprint of the analyte. This phenomenon is wavelength independent and can be used in the UV through NIR portions of the spectrum, and ideal for imaging considering the resolution of an image is partially dependent on the wavelength of light used to interrogate the system. Raman scattering can occur so long as the energy of the light interrogating a particular vibration is greater than the energy of the vibration itself and is therefore not absorbed. For Raman signals to be adequately obtained, lasers must be employed for their narrow bandwidth of emitted light; any vibrations that are *less* energetic than the frequency of the laser employed *can*



have a Raman signal. Therefore, with Raman imaging, the wavelength can be tuned away from absorption bands of potential interferents and, in biomedical imaging, out into the “biological window” ( $> 700\text{nm}$ ) which is where many common biological substances no longer absorb.

Raman scattering requires a change in the polarizability of a molecule as the light passes through a vibration. Just as in IR, the change in the vibrational level is  $\nu = \pm 1$ ; in other words, the scattering phenomenon will be from  $\nu = 0$  to *past*  $\nu = 1$ , into a virtual level, prior to “relaxing” back down to  $\nu = 1$ . The energy transferred to the molecule from the photon results in a lower energy “emission” of the photon called Stokes shift, while energy transferred to the photon from the molecule results in higher energy “emission” of the photon called an Anti-Stokes shift. See the partial Jablonski diagram in Figure 1.6 for further detail. As described earlier, straight vertical arrows are indicative of an energy transition due to a photon interacting with the material. Horizontal lines represent electronic ( $S_i$ ) and vibrational ( $\nu_i$ ) levels. A dashed horizontal line represents a virtual state that is a fleeting, non-stable energy state induced by a photonic interaction. When compared to IR, however, Raman is inherently weak with cross sections on the order of  $10^{-17}\text{cm}^2$  and  $10^{-29}\text{cm}^2$  for IR and Raman respectively. While employing lasers have the advantage of more photons per unit area (and therefore higher Raman signals), powerful lasers can also damage the sample under investigation.

Raman imaging has applications within the food industry,<sup>23, 24</sup> pharmaceuticals,<sup>25</sup> biology,<sup>26, 27</sup> explosives detection,<sup>28, 29</sup> and forensics<sup>29, 30</sup> highlighting the diversity in which Raman chemical imaging can be employed. Understanding the spatial location of analytes can be imperative, especially when considering something like quality control

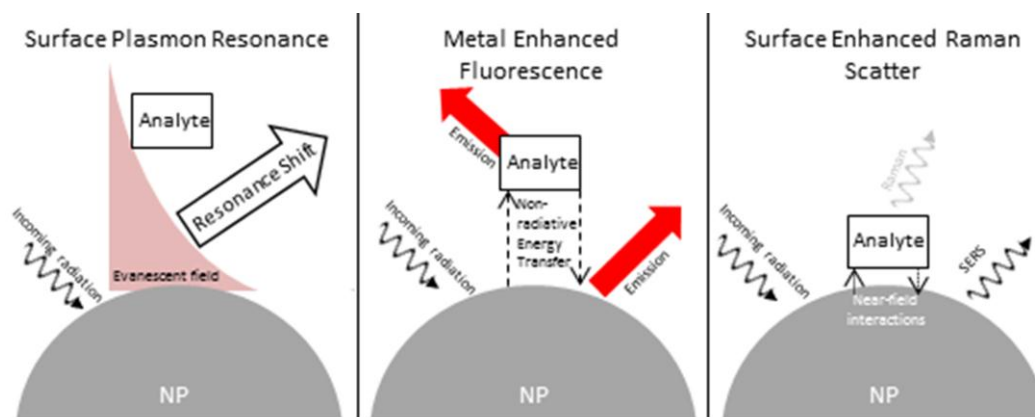
within the food industry or within pharmaceuticals. Furthermore, quantification of an analyte within a spatial location provide insight into biological processes without absorption from the aqueous medium.<sup>31</sup>

IR and Raman are advantageous to use for imaging due to the chemical specific fingerprints that they provide and considering that they are mechanistically different; both techniques are complementary to each other. One key advantage of Raman and IR over other optical spectroscopies is that the signals obtained are inherent to the analyte or molecule under investigation owing this to the vibration of the molecule. Lasers that are higher in wavelength and therefore less likely to damage the sample can be employed for Raman measurements. A key advantage of Raman over IR is that there is no broadband scatter due to water, and biological species and/or analyte in aqueous media may be investigated with ease. Since Raman is inherently weak, there is a need to further increase the sensitivity of Raman despite the use of lasers. This can be achieved, as described in the following section, by surface enhancement techniques.

#### **1.4 Surface Enhanced Techniques**

Combining sensitivity and selectivity, especially when striving to understand the spatial location of analytes, is of key importance. Sensitivity is necessary for the potentially small amount of material within each imaging area and selectivity is important to differentiate one material from another within an image. One such way of combining these two parameters is through plasmonic enhancement. Plasmonic enhancement is due to a collective oscillation of the conductive band electrons of a metal-coated substrate that is in resonance with the frequency of light being used.<sup>32</sup> This collective oscillation effectively increases the cross section of a molecule that is in close proximity to the

surface of the substrate. Surface plasmons propagate across a metallic interface while localized surface plasmons are within metallic nanostructures.<sup>32, 33</sup> The plasmons are dependent on the metal type. Group 13 and group 14 metals can be used for plasmons, though coinage (i.e. Au, Ag, Cu, Al) are most often used.<sup>32, 34, 35</sup> The size (i.e. 50 – 100's nm) and shape (i.e. hole, spike, rod, pyramid) of the underlying nanostructure will also define the plasmons which can be varied to match the application desired and is dependent on the light being used.<sup>36-40</sup> Arrays of nanostructures on a substrate can be used for imaging as well; this provides areas of locally strong enhancement resulting in chemical information at each point of the nanostructured surface.<sup>41-48</sup> Figure 1.7 shows a cartoon representation of surface enhancement when a nanoparticle is employed for the



**Figure 1.7:** Cartoon representation of surface plasmon resonance (SPR), metal enhanced fluorescence (MEF) and surface enhanced Raman scatter (SERS). In SPR, an analyte residing within an evanescent field causes a spectral shift in the resonance absorption profile. MEF is caused by a non-radiative energy transfer between the nanoparticle (NP) and the analyte (and vice versa) resulting in the co-emission of fluorescence from the analyte and the NP and must be between 5-15nm from the surface of the NP. In SERS, the analyte must be within near contact (< 5nm) of the NP surface for the near-field interactions of the plasmon coupling and increased scatter from primarily the NP.

techniques discussed below.

Two common techniques that utilize plasmonic enhancement are surface plasmon resonance (SPR) and metal enhanced fluorescence (MEF), represented pictorially in Figure 1.7. SPR probes the local environment ( $<100\text{nm}$  from the surface) by an evanescent field of a surface plasmon propagating across a metallic surface (depicted as the red field extending from the nanoparticle's surface).<sup>49-52</sup> Changes in the dielectric constant on or near the surface cause a spectral shift in the resonance absorption that is measured.<sup>49, 50, 52</sup> Imaging arrays have been developed for SPR and primarily used for biosensing whereby binding of an analyte or a protein causes the spectral shift observed.<sup>53-56</sup>

MEF, however, is due to a different mechanism. Increased emission of the fluorescence is due to a dipole interaction of the fluorophore and plasmonic structure providing a rapid, non-radiative transfer between the two followed by the radiative emission of both the metal and the fluorophore.<sup>57-62</sup> Unlike SPR, the fluorophore must be within an optimal distance of 10-20nm of the nanoparticle's surface for an increase in emission requiring precise control of fluorophore distance from the metallic nanostructures and is due to metallic materials quenching fluorescence in close proximity.<sup>49, 59, 61, 63, 64</sup> MEF imaging has primarily been used for bioimaging and biomarkers where core-shell and other distance-precise materials for binding and signaling have been employed.<sup>47, 65-69</sup>

#### *1.4.1 Surface Enhanced Raman Scatter*

Surface enhanced Raman scatter (SERS) is the primary focus of the surface enhanced modalities as this is used in this document. SERS is dependent on two mechanisms, an

electromagnetic enhancement, and a chemical enhancement, that work in concert to provide the full enhancing effect.<sup>70-73</sup> As with other plasmonic techniques, these too require a nanostructured metallic surface but must be within 5 nm or closer to the surface for enhancement to occur. See Figure 1.7 for a generalized scheme of how SERS works.

Understanding the general mechanisms by which an enhancement strategy works aids in understanding the output from the transducer. Plasmonic enhancement for Raman scattering is only at near contact (<5nm) and therefore helps define the depth of view when imaging. The enhancement is provided by two mechanisms simultaneously: the electromagnetic mechanism, providing the majority of the enhancement at a  $10^6 - 10^{11}$  fold increase in signal<sup>74</sup> or by the chemical mechanism, providing  $10^2 - 10^3$  fold increase in signal.<sup>49, 74, 75</sup> The distance dependence of SERS is due to the electromagnetic enhancement whereby the analyte experiences the oscillating electric field that exists within the plasmon on the surface and results in higher intensity of the electric field.<sup>32, 49, 76</sup> In addition, scattered radiation can also couple with the plasmonic surface further increasing the electromagnetic enhancement.<sup>49, 77</sup> SERS imaging is often used in biomedical (i.e. drug delivery and detection or biological imaging) and in high-resolution imaging and surface characterizations.<sup>5, 43, 78-82</sup>

As sensitivity has increased, so has the drive towards imaging smaller concentrations of analyte, towards the ultimate goal of single molecule. As such, increased sensitivity has made the nanoscale world available. Various techniques have been developed to achieve visualization below the diffraction-limit of light and is generally called super resolution chemical imaging (SRCI) and is discussed in the following section.

## 1.5 Super resolution chemical imaging

Super resolution chemical imaging is defined by an image providing chemical information that is below the diffraction-limit of light for that particular system. The diffraction-limit can be approximated as one-half the wavelength of light that is employed, and comes out of Eq 1.1. SRCI techniques were born from the development of a near-field scanning optical microscopy (NSOM) technique in the 1980s that allowed a sub-wavelength aperture to transmit light.<sup>83, 84</sup> Advances in SRCI were primarily achieved through the inherent sensitivity provided from the high quantum yield of select fluorophores and through optical modulation and increased computing power. However, vibrational techniques have shown to be approximately as sensitive as fluorescence in many cases when enhancement is utilized in the imaging.

### *1.5.1 Fluorescence -based Super Resolution Chemical Imaging*

In general, there are three ways of achieving super resolution images. The first is using a sub-wavelength aperture or the apex of a small nano-triangle (or similar) on a cantilever to obtain the chemical signals from only the small aperture or tip. These techniques require raster scanning of the probe across the surface to create an image.<sup>85, 86</sup> Since the signal is only originating from this small area of the aperture or the cantilever tip and can be characterized, the resolution is defined by their size. NSOM and tip-enhanced techniques utilize these methods.

A second way of obtaining a super-resolved image is through photoswitching abilities. These techniques rely on the ability to temporally modulate a subset of the population of fluorophores either optically or temporally (i.e. with relaxation to its original state).<sup>87</sup> This requires a fluorophore to be in an “on” state *or* an “off” state and be able to switch

between the two. Techniques such as photo activated localization microscopy (PALM) and stochastic optical reconstruction microscopy (STORM) utilize this. These techniques excite a sparse subset of the population of fluorophores (i.e.  $< 1$  fluorophore per diffraction-limited spot). The centroid of each diffraction-limited spot (i.e. fluorophore emitting) is calculated. The fluorophore is then turned “off” typically with irradiation of a different frequency of light. This process then repeats. The centroids are calculated with more precision than the diffraction-limited spot due to the number of times the centroid is calculated and therefore results in super-resolved images when reconstructed into a single image. These techniques require up to thousands of images to successfully reconstruct an image and are computationally taxing.

Lastly, a third way of obtaining super-resolved images is through structured illumination.<sup>88, 89</sup> These techniques illuminate the sample in a structured or patterned way and move the pattern across the sample to illuminate it in entirety. One generalized technique is structured illumination microscopy (SIM). An example of this is parallel illumination in the form of a sine wave with high intensity light at each peak of the sine wave and no intensity at each trough. This pattern is scanned through the sample providing illumination to each area. After computerized analysis, the super resolved image is reconstructed. Some techniques such as stimulated emission by depletion (STED) microscopy actually utilize both structured illumination and photoswitching whereby the excited state is depleted, or “turned off”, through stimulated emission at a faster rate than the surrounding fluorescence naturally occurs.

Despite huge gains in chemical imaging through SR techniques, most of the techniques employ fluorescence as the spectroscopic interrogation method to provide the sensitivity,

thereby limiting their inherent molecular identification. These include a lack of molecular specificity within the spectrum and indirect measurements of location and/or activity. In fact, there are only 10's of fluorophores and 10's of proteins used for fluorescence SRCI, many of which have significant spectral overlap.<sup>31</sup> Furthermore, when two or more fluorophores are employed, controls need to be used to ensure that there is a significantly small amount of overlap between the fluorophores as to not obtain false positives when filtering. This section highlights only key points of these techniques. There are many more hyphenated techniques and small variations of the ones listed above. The reader is directed towards several of the many reviews and information available at the following sources.<sup>29, 31, 87, 90, 91</sup>

### *1.5.2 Vibrational super-resolution chemical imaging*

In order to obtain fingerprint information from trace amounts of analyte to single molecules, SRCI using vibrational spectroscopy can be employed. There have been three main advances with SRCI in Raman imaging and are SERS, tip enhanced Raman spectroscopy (TERS), and structured illumination techniques. Mainly, employing plasmonic enhancement (SERS and TERS) has been at the forefront of vibrational SRCI. First, structured illumination will be discussed due to its similarities to the fluorescence-based techniques.

#### *1.5.1.1 Structured illumination for Raman based SRCI*

Structured illumination can be used in several ways for vibrational SRCI. In a non-enhancement strategy, non-linear spectroscopy can be used. In coherent anti-stokes Raman spectroscopy (CARS), three pump beams are used: one that pumps from the ground vibrational state to a virtual state, a second pump that stimulates the relaxation



from the virtual state to the first excited vibrational state, and a third laser that pumps from the first excited vibrational state to a second, higher energy virtual state. When this energy is in resonance, or matches a vibrational frequency of an anti-Stokes shift, the scatter is generated with a squared dependence on the number of molecules present, providing higher intensity than Raman alone. See Figure 1.6 for a partial Jablonski diagram and a recent review for further detail describing CARS in bioimaging.<sup>92</sup>

CARS has been shown theoretically<sup>9, 11, 93</sup> and experimentally<sup>9, 12, 94</sup> to surpass the diffraction-limit of light by using structured illumination. Theoretically, the resolution when imaging with CARS can be increased by modification of the point spread function (PSF) of the system. This is an analogous way of describing the pattern of illumination on the surface of the sample. Beeker *et al.* uses a fourth patterned “control” beam to populate the first excited vibrational state that suppresses the CARS output in such a way that is analogous to STED.<sup>11</sup> This technique uses a Gaussian beam ( $TEM_{00}$ ) to pump the sample while using a donut-shaped beam ( $TEM_{01}$ ) to deplete the first excited vibrational state, effectively squeezing the PSF of the Gaussian beam to a smaller point. This type of ground state depletion was shown practically using tris(bipyridine)ruthenium(II) ( $Ru(bpy)_3^{2+}$ ) with an envisioned increase in resolution to 175nm, though evidence was not provided showing this.<sup>12</sup> Alternatively, phase masks can be used with the existing three pump beams to further reduce the PSF and thus increase the resolution of the image in which one example provided 150nm spatial resolution imaging Si nanowires.<sup>9, 93-95</sup>

#### 1.5.1.2 Tip-enhanced methods

Plasmonic enhancement can also be used to provide super-resolved images. A localization of the electric field at the apex of a nanoscale, raster scanned tip provides

chemical images at the nanoscale.<sup>96</sup> In these methods, a cantilever with a metal-coated pyramid (or similar point-like nanostructure) on the end is brought into contact (i.e. < 5nm) with a material of interest. The metal-coated pyramid localizes the electric field to the apex of the tip creating an enhanced area approximately the size of the apex of the pyramid; typically ones to tens of nanometers in size. Tip enhanced techniques can utilize both the visible and the NIR region of the spectrum, providing further flexibility in the samples that can be used.<sup>15, 20, 22, 96-98</sup> One long-standing area of concern with tip-enhanced techniques, however, is the reproducibility of the tips used for imaging. While the apex of the tip is what defines the resolution, each tip will often have a specific enhancement and resolution associated with it and therefore there is tip-to-tip variability. This disadvantage is overcome by the use of mass fabrication of template-stripped pyramids with over 95% reproducibility in the template.<sup>45</sup>

#### *1.5.1.3 SERS*

Nanoparticles were first used as aggregates for SERS imaging. However, these often aggregated to form dimers or higher-order aggregates in a random fashion leading to hotspots (i.e. unintentional and random locations of uncharacteristically high intensity) and irreproducibility. While this is a disadvantage for imaging in a wide-field format, aggregation is advantageous for measuring single molecules residing within the hotspot. Considering the analyte can reside within a hotspot that is sub-diffraction-limited, and this location can be imaged with high accuracy, this has been exploited as a single-molecule super-resolution SERS (SM-SRSERS) imaging technique.<sup>99</sup>

SM-SRSERS utilizes similar observation and post-processing techniques as the STORM technique in fluorescence and is analogous. In short, many images are obtained and in

each image, the centroid of the signal originating from the single molecule in the junction of nanoparticles is calculated.<sup>17, 79, 100-103</sup> The centroid from the PSF of the image can be estimated, with many observations, with rather high accuracy from 1-10's of nanometers.<sup>17, 101</sup> Once the images are obtained and the centroid calculated, the images are reconstructed with high spatial resolution accuracy of <5nm.<sup>101</sup> It is also possible to distinguish luminescence from the nanoparticles with respect to the SERS junction by fitting both signals to centroids; they are often separate and distinguishable.<sup>100</sup> This advance allows for the deconvolution of the two signals and therefore higher precision.

Alternative to aggregated nanoparticles, patterned arrays can be used for SERS imaging. These techniques reconstruct images after many images of hotspots are obtained. In a similar capacity to SM-SRSERS, many images are obtained of the plasmonic substrate with an analyte present and then each single hotspot is fit with a two-dimensional Gaussian distribution to find the location. Using patterned arrays of nanoholes provides specific locations of the hotspots and thus higher electric field concentrating there while retaining a larger field of view. These can be modulated based on using a diffuser to scatter the incoming radiation and spatial resolution can be increased to within 10nm.<sup>18, 19</sup> Additionally, using a technique more closely related to TERS and NSOM, a fiber optic bundle can be modified providing a reproducible SERS platform available for surface studies.<sup>104-106</sup> In these studies, fiber-optic bundles are tapered, etched and metal-coated providing an array of thousands of high-intensity localized electric fields co-localized around the fiber optics. Each fiber optic acts as a point source the size of the tapered fiber optic and ranges from 100's of nanometers to microns. This technique has the advantages of SERS with focusing of the electric field, while retaining reproducibility across the

substrate as well as a periodic array of information similar to the patterned arrays with nanoholes. However, using arrayed platforms can yield cross-talk, a form of signal cross-over, typically dependent on how closely packed the array is.

Scanning techniques often take a long time to complete an entire image, reducing temporal capabilities and the wide-field imaging techniques tend to need hundreds to thousands of images to produce a super-resolved image. Therefore, there is a need for a wide-field, non-scanning imaging technique that does not require thousands of images for a high spatial resolution reconstructed image. As such, this thesis will address concerns associated with optical cross-talk on a densely packed nanoscale optical array for SERS imaging in a wide-field, non-scanning format, as well as post-processing techniques that can be employed providing higher resolution SERS images than what can be achieved with the fiber-bundle itself.

## **1.6 Conclusion**

While there are many different forms of imaging, and specifically chemical optical imaging, there are only select techniques that provide the researcher with a unique fingerprint of the sample under investigation. To this end, there is a need to provide high spatial resolution and reproducible fingerprint images. The technique utilizing fiber optic bundles for sub-diffraction-limited chemical imaging in a non-scanning, wide field format will be expanded upon and new methods for increasing the resolution beyond its inherent capabilities will be discussed in this document.

## **1.6 References**

1. Farkas DL. (2003) Invention and commercialization in optical bioimaging. *Nat Biotech* 21 (11): 1269-1271.
2. Council NR. (2006) *Visualizing Chemistry: The Progress and Promise of Advanced Chemical Imaging*. Washington, DC: The National Academies Press,
3. Abbe E. (1873) Beiträge zur Theorie des Mikroskops und der mikroskopischen Wahrnehmung. *Archiv für mikroskopische Anatomie* 9 (1): 413-418.
4. Phinn S, Roelfsema C, Dekker A, Brando V, Anstee J. (2008) Mapping seagrass species, cover and biomass in shallow waters: An assessment of satellite multi-spectral and airborne hyper-spectral imaging systems in Moreton Bay (Australia). *Remote Sensing of Environment* 112 (8): 3413-3425.
5. Stender AS, Marchuk K, Liu C, Sander S, Meyer MW, Smith EA, Neupane B, Wang G, Li J, Cheng J-X, Huang B, Fang N. (2013) Single Cell Optical Imaging and Spectroscopy. *Chemical Reviews* 113 (4): 2469-2527.
6. Lakowicz J. (1999) *Principles of Fluorescence Spectroscopy*. New York, Boston, Dordrecht, London, Moscow: Kluwer Academic/Plenum Publishers,
7. Lichtman JW, Conchello J-A. (2005) Fluorescence microscopy. *Nat Meth* 2 (12): 910-919.
8. Shaner NC, Campbell RE, Steinbach PA, Giepmans BNG, Palmer AE, Tsien RY. (2004) Improved monomeric red, orange and yellow fluorescent proteins derived from *Discosoma* sp. red fluorescent protein. *Nat Biotech* 22 (12): 1567-1572.

9. Tachikawa T, Yamashita S, Majima T. (2011) Evidence for Crystal-Face-Dependent TiO<sub>2</sub> Photocatalysis from Single-Molecule Imaging and Kinetic Analysis. *Journal of the American Chemical Society* 133 (18): 7197-7204.
10. Dubertret B, Skourides P, Norris DJ, Noireaux V, Brivanlou AH, Libchaber A. (2002) In Vivo Imaging of Quantum Dots Encapsulated in Phospholipid Micelles. *Science* 298 (5599): 1759-1762.
11. Wu C, Bull B, Szymanski C, Christensen K, McNeill J. (2008) Multicolor Conjugated Polymer Dots for Biological Fluorescence Imaging. *ACS Nano* 2 (11): 2415-2423.
12. Giepmans BNG, Adams SR, Ellisman MH, Tsien RY. (2006) The Fluorescent Toolbox for Assessing Protein Location and Function. *Science* 312 (5771): 217-224.
13. Wang D, Neyenhuis B, de Miranda MHG, Ni KK, Ospelkaus S, Jin DS, Ye J. (2010) Direct absorption imaging of ultracold polar molecules. *Physical Review A* 81 (6): 061404.
14. Lu G, Fei B. (2014) Medical hyperspectral imaging: a review. *BIOMEDO* 19 (1): 010901-010901.
15. Katzenmeyer AM, Holland G, Kjoller K, Centrone A. (2015) Absorption Spectroscopy and Imaging from the Visible through Mid-Infrared with 20 nm Resolution. *Analytical Chemistry* 87 (6): 3154-3159.

16. Lu G, Fei B. (2014) Medical hyperspectral imaging: a review. *J. Biomed. Opt.* 19 (1): 010901.
17. Corsi C. (2015) New frontiers for infrared. In *Opto-Electronics Review*, p. 3
18. Serrano AL, Ghosh A, Ostrander JS, Zanni MT. (2015) Wide-field FTIR microscopy using mid-IR pulse shaping. *Opt. Express* 23 (14): 17815-17827.
19. Kazarian SG, Chan KLA. (2013) ATR-FTIR spectroscopic imaging: recent advances and applications to biological systems. *Analyst* 138 (7): 1940-1951.
20. Palombo F, Danoux CB, Weinberg PD, Kazarian SG. (2009) Measurement of drug and macromolecule diffusion across atherosclerotic rabbit aorta ex vivo by attenuated total reflection-Fourier transform infrared imaging. *J. Biomed. Opt.* 14 (4): 044008.
21. Zapata F, Ortega-Ojeda FE, García-Ruiz C. (2017) Revealing the location of semen, vaginal fluid and urine in stained evidence through near infrared chemical imaging. *Talanta* 166 (Supplement C): 292-299.
22. Chan KLA, Hammond SV, Kazarian SG. (2003) Applications of Attenuated Total Reflection Infrared Spectroscopic Imaging to Pharmaceutical Formulations. *Analytical Chemistry* 75 (9): 2140-2146.
23. Qin J, Chao K, Kim MS, Cho B-K. (2016) Line-Scan Macro-scale Raman Chemical Imaging for Authentication of Powdered Foods and Ingredients. *Food and Bioprocess Technology* 9 (1): 113-123.

24. Qin J, Kim MS, Chao K, Schmidt WF, Cho B-K, Delwiche SR. (2017) Line-scan Raman imaging and spectroscopy platform for surface and subsurface evaluation of food safety and quality. *Journal of Food Engineering* 198 (Supplement C): 17-27.
25. Jérez Rozo JI, Zarow A, Zhou B, Pinal R, Iqbal Z, Romañach RJ. (2011) Complementary near-infrared and raman chemical imaging of pharmaceutical thin films. *Journal of Pharmaceutical Sciences* 100 (11): 4888-4895.
26. Tripathi A, Jabbour RE, Guicheteau JA, Christesen SD, Emge DK, Fountain AW, Bottiger JR, Emmons ED, Snyder AP. (2009) Bioaerosol Analysis with Raman Chemical Imaging Microspectroscopy. *Analytical Chemistry* 81 (16): 6981-6990.
27. Kalasinsky KS, Hadfield T, Shea AA, Kalasinsky VF, Nelson MP, Neiss J, Drauch AJ, Vanni GS, Treado PJ. (2007) Raman Chemical Imaging Spectroscopy Reagentless Detection and Identification of Pathogens: Signature Development and Evaluation. *Analytical Chemistry* 79 (7): 2658-2673.
28. Emmons ED, Tripathi A, Guicheteau JA, Christesen SD, A. W. Fountain I. (2009) Raman Chemical Imaging of Explosive-Contaminated Fingerprints. *Applied Spectroscopy* 63 (11): 1197-1203.
29. Tripathi A, Emmons ED, Guicheteau JA, Christesen SD, Wilcox PG, Emge DK, Fountain AW. (2010) Trace explosive detection in fingerprints with Raman chemical imaging. *Proc. SPIE Defense, Security, and Sensing*, 7665:76650N. SPIE



30. Wolfe J, Exline DL. (2003) Characterization of condom lubricant components using Raman spectroscopy and Raman chemical imaging. *J Forensic Sci* 48 (5): 1065-1074.
31. Lohumi S, Kim MS, Qin J, Cho B-K. (2017) Raman imaging from microscopy to macroscopy: Quality and safety control of biological materials. *TrAC Trends in Analytical Chemistry* 93 (Supplement C): 183-198.
32. Maier SA. (2007) *Plasmonics: Fundamentals and Applications*. Springer US,
33. Ru EL, Etchegoin P. (2008) *Principles of Surface-Enhanced Raman Spectroscopy: and related plasmonic effects*. Elsevier Science,
34. Knight MW, King NS, Liu L, Everitt HO, Nordlander P, Halas NJ. (2014) Aluminum for Plasmonics. *ACS Nano* 8 (1): 834-840.
35. McMahon JM, Schatz GC, Gray SK. (2013) Plasmonics in the ultraviolet with the poor metals Al, Ga, In, Sn, Tl, Pb, and Bi. *Physical Chemistry Chemical Physics* 15 (15): 5415-5423.
36. Orendorff CJ, Gearheart L, Jana NR, Murphy CJ. (2006) Aspect ratio dependence on surface enhanced Raman scattering using silver and gold nanorod substrates. *Phys. Chem. Chem. Phys.* 8 (1): 165-170.
37. Eustis S, El-Sayed MA. (2006) Determination of the aspect ratio statistical distribution of gold nanorods in solution from a theoretical fit of the observed

- inhomogeneously broadened longitudinal plasmon resonance absorption spectrum. *Journal of Applied Physics* 100 (4): 044324.
38. Wang J-F, Li H-J, Zhou Z-Y, Li X-Y, Liu J, Yang H-Y. (2010) Tunable surface-plasmon-resonance wavelength of silver island films. *Chin. Phys. B* 19 (11): 117310/117311-117310/117317.
39. Haynes CL, Van Duyne RP. (2001) Nanosphere Lithography: A Versatile Nanofabrication Tool for Studies of Size-Dependent Nanoparticle Optics. *The Journal of Physical Chemistry B* 105 (24): 5599-5611.
40. Boyack R, Le Ru EC. (2009) Investigation of particle shape and size effects in SERS using T-matrix calculations. *Phys. Chem. Chem. Phys.* 11 (34): 7398-7405.
41. Weisstein EW. Gaussian Function.  
<http://mathworld.wolfram.com/GaussianFunction.html>
42. Hess ST, Girirajan TPK, Mason MD. (2006) Ultra-High Resolution Imaging by Fluorescence Photoactivation Localization Microscopy. *Biophysical journal* 91 (11): 4258-4272.
43. Hankus ME, Li H, Gibson GJ, Cullum BM. (2006) Surface-Enhanced Raman Scattering-Based Nanoprobe for High-Resolution, Non-Scanning Chemical Imaging. *Analytical Chemistry* 78 (21): 7535-7546.
44. (2017) Correlative super-resolution fluorescence and electron microscopy using conventional fluorescent proteins in vacuo. *Journal of Structural Biology*.

45. Johnson TW, Lapin ZJ, Beams R, Lindquist NC, Rodrigo SG, Novotny L, Oh S-H. (2012) Highly Reproducible Near-Field Optical Imaging with Sub-20-nm Resolution Based on Template-Stripped Gold Pyramids. *ACS Nano* 6 (10): 9168-9174.
46. Sharma H, Wood JB, Lin S, Corn RM, Khine M. (2014) Shrink-Induced Silica Multiscale Structures for Enhanced Fluorescence from DNA Microarrays. *Langmuir* 30 (37): 10979-10983.
47. Szmazinski H, Toshchakov V, Piao W, Lakowicz J. (2013) Imaging of Protein Secretion from a Single Cell Using Plasmonic Substrates. *BioNanoSci.* 3 (1): 30-36.
48. Ray K, Lakowicz JR. (2013) Metal-Enhanced Fluorescence Lifetime Imaging and Spectroscopy on a Modified SERS Substrate. *The Journal of Physical Chemistry C* 117 (30): 15790-15797.
49. Strobbia P, Languirand E, Cullum BM. (2015) Recent advances in plasmonic nanostructures for sensing: a review. *OPTICE* 54 (10): 100902-100902.
50. Otto A. (1968) Excitation of nonradiative surface plasma waves in silver by the method of frustrated total reflection. *Z. Physik* 216 (4): 398-410.
51. Kretschmann E, Raether H. (1968) Notizen: Radiative Decay of Non Radiative Surface Plasmons Excited by Light. In *Zeitschrift für Naturforschung A*, p. 2135

52. Daghestani HN, Day BW. (2010) Theory and Applications of Surface Plasmon Resonance, Resonant Mirror, Resonant Waveguide Grating, and Dual Polarization Interferometry Biosensors. *Sensors* 10 (11): 9630.
53. Wong C, Olivo M. (2014) Surface Plasmon Resonance Imaging Sensors: A Review. *Plasmonics* 9 (4): 809-824.
54. Live LS, Bolduc OR, Masson J-F. (2010) Propagating Surface Plasmon Resonance on Microhole Arrays. *Analytical Chemistry* 82 (9): 3780-3787.
55. Romain FL, Gabriele SKS, Sebastian van de L, Clemens FK. (2016) From single-molecule spectroscopy to super-resolution imaging of the neuron: a review. *Methods and Applications in Fluorescence* 4 (2): 022004.
56. Toma M, Knoll W, Dostalek J. (2012) Bragg-Scattered Surface Plasmon Microscopy: Theoretical Study. *Plasmonics* 7 (2): 293-299.
57. Kuhn H. (1970) Classical Aspects of Energy Transfer in Molecular Systems. *The Journal of Chemical Physics* 53 (1): 101-108.
58. Geddes C, Lakowicz J. (2002) Editorial: Metal-Enhanced Fluorescence. *J Fluoresc* 12 (2): 121-129.
59. Lakowicz JR. (2001) Radiative Decay Engineering: Biophysical and Biomedical Applications. *Analytical Biochemistry* 298 (1): 1-24.

60. Lakowicz JR, Shen B, Gryczynski Z, D'Auria S, Gryczynski I. (2001) Intrinsic Fluorescence from DNA Can Be Enhanced by Metallic Particles. *Biochemical and Biophysical Research Communications* 286 (5): 875-879.
61. Aslan K, Geddes CD. (2010) Metal-Enhanced Fluorescence: Progress Towards a Unified Plasmon-Fluorophore Description. In *Metal-Enhanced Fluorescence*: John Wiley & Sons, Inc., 1-23 pp.
62. (2010) *Metal-Enhanced Fluorescence*. Hoboken, New Jersey: John Wiley & Sons,
63. Carminati R, Greffet JJ, Henkel C, Vigoureux JM. (2006) Radiative and non-radiative decay of a single molecule close to a metallic nanoparticle. *Optics Communications* 261 (2): 368-375.
64. Kümmerlen J, Leitner A, Brunner H, Aussenegg FR, Wokaun A. (1993) Enhanced dye fluorescence over silver island films: analysis of the distance dependence. *Molecular Physics* 80 (5): 1031-1046.
65. Centeno A, Xie F. (2014) Towards optimizing metal enhanced fluorescence (MEF) for improved detection of disease biomarkers. *Biointerface Research in Applied Chemistry* 4 (3): 731-735.
66. Cheng H, Wang C, Xu Z, Lin H, Zhang C. (2015) Gold nanoparticle-enhanced near infrared fluorescent nanocomposites for targeted bio-imaging. *RSC Advances* 5 (1): 20-26.

67. Deng W, Xie F, Baltar HTMCM, Goldys EM. (2013) Metal-enhanced fluorescence in the life sciences: here, now and beyond. *Physical Chemistry Chemical Physics* 15 (38): 15695-15708.
  
68. Darvill D, Centeno A, Xie F. (2013) Plasmonic fluorescence enhancement by metal nanostructures: shaping the future of bionanotechnology. *Physical Chemistry Chemical Physics* 15 (38): 15709-15726.
  
69. Chang Y-F, Tsao K-C, Liu Y-C, Chen Y-C, Yu P-C, Huang Y-C, Chou C. (2015) Diagnosis of human metapneumovirus in patients hospitalized with acute lower respiratory tract infection using a metal-enhanced fluorescence technique. *Journal of Virological Methods* 213 (0): 151-156.
  
70. Cristani M, Cheng DS, Murino V, Pannullo D. (2004) Distilling information with super-resolution for video surveillance. In *Proceedings of the ACM 2nd international workshop on Video surveillance & sensor networks*, pp. 2-11. New York, NY, USA: ACM
  
71. Moskovits M. (1985) Surface-enhanced spectroscopy. *Reviews of Modern Physics* 57 (3): 783-826.
  
72. Kneipp K, Moskovits M, Kneipp H. (2006) *Surface-Enhanced Raman Scattering: Physics and Applications*. Springer Berlin Heidelberg,

73. Le Ru EC, Blackie E, Meyer M, Etchegoin PG. (2007) Surface Enhanced Raman Scattering Enhancement Factors: A Comprehensive Study. *The Journal of Physical Chemistry C* 111 (37): 13794-13803.
74. Xu H, Aizpurua J, Käll M, Apell P. (2000) Electromagnetic contributions to single-molecule sensitivity in surface-enhanced Raman scattering. *Physical Review E* 62 (3): 4318-4324.
75. Doering WE, Nie S. (2002) Single-Molecule and Single-Nanoparticle SERS: Examining the Roles of Surface Active Sites and Chemical Enhancement. *The Journal of Physical Chemistry B* 106 (2): 311-317.
76. Kelly KL, Coronado E, Zhao LL, Schatz GC. (2003) The Optical Properties of Metal Nanoparticles: The Influence of Size, Shape, and Dielectric Environment. *The Journal of Physical Chemistry B* 107 (3): 668-677.
77. Moskovits M. (2005) Surface-enhanced Raman spectroscopy: a brief retrospective. *Journal of Raman Spectroscopy* 36 (6-7): 485-496.
78. Tian X, Guo J, Tian Y, Tang H, Yang W. (2014) Modulated fluorescence properties in fluorophore-containing gold nanorods@mSiO<sub>2</sub>. *RSC Advances* 4 (18): 9343-9348.
79. Stranahan SM, Willets KA. (2010) Super-resolution Optical Imaging of Single-Molecule SERS Hot Spots. *Nano Letters* 10 (9): 3777-3784.

80. Rees EJ, Erdelyi M, Kaminski Schierle G, S. , Knight A, Kaminski C, F. . (2013) Elements of image processing in localization microscopy. *Journal of Optics* 15 (9): 094012.
81. Schmid T, Opilik L, Blum C, Zenobi R. (2013) Nanoscale Chemical Imaging Using Tip-Enhanced Raman Spectroscopy: A Critical Review. *Angewandte Chemie International Edition* 52 (23): 5940-5954.
82. Feng S, Dong F, Sun S, Zou Y, Zhou C. (2014) Performance analysis for two typical spatial domain super-resolution reconstruction algorithms. *Proc. 2014 7th International Congress on Image and Signal Processing*:353-358.
83. Lewis A, Isaacson M, Harootunian A, Muray A. (1984) Development of a 500 Å spatial resolution light microscope: I. light is efficiently transmitted through  $\lambda/16$  diameter apertures. *Ultramicroscopy* 13 (3): 227-231.
84. Pohl DW, Denk W, Lanz M. (1984) Optical stethoscopy: Image recording with resolution  $\lambda/20$ . *Applied Physics Letters* 44 (7): 651-653.
85. Huckabay HA, Armendariz KP, Newhart WH, Wildgen SM, Dunn RC. (2013) Near-Field Scanning Optical Microscopy for High-Resolution Membrane Studies. *Methods in molecular biology (Clifton, N.J.)* 950: 373-394.
86. Betzig E, Lewis A, Harootunian A, Isaacson M, Kratschmer E. (1986) Near Field Scanning Optical Microscopy (NSOM): Development and Biophysical Applications. *Biophysical journal* 49 (1): 269-279.



87. Hell SW. (2009) Microscopy and its focal switch. *Nat Meth* 6 (1): 24-32.
88. Chen B-C, Legant WR, Wang K, Shao L, Milkie DE, Davidson MW, Janetopoulos C, Wu XS, Hammer JA, Liu Z, English BP, Mimori-Kiyosue Y, Romero DP, Ritter AT, Lippincott-Schwartz J, Fritz-Laylin L, Mullins RD, Mitchell DM, Bembenek JN, Reymann A-C, Böhme R, Grill SW, Wang JT, Seydoux G, Tulu US, Kiehart DP, Betzig E. (2014) Lattice light-sheet microscopy: Imaging molecules to embryos at high spatiotemporal resolution. *Science* 346 (6208).
89. Hirano Y, Matsuda A, Hiraoka Y. (2015) Recent advancements in structured-illumination microscopy toward live-cell imaging. *Microscopy* 64 (4): 237-249.
90. Hell SW. (2007) Far-Field Optical Nanoscopy. *Science* 316 (5828): 1153-1158.
91. Patterson G, Davidson M, Manley S, Lippincott-Schwartz J. (2010) Superresolution Imaging using Single-Molecule Localization. *Annual Review of Physical Chemistry* 61 (1): 345-367.
92. Evans CL, Xie XS. (2008) Coherent Anti-Stokes Raman Scattering Microscopy: Chemical Imaging for Biology and Medicine. *Annual Review of Analytical Chemistry* 1 (1): 883-909.
93. Raghunathan V, Potma EO. (2010) Multiplicative and subtractive focal volume engineering in coherent Raman microscopy. *J. Opt. Soc. Am. A* 27 (11): 2365-2374.

94. Kim H, Bryant GW, Stranick SJ. (2012) Superresolution four-wave mixing microscopy. *Opt. Express* 20 (6): 6042-6051.
95. Silva WR, Graefe CT, Frontiera RR. (2016) Toward Label-Free Super-Resolution Microscopy. *ACS Photonics* 3 (1): 79-86.
96. Sonntag MD, Pozzi EA, Jiang N, Hersam MC, Van Duyne RP. (2014) Recent Advances in Tip-Enhanced Raman Spectroscopy. *The Journal of Physical Chemistry Letters* 5 (18): 3125-3130.
97. Weber-Bargioni A, Schwartzberg A, Cornaglia M, Ismach A, Urban JJ, Pang Y, Gordon R, Bokor J, Salmeron MB, Ogletree DF, Ashby P, Cabrini S, Schuck PJ. (2011) Hyperspectral Nanoscale Imaging on Dielectric Substrates with Coaxial Optical Antenna Scan Probes. *Nano Letters* 11 (3): 1201-1207.
98. Jahncke CL, Paesler MA, Hallen HD. (1995) Raman imaging with near-field scanning optical microscopy. *Applied Physics Letters* 67 (17): 2483-2485.
99. Willets KA. (2014) Super-resolution imaging of SERS hot spots. *Chemical Society Reviews* 43 (11): 3854-3864.
100. Weber ML, Litz JP, Masiello DJ, Willets KA. (2012) Super-Resolution Imaging Reveals a Difference between SERS and Luminescence Centroids. *ACS Nano* 6 (2): 1839-1848.

101. Willets KA. (2013) Super-resolution imaging of interactions between molecules and plasmonic nanostructures. *Physical Chemistry Chemical Physics* 15 (15): 5345-5354.
102. Willets KA, Stranahan SM. (2012) Super-resolution imaging of diffusing analyte in surface-enhanced Raman scattering hot-spots, 8228:82280P-82280P-82288.
103. Willets KA, Stranahan SM, Weber ML. (2012) Shedding Light on Surface-Enhanced Raman Scattering Hot Spots through Single-Molecule Super-Resolution Imaging. *The Journal of Physical Chemistry Letters* 3 (10): 1286-1294.
104. Cullum BM, Li H, Hankus ME, Schiza MV. (2007) Characterization of multilayer-enhanced surface-enhanced raman scattering (SERS) substrates and their potential for SERS nanoimaging. *Nanobiotechnol* 3 (1): 1-11.
105. Hankus ME. (2008) Development and Characterization of Surface Enhanced Raman Scattering (SERS) Nanoimaging Probes. Masters. University of Maryland, Baltimore County, Baltimore, MD
106. Hankus ME, Cullum BM. (2006) SERS probes for the detection and imaging of biochemical species on the nanoscale, 6380:638004-638004-638012.

## Chapter 2: Optical Cross Talk

### 2.1. Introduction

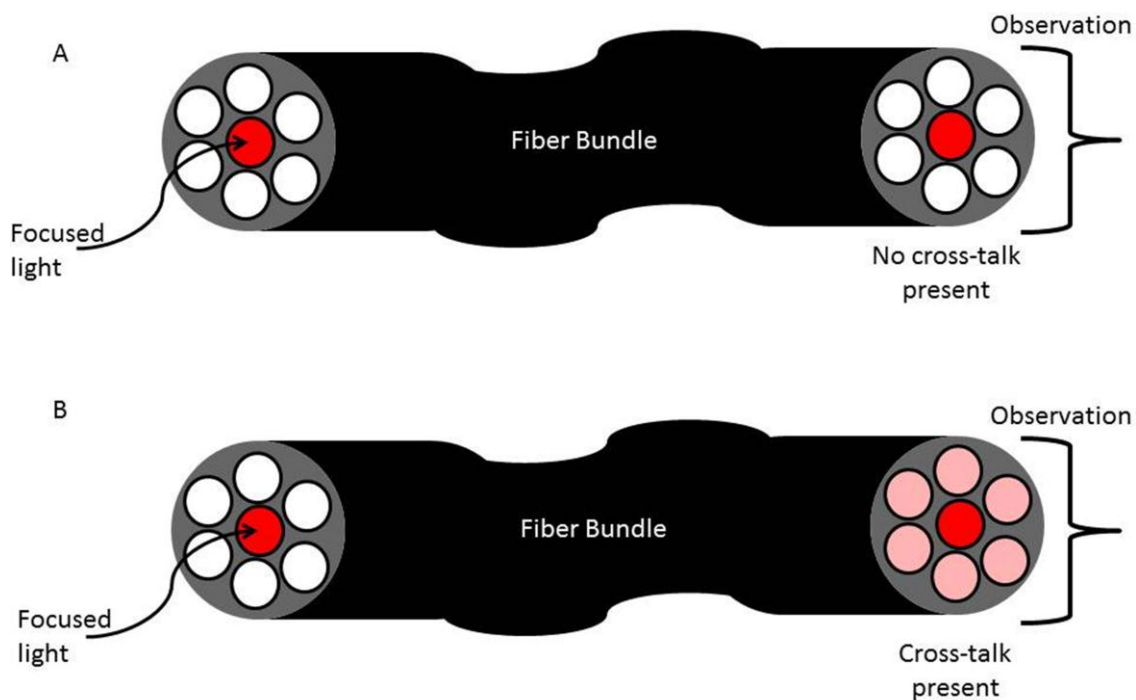
Near field scanning optical microscopy (NSOM) was the first technique to provide super resolution optical imaging.<sup>1</sup> Using a sufficiently small aperture and a strong enough signal, an NSOM device (metal-coated pipette tip or optical fiber) can provide indefinitely high resolution. Resolution degradation and therefore the utility of such an instrument are, however, often limited to the light (wavelength employed and throughput) that can actually be collected from the nanoscale aperture. When light is collected from a sub-wavelength aperture, the signal originates in the near-field and must progress up the waveguide (typically a fiber optic and henceforth used interchangeably) as an evanescent wave where the power of the light transmitted to the far-field is dependent to the fourth power of the diameter of the aperture and intensity decreases with the inverse square of distance.<sup>2,3</sup> Once the fiber has widened enough for the photon to “exist” (i.e. approximately one-half the wavelength of the light being employed), the evanescent wave scatters into the far-field and a propagating mode of the light can then travel up the fiber via total internal reflection.

Since the diameter of the aperture and the distance the evanescent wave must travel are two defining characteristics of the amount of light transmitted from the near-field to the far-field (i.e. measureable light from a tapered fiber), several key parameters of the bundle (i.e. aperture size and taper length) must be taken into account. One such parameter is the taper length, which controls the amount of light lost in the near-field due to the distance dependence of the non-propagating evanescent wave that is collected into

the fiber. Additionally, the aperture size parameter drastically reduces the amount of light that can enter the fiber as the aperture size decreases.

Multiple fiber optics can be used in parallel such as in a system employing fiber imaging bundles. By having a core material and cladding material that have different refractive indices, light can travel into the core material and totally internal reflect before being transmitted to the distal end of the bundle. Imaging bundles have two or more fiber elements in a single bundle that run in parallel and are often ordered from one end to the other to allow image transmission.<sup>4, 5</sup> However, any light leaking from one fiber optic element to the next can degrade the resolution and is termed cross-talk. While imaging fibers are manufactured in such a way that the cross-talk is minimal, manipulating the imaging fiber and/or lower energy light can cause undesired cross-talk.<sup>6</sup> Therefore, to mitigate cross-talk in a imaging fiber bundles, the bundle should be kept large and short enough to reduce such adverse coupling between two adjacent fibers.

Measuring cross-talk is completed by ensuring that the observed light emitted from a single fiber element of an imaging bundle is due to the illumination of a single fiber element within the bundle. The most direct measurement of cross-talk can be completed by illuminating one fiber in a bundle with a tightly focused laser<sup>6</sup> or white-light source<sup>7</sup> while imaging the proximal face of the fiber bundle and accounting for the amount of light in the fibers adjacent to the fiber being illuminated. A cartoon representation of this is shown below in Figure 2.1. Alternative methods for use when the fiber elements are below the diffraction-limit of light (thereby excluding optical focusing of an electromagnetic field into a single fiber element) include using a diffused white light source incident on the distal end of the bundle while video-recording the angle dependent



**Figure 2.1:** Cartoon representation of the traditional way of measuring cross-talk whereby a focused light (either a laser or white light) is coupled into a single fiber element while the output is measured on the opposite end. A) represents a fiber bundle with no cross-talk while B) represents a fiber bundle with cross-talk.

transmission of the proximal end.<sup>8</sup> This results in different frames having groups of fibers illuminated. In some series of frames, a single fiber-element is illuminated while the surrounding fibers are not and vice-versa, allowing for the quantification of cross-talk.

Currently, imaging probes have been tapered, etched and coated in metal to create apertures of varying sizes (down to sub-diffraction-limited) capable of producing surface enhanced Raman scatter (SERS) images, increasing the resolution and versatility of the imaging bundle.<sup>8, 9</sup> In doing so, the core material becomes smaller in diameter with a commensurate decrease in the cladding thickness. As the cladding thickness decreases, the potential for cross-talk increases due to an increase in the probability of light fully

penetrating the cladding and leaking into an adjacent fiber element. Due to using sub-wavelength apertures, a new way of imaging fiber bundles is necessary since the diffraction-limit of light precludes the coupling of a laser (or white light source) into an individual fiber element within the imaging fiber bundle.

Fiber bundle arrays are 1mm in diameter and consist of 30,000 individual fiber elements that are 4 $\mu$ m in diameter. Modifying the size and surface through tapering whereby the total bundle is approximately 20 $\mu$ m and the fiber elements are approximately 50nm in diameter prohibits the use of traditional methods of cross-talk measurement due to a nearly zero efficiency of transmission at sub-wavelength dimensions. Previously, fluorescent beads have been used as light sources in the tapered end of the probe for cross-talk analyses on such tapered probes.<sup>9</sup> The fluorescent beads were chemically cross-linked to the silica core of an individual fiber element resulting in fluorescence originating inside an individual nanowell and propagating to the proximal end. However, stochastic fluorescent events were not observed inasmuch as there were no individually illuminated fiber elements; either all the fiber elements were illuminated or none were illuminated and cross-talk could not be determined.<sup>9</sup> Furthermore, this precludes a measurement of crosstalk when the fiber bundles are tapered to a diameter that is on the same order of magnitude as the size of the beads because they are not likely to fit inside the nano-well. Moreover, as sensing modalities continue to decrease in size (i.e. smaller pixels, smaller apertures) and additional SERS geometries arise,<sup>10</sup> quantification of cross-talk in arrayed platforms are becoming increasingly significant. Understanding and characterizing cross-talk within different geometries, including that of arrayed fiber

optics, is necessary to ensure accurate spatial information is obtained when imaging at sub-wavelength scales.

This chapter highlights progress towards developing a robust protocol for measuring cross-talk in such arrays. Quantum dots are employed as individual point sources within the nanowells due to their small (4-5nm) diameters. Due to the quantum dot's high quantum efficiency, this arrangement allows light to originate in individual wells and the quantification of cross-talk realized. Furthermore, the on/off nature observed with use of fluorescent beads is also overcome using this method.

## **2.2. Experimental**

### *2.2.1 Fiber Bundle Preparation*

The preparation and fabrication of fiber bundles have been previously described.<sup>8, 11-13</sup> In short, fiber bundles were purchased from Sumitomo Electric Industries (IGN-08/30) and were used as received. A 7.5 cm long section is cut from the bundle and mechanically polished using lapping film with grits of 5-, 3-, 1-, and 0.3 $\mu$ m (Thor Labs). After each lapping film is used, the bundle is washed thoroughly and visually inspected for abnormal defects with an optical microscope.

Polished bundles are then tapered using a Sutter P-2000 micropipette puller instrument. Specialized programs are used to taper fiber bundles with different diameters while maintaining image coherency from end-to-end. See Appendix A for a program used, a listing of the parameters employed, and the resulting fiber element diameter achieved. Following tapering, each fiber bundle is also visually inspected via optical microscope to ensure the tapered end appears flat and not chipped, cracked, or broken.



Following polishing and tapering to the desired dimensions (when using tapered bundles), fiber bundles are etched using a 25% (v/v%) hydrofluoric acid solution in water. The tips of the bundles are submerged into the etchant solution at a constant depth. Untapered bundles are etched for 60 seconds while tapered bundles are etched for 150 seconds. Etching is subsequently quenched by submerging the tips into double distilled deionized water with sonication and/or manual agitation for at least 150 seconds.

Metal deposition on the fiber bundles is achieved using a Denton Vacuum Explorer physical vapor deposition system. Fiber bundles are suspended on a rotating motor at approximately 45° above a tungsten evaporating boat with Ag shot (99.99% pure, Kurt J. Lesker Company, Clairton, PA) in it. The motor is then rotated under vacuum ( $< 5 \times 10^{-6}$  torr) and metal is deposited onto the etched end of the fiber bundle at rates of 0.4 Å/s – 1.0 Å/s. Total Ag deposited on the untapered bundles were approximately 75nm while tapered bundles had approximately 20nm Ag deposited. See Appendix B for a complete description of the deposition process.

Bundles can also be reused for acquisition of subsequent images by thorough cleaning. To ensure complete removal of QDs during such cleaning, the bundles are soaked in 6.0N HNO<sub>3</sub> for at least one hour. This dissolves the Ag and the QDs. Cleaned and stripped bundles are then rinsed with deionized water (DI H<sub>2</sub>O) and left in an oven (55° C) for at least two hours, but typically overnight, to ensure the nano-wells were dry.

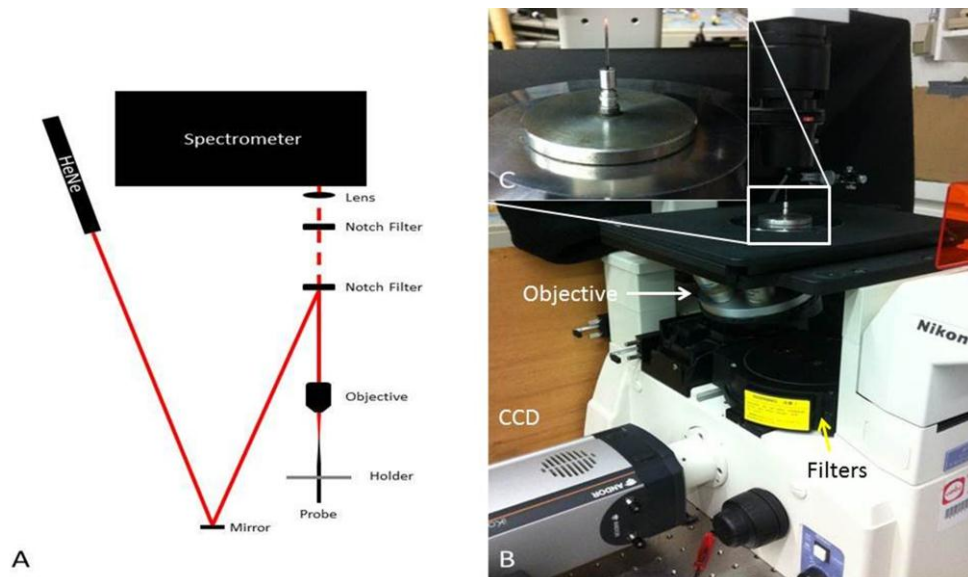
### 2.2.2 Quantum Dots

Quantum dots were purchased from CytoDiagnostics (FN-665-A-5MG; Burlington, ON, Canada) and used as received. Several concentrations of QDs were made in toluene with

concentrations ranging from  $6 \times 10^8$  QD/L to  $6 \times 10^{16}$  QD/L. Prior to deposition of the QDs on the fiber bundles, each solution was vortexed for 15 seconds, sonicated for 60, seconds and vortexed again for 15 more seconds to ensure that the QDs were not aggregating and fully separated in the solution. These solutions are stored in the refrigerator while not in use.

### 2.2.3 Spectroscopy System

All spectra were obtained with a custom-built spectrometer. This spectroscopy system was arranged in backscatter geometry and employs an Acton SpectraPro 500i spectrometer for spectral dispersion (see Figure 2.2A). All spectra were obtained with 2-second acquisition times and nine accumulations following excitation with a 633nm laser (JDS Uniphase, model 1145; 25mW). The distal end of the fiber bundles were placed at the focus of a 10X microscope objective (Nikon Plan 10 X/0.25) on a stage. The bundle



**Figure 2.2:** The custom-built spectrometer used for spectroscopic analysis, where the red line is representative of the laser line, and the dashed line is the collected fluorescence (A); Microscope used for imaging of the fiber bundles (B), close-up of a tapered fiber bundle used.

was then positioned in the x, y, and z planes for optimal signal-to-noise ratio of the fluorescence emitting from the QD.

#### *2.2.4 Microscopic Imaging System*

Bright field and fluorescence images of the bundles with QDs embedded within the nanowells were obtained using an inverted, epi-fluorescence microscope (TE2000-S; see Figure 2.2B), recording transmitted light through the proximal end of an etched, metal coated fiber bundle (see Figure 2.2B, C). A filter cube containing a 594nm - 651nm excitation filter and emission band pass of 669nm - 726nm for transmission of the fluorescent light was employed. 20X magnification was used for all measurements, unless otherwise noted. Images of the bundles were captured on either an Andor iKon-M CCD with 30-second acquisition times averaged over 6 frames or an SBIG ST-7XE (Santa Barbara Instrument Group) imaging CCD with a single frame ranging from 300 - 900 seconds. The image illumination of the tapered probes was not uniform and therefore the center portion of the image was used where illumination was more consistent. The pixel-distance relationship for determination of fiber element diameter was determined using a standard microscope calibration slide with 20 - 160 $\mu$ m calibration bars. Image analysis was completed using Image J (v. 1.48; National Institute of Health).

### **2.3. Results and Discussion**

#### *2.3.1 Quantum Dot Loading*

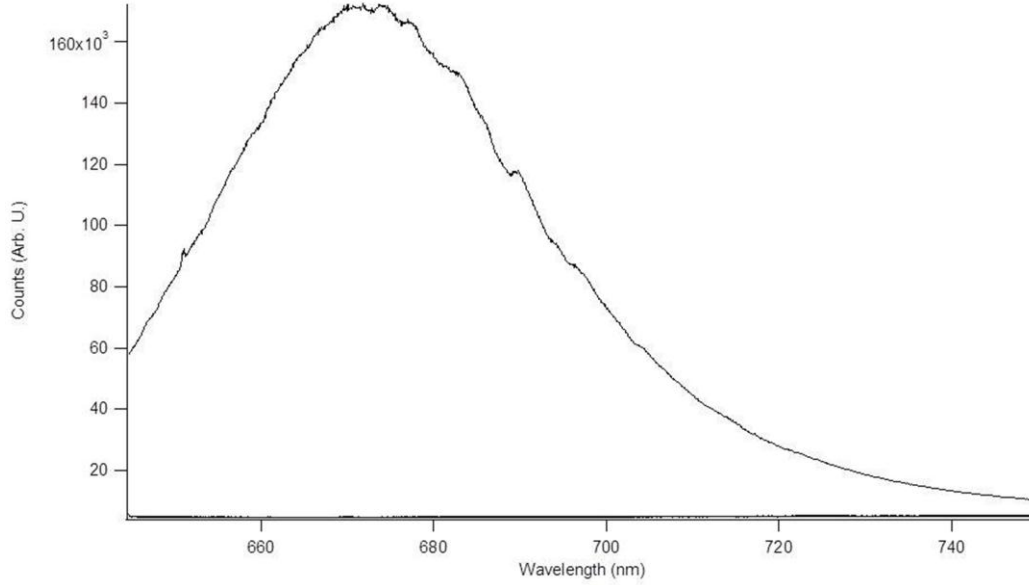
QDs must be diluted to an appropriate concentration and loaded into the prepared etched and coated fiber bundles in order to sparsely populate the fiber bundles with QDs for acquiring cross-talk measurements. To ensure QDs did not occupy adjacent fiber

elements, QD concentrations were kept less than 1 QD per 100 fiber elements resulting in no more than approximately 3,000 QD over the entire fiber bundle. The concentrations to be used were conservatively approximated by calculating the volume of each fiber well that was to be occupied and then diluting the QDs appropriately based upon the manufacture data of the QD concentration received in the stock solution. Assuming a 4μm fiber element, and an anisotropic etching rate of 150nm/min to achieve filling 1 out of every 100 fiber elements, this relationship can be employed:

$$\left[ \text{QD}/\text{L} \right] = \frac{1}{\left( \frac{\pi \times r^2 \times H}{FE_{frac}} \right)} = \frac{1}{\left( \frac{\pi \times 25nm^2 \times 150nm}{100} \right)} = 1.77 \times 10^{12} \text{ QD}/\text{L}$$

Eq. 2.1

To ensure that there are QDs embedded as expected, the concentration of QDs was varied from what was found from Eq. 2.1 to achieve either more or less fiber wells illuminated during interrogation. As seen in Figure 2.3, as the concentration of QDs is increased, there is a detectable luminescence consistent with QDs only when the QDs were at their highest measured concentration ( $6 \times 10^{16}$  QD/L;  $\lambda_{max} = 672\text{nm}$ ). At the highest concentration measured there were still only approximately 20 measureable points out of approximately 25,000 fiber elements observed, resulting in less than one-tenth of one percent of measurable observations compared to the total number of fiber elements. While the concentration of QDs needed to achieve luminescence was larger than expected, the luminescence was monitored with each addition of a diluted QD solution, ensuring that luminescence was not detectable until the  $6 \times 10^{16}$  QD/L was used, as shown in Figure 2.3.



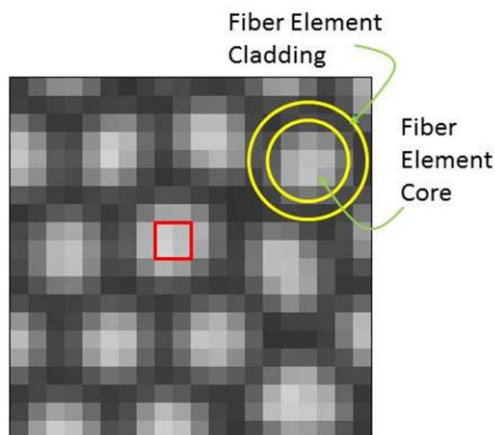
**Figure 2.3:** Luminescent spectra of the quantum dots at concentrations ranging from 0 QD/L to  $6 \times 10^{16}$  QD/L. The only concentration producing a luminescent spectrum is at  $6 \times 10^{16}$  QD L<sup>-1</sup>.

### 2.3.2 Cross-talk evaluation

Fiber imaging probes were evaluated before and after QD deposition via spectroscopic and imaging analyses. Using both techniques validates the presence of QDs within the fiber bundle. Furthermore, fiber bundles were analyzed with increasing concentrations of QDs in order to add the minimal number of QDs necessary for cross-talk measurements and ensure sparsely populated fiber element wells.

#### 2.3.2.1 Untapered Fiber Bundles

To determine the cross-talk present for a particular group of neighboring fiber elements, first the fiber bundle was imaged onto the CCD for identification of fiber elements and fiber cladding. The pixels associated with each element and its surrounding cladding was identified by the areas of high and low intensity, respectively, when imaged with a broadband light source, as seen in Figure 2.4. A 2x2 region of interest (ROI) is chosen



**Figure 2.4:** A 2x2 box is outlined around four pixels in the manner in which data were obtained for this cross-talk study. The 2x2 box was chosen because it includes only pixels that are from the luminescence of the fiber element and excludes the surrounding fiber cladding resulting in comparable data from image-to-image.

such that only the interior of the fiber element is included, ensuring that the decreased intensity of the cladding is not incorporated into the cross-talk measurement. When selecting the ROI, it was ensured that the brightest pixel of the fiber element was incorporated to represent the total signal (sum of the individual pixels) as accurately as possible. Furthermore, all values reported below are provided with 95% confidence interval, unless otherwise noted.

Figure 2.5 shows a white light transmission image of a fiber bundle (Figure 2.5A) and two concentrations of QDs (Figure 2.5B,  $6 \times 10^{12}$  QD/L; Figure 2.5C,  $6 \times 10^{16}$  QD/L) at the same spatial location. This figure shows an increase in signal intensity in one or more fiber elements while the cladding remains dark (Figure 2.5C) as evident through the central pixel having the most intensity and a ring of low intensity around it. This is important to note as foreign material can unintentionally adsorb onto the proximal surface creating a luminescent area that is not bounded by the cladded and is therefore on top of

the surface being imaged and not a QD. During analysis, each illuminated area was analyzed and confirmed to have no foreign material present both prior to and after addition of the QDs via white light images similar to that in Figure 2.5A whereby the fiber was placed on the inverted microscope and illuminated from the proximal end.

Therefore a group of fiber elements possessing cross-talk is defined as a single fiber element with a QD present (manifested by a single, brightly luminescent fiber element) and any of the surrounding 6 fiber elements having an intensity value above the average of the background intensity of a representative sample of all the fiber elements with no QDs present. Cross-talk is calculated by measuring the ratio of the background-subtracted signal from the central fiber with respect to each of the surrounding background-subtracted fibers. Threshold values for what to consider a QD were calculated at the 95% confidence level based on the analysis of 50 fiber elements with no QDs present equally spread across the imaging area. The amount of light (percentage) leaking from the central fiber into each surrounding fiber was calculated individually and then averaged together with a reported confidence of 95%.



**Figure 2.5:** White light image of a small area on a fiber bundle (A), fluorescent image of the same bundle that has been dip coated in a quantum dot solution of  $6 \times 10^{14}$  QD/L (B), and a fluorescent image of the same bundle that has been dip-coated in a quantum dot solution of  $6 \times 10^{16}$  QD/ L (C). All images are of the same area and have the same contrast for comparison purposes.

Expressed mathematically:

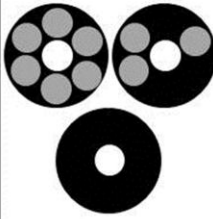

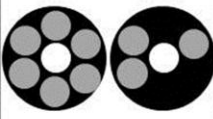
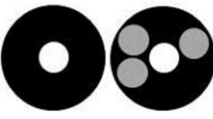
$$CT = \frac{1}{n} \sum_{i=1}^n \frac{ROI_i}{QD} \quad \text{Eq. 2.2}$$

Where  $n$  is the number fiber elements in group ( $n = 6$ ),  $ROI_i$  is the sum total of the 2x2 background subtracted ROI associated with the neighboring fiber element,  $i$ .  $QD$  is the background subtracted sum total intensity of the central fiber element within the ROI and represents the intensity of the QD emission.

Cross-talk can manifest itself in two forms: a symmetric illumination of the six surrounding fiber elements or in a non-symmetrical form where only some of the fiber elements are illuminated. Pictorial representations and tabulated data are found in Table 2.1. From these studies, it was found that 12% of the fiber elements observed had a symmetric illumination of the fiber elements surrounding a central fiber element with a QD present. Cross-talk for these was shown to have  $10 \pm 2\%$  of the total luminescence in the surrounding fibers. The combination of symmetrical, non-symmetrical, and no illumination yields the most comprehensive and liberal measure cross-talk in which all possible combinations of measure are incorporated. This yields a measure of  $2.2\% \pm 0.6\%$  of the light intensity leaking for the central fiber element to surrounding fiber elements. Less inclusive scenarios investigating the amount of light leaking from fiber-to-fiber are 1) a measure of all the groups of fiber elements with *some* of the adjacent fiber elements illuminated (excluding groups with no measurable intensity) and 2) a measure of all of the groups of fiber elements with some or none of the adjacent fiber elements illuminated. The data for these scenarios are  $6\% \pm 1\%$  and  $1.0\% \pm 0.4\%$  of the light leaking from the core to the adjacent fibers and comprise approximately 27% and 88% of



**Table 2.1:** Summary of the cross-talk measurements of light leaking from a central fiber element illuminated with a QD to the adjacent fiber elements in untapered (4000nm) and tapered (271nm and 32nm) fiber bundles. To help aid in understanding, the groups are represented in a visual form whereby the central circle is illuminated completely (white) to represent the fiber illuminated by a QD while the surrounding fibers are either fully illuminated (gray, cross-talk), partially illuminated or not illuminated (no measurable cross-talk). \*Error is defined at the 95% confidence interval.

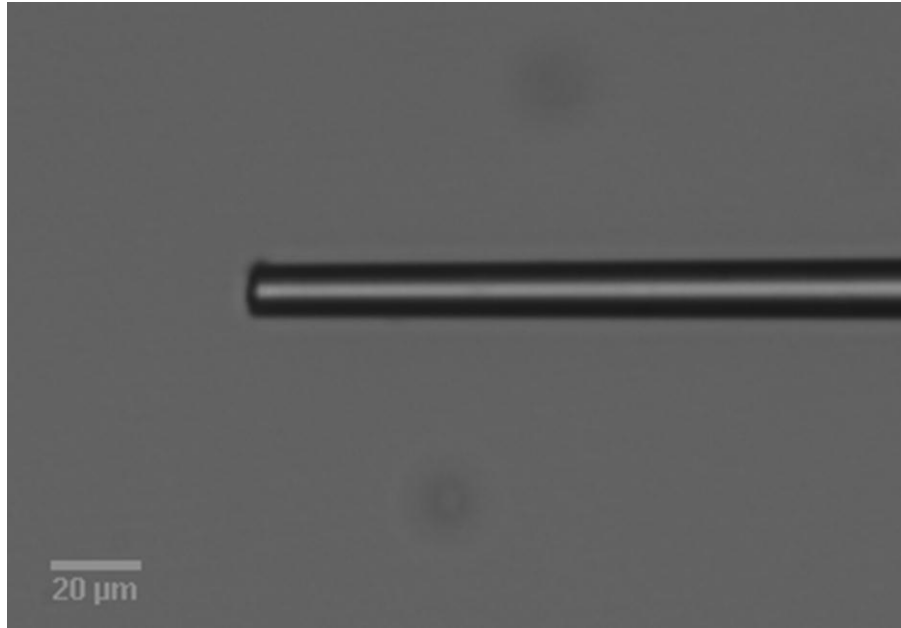
	Type of groups Fiber element diameter in nm				
Average intensity leaked from middle fiber to adjacent fibers (%) $\pm$ Error* (%)	<b>4000</b>	$2.2 \pm 0.6$	$10 \pm 2$	$6 \pm 1$	$1.0 \pm 0.4$
	<b>271</b>	$0.5 \pm 0.9$	N/A	N/A	$5 \pm 12$
	<b>32</b>	$1.5 \pm 0.5$	$3 \pm 1$	$1.8 \pm 0.6$	$0.6 \pm 0.4$

the total recorded measurements, respectively. It is noteworthy that 88% of the total measurements only have 1.4% of the luminescence leaking from the core fiber element to the adjacent ones at the 95% confidence level. While 39% of the measured fiber elements had light leaking from the central fiber element (QD) into it, these data suggest that crosstalk is *not* a significant source of interference when imaging with non-tapered bundles.

Generally, however, it was observed that the QDs showed either no measurable cross-talk or they showed fiber elements that had luminescence present in adjacent fibers, *but not all 6 adjacent fibers*. Furthermore, determining if the QD is seated in the bottom of the nanowell or has adsorbed to a portion of the cladding that is not coated in metal was not feasible due to instrumentation needed for such measurements. However, this scenario could increase the cross-talk preferentially to one or several adjacent fiber element(s), not all 6 adjacent fiber elements as a QD seated in the bottom of the nanowells evenly luminescing would. The non-symmetric leakage may be due to QD(s) not seated in the bottom of the well and may be situated on the side of the well, closer to the fiber element that has a higher percentage of cross-talk. Quantum dot seating within a well will affect the average and standard deviation of such a measurement, and cause the data to trend towards larger cross-talk values if it is occurring. Therefore, with cross-talk measured at an average of  $2.2\% \pm 0.6\%$ , QD seating is not a significant issue.

#### 2.3.2.2 – Tapered Fiber Bundles

As the fiber bundles are tapered further and the individual fiber elements reach nanometric dimensions, as shown in Figure 2.6, the previous methods of detecting cross-talk are no longer feasible because the fiber element diameter is too small to focus a laser into a single element.<sup>6, 7</sup> Additionally, the use of diffused light, as described in previous reports,<sup>8, 9</sup> is not reasonable as one cannot preclude the scenario in which scattered light fills adjacent fibers elements resulting in artificially high cross-talk. To avoid chemical modification or cross linking on the surface of the probes, as previously described,<sup>9</sup> and therefore potentially inhibit the ability of light transmission and/or total internal reflection, the use of QD has become a significant venture for determining the cross-talk.



**Figure 2.6:** A Tapered fiber bundle measuring approximately  $13\mu\text{m}$  in diameter, providing fiber elements that are approximately  $32\text{nm}$  in diameter.

Furthermore, use of QDs is a ubiquitous approach as the QDs are small ( $\sim 5\text{nm}$ ) compared to most commercially available tapered apertures ( $\geq 50\text{nm}$ ).

Fiber-element well size for tapered fiber bundles is estimated for the volume and concentration needed for cross-talk measurements. To determine the well size within the fiber bundle, two parameters must be known: 1) the size of the individual fiber elements and 2) the rate of etching. It is further assumed that each fiber element is perfectly circular and the etching process proceeds to create a perfect cylinder, as is expected through the anisotropic etching of  $\text{SiO}_2$  with  $\text{HF}$ .<sup>14, 15</sup> The etching rate is known to be approximately  $150\text{nm}/\text{min}$  in a 25%  $\text{HF}$  (v/v%) solution in water.<sup>8, 16</sup> The size of the individual fiber elements can be estimated by using a calibrated optical microscope to examine the cross-section of a tapered (or untapered) fiber bundle (shown in Figure 2.6) and employing the following relationship:

$$D_{FE} = 2 \times \sqrt{\frac{\left(\frac{D_{FB} \times A}{2}\right)^2 \times \pi \times B}{C}} \quad \text{Equation 2.2}$$

where:

- $D_{FE}$  is the diameter of the fiber elements (in meters)
- $D_{FB}$  is the diameter of the fiber bundle, as imaged on the microscope (in meters)
- $A$  is the active area to cladding ratio, as defined by the manufacturer; this is the area of active fiber elements (unit-less ratio)
- $B$  is the packing density for hexagonally packed fiber elements and is used as an estimation of the packing density of the fiber elements in the array (unit-less)
- $C$  is the number of fiber elements present in the fiber bundle array and is defined by the manufacturer (or could be counted if few enough elements are present)

This relationship extends to all fiber-bundle arrays that are hexagonally packed. For this particular system,  $A$  is 0.9,  $B$  is approximately 0.9069, and  $C$  is 30,000 fiber elements based on manufacturers documentation. With this information, the volume of the etched cylinder (i.e. nano-well) can be calculated.

To examine and confirm consistency between tapered and non-tapered fiber bundles, additional tapered fiber bundles were used to evaluate cross-talk. Fiber bundles with individual fiber elements of approximately 271nm and 32nm were used. A similar process as above was followed, with increased drying time between adding the toluene and making the final measurements. The bundles were left over night after the QDs were added to ensure that all the toluene evaporated. The data are tabulated in Table 2.1.

Upon evaluation of the larger (271nm fiber elements) fiber bundle, nine groups were measured with QDs present; 11% (one out of the nine) possessed a measurable amount of light leaking from the center fiber to adjacent fibers with  $5\% \pm 12\%$  of the light leaking. Therefore, the cross-talk associated with this fiber bundle (271nm fiber elements) is significantly different than the cross-talk associated with an untapered fiber bundle (4 $\mu$ m fiber elements). Less than 2% of the total number of fiber elements evaluated possessed any cross-talk. When evaluating all fiber elements with QDs present,  $0.5\% \pm 0.9\%$  of the light leaking from the center to adjacent fibers was measured. The error of these measurements is high because the one fiber element that had cross-talk is approximately 28% and is observed as a single fiber elements possessing this high percentage of cross-talk, creating a large error associated with the one measurement. However, the overall amount of cross-talk is still consistent with what was previously observed with nanobeads.<sup>9</sup> Furthermore, the number of fiber elements that had any cross-talk present, excluding the fiber elements with QDs in them, were less than 2%.

The smaller fiber bundle with fiber elements approximately 32nm in diameter showed slightly higher cross-talk than the bundle with 271nm fiber elements, but is not statistically different than the fiber bundles with 4 $\mu$ m fiber elements or the fiber bundles with 271nm fiber elements. A total amount of cross-talk of  $1.5\% \pm 0.5\%$  was determined. In the image, there were 6 QDs identified, of which 33% possessed cross-talk with illumination of all 6 surrounding fiber elements, 50% of the groups had partial illumination of the surrounding fiber elements, and 17% of the groups had no illumination of the surrounding elements.

The bundle with 32nm fiber elements had 65% of the total fiber elements adjacent to the QDs possessing cross-talk. This is significantly higher when compared to untapered bundles. However, as shown above, at the 95% confidence level, there is at most 2% of the total luminesces leaking from fiber-to-fiber. This suggests that as the fiber bundle diameter decreases, the total number of elements with cross-talk increases, but the total amount of cross-talk (i.e. percentage of light leaking into an adjacent fiber) does not increase. This also makes sense with respect to previous reports<sup>9</sup> whereby a polystyrene sphere functionalized with a dye molecule was attached to the metal-coated tips of the etched fiber elements. This study is flawed such that the highest surface area of the metal is at the apex of the tip, providing the highest likelihood of a binding event, at the outermost region of the fiber element significantly increasing the likelihood of cross-talk. Our technique, using embedded QDs in the nano-wells, is a better representation of how much light will actually leak from one fiber element to another fiber element (the definition of cross-talk) when imaging.

While cross-talk using fiber-elements at sub-50 nm diameters does not provide a significant source of interference when imaging, it is worth noting that as the diameter of the fiber elements decrease, the overall time of image acquisition will increase due to the attenuated throughput of the sub-diffraction-limited apertures. Therefore, it is useful to pursue ventures that will subsequently increase resolution without necessarily decreasing the aperture size of the fiber elements. This will be discussed in Chapter 3 of this dissertation.

## **2.4. Conclusion**

Fiber bundles consisting of 30,000 individual fiber elements can be tapered to nanometric dimensions and therefore require a new way of quantifying cross-talk between adjacent fiber elements. Cross-talk measurements were found to impart an insignificant amount of light leaking from a central fiber element to the surrounding fiber elements. The amount of cross-talk for untapered fiber bundlers was  $2.2\% \pm 0.6\%$  at the 95% confidence level. This is consistent or provided a lesser amount of cross-talk with previous cross-talk measurements of approximately 7% above background intensity. Tapered fiber bundles (down to individual fiber elements of 32nm in diameter) showed a comparable degree of cross-talk (approximately 2%) which is also consistent with previous findings as well. This method circumvents the physical modification of the surface of the bundle set forth previously while providing point source illumination in a sparsely populated, independent fashion. In both tapered and untapered fiber bundles, the average amount of cross-talk at the 95% confidence level was 2%. However, using sub-diffraction-limited fiber elements tend to have a greater percentage of fiber elements possessing cross-talk. This study shows that since the average cross-talk at the 95% confidence level is not statistically different for both commercial bundles and bundles modified to have sub-diffraction-limited fiber elements, cross-talk is not a significant source of interference in these measurements.

## **2.5. Acknowledgments**

The researchers are thankful for Jeffrey Oleske from Andor Technology for the recommendation and loaning of the Andor iKon-M CCD used within this manuscript.

## 2.6. References

1. Betzig E, Lewis A, Harootunian A, Isaacson M, Kratschmer E. (1986) Near Field Scanning Optical Microscopy (NSOM): Development and Biophysical Applications. *Biophysical journal* 49 (1): 269-279.
2. Weiner J. (2009) The physics of light transmission through subwavelength apertures and aperture arrays. *Reports on Progress in Physics* 72 (6): 064401.
3. Hecht B, Sick B, Wild UP, Deckert V, Zenobi R, Martin OJF, Pohl DW. (2000) Scanning near-field optical microscopy with aperture probes: Fundamentals and applications. *The Journal of Chemical Physics* 112 (18): 7761-7774.
4. Walt DR. (2010) Fibre optic microarrays. *Chemical Society Reviews* 39 (1): 38-50.
5. Flusberg BA, Cocker ED, Piyawattanametha W, Jung JC, Cheung ELM, Schnitzer MJ. (2005) Fiber-optic fluorescence imaging. *Nat Meth* 2 (12): 941-950.
6. Chen X, Reichenbach KL, Xu C. (2008) Experimental and theoretical analysis of core-to-core coupling on fiber bundle imaging. *Opt. Express* 16 (26): 21598-21607.
7. Huang L, Oesterberg UL. (1995) Measurement of cross-talk in order-packed image fiber bundles, 2536:480-488.
8. Hankus ME, Li H, Gibson GJ, Cullum BM. (2006) Surface-Enhanced Raman Scattering-Based Nanoprobe for High-Resolution, Non-Scanning Chemical Imaging. *Analytical Chemistry* 78 (21): 7535-7546.



9. Kiser JB, Cullum BM. (2010) Optical cross-talk and surface characterization of SERS nanoimaging bundle substrates, 7674:76740D-76740D-76748.
10. Strobbia P, Languirand E, Cullum BM. (2015) Recent advances in plasmonic nanostructures for sensing: a review. *OPTICE* 54 (10): 100902-100902.
11. Hankus ME, Gibson G, Chandrasekharan N, Cullum BM. (2004) Surface-enhanced Raman scattering (SERS): nanoimaging probes for biological analysis, 5588:106-116.
12. Hankus ME, Cullum BM. (2006) SERS probes for the detection and imaging of biochemical species on the nanoscale, 6380:638004-638004-638012.
13. Hankus ME, Gibson GJ, Cullum BM. (2005) Characterization and optimization of novel surface-enhanced Raman scattering (SERS)-based nanoimaging probes for chemical imaging, 6007:600704-600704-600711.
14. Kovacs GTA, Maluf NI, Petersen KE. (1998) Bulk micromachining of silicon. *Proceedings of the IEEE* 86 (8): 1536-1551.
15. Schwartz B, Robbins H. (1976) Chemical Etching of Silicon: IV . Etching Technology. *Journal of The Electrochemical Society* 123 (12): 1903-1909.
16. White DJ, Mazzolini AP, Stoddart PR. (2008) First-approximation simulation of dopant diffusion in nanostructured silica optical fibres. *Photonics and Nanostructures - Fundamentals and Applications* 6 (2): 167-177.
17. Maenosono S, Dushkin CD, Saita S, Yamaguchi Y. (1999) Growth of a Semiconductor Nanoparticle Ring during the Drying of a Suspension Droplet. *Langmuir* 15 (4): 957-965.

18. Kong YL, Boulogne F, Kim H, Nunes J, Feng J, Stone HA. (2015) Deposition of Quantum Dots in a Capillary Tube. *Langmuir* 31 (45): 12560-12566.
19. Crivoi A, Duan F. (2014) Three-dimensional Monte Carlo model of the coffee-ring effect in evaporating colloidal droplets. *Scientific Reports* 4: 4310.

## **Chapter 3: Super-Resolution Reconstruction with a Magnified Fiber Imaging Bundle**

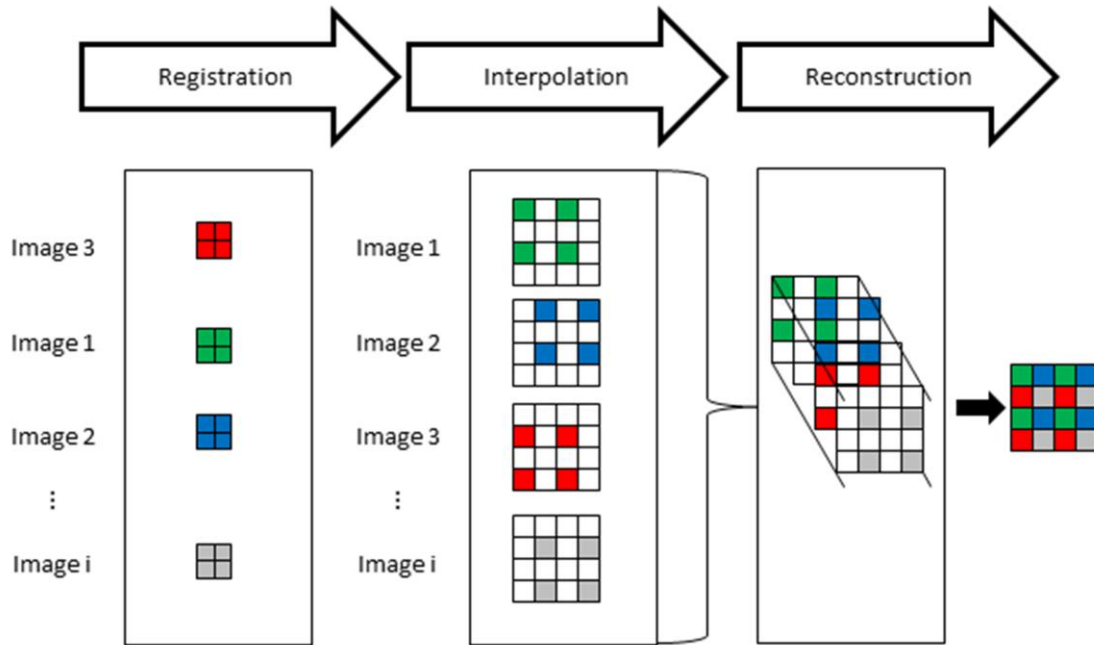
### **3.1 Introduction**

The past several decades have seen significant advances in super-resolved chemical imaging, most notably with fluorescence imaging.<sup>1-5</sup> Reaching below the diffraction-limit of light allows for the probing of molecular interactions at or near the molecular scale. However, with all super-resolving techniques, increasing spatial resolution comes at a cost of temporal resolution many times quite considerably with few to none capable of real-time imaging. Despite this, dynamic interactions on the nanoscale have become of great interest and numerous techniques have been developed to further increase spatial resolution while retaining dynamic capabilities.<sup>6-8</sup> Recently, several techniques (e.g. dynamic light sheet microscopy, super resolution optical fluctuation imaging, etc.) have been used to monitor dynamic interactions in three dimensions.<sup>1</sup> Unfortunately, most super resolution techniques currently employed rely on the use of exogenous dyes as an indirect measure of location and/or concentration and may not represent the true dynamics of the system.

The spatial resolution of any particular imaging system can be defined by the hardware employed (i.e. pixel density of the camera used) or the optics used (e.g. point spread function, aberrations, etc.). To increase the spatial resolution of a system, one must change either, or both, hardware and optics. Changing the hardware requires an increase in pixel density, which is often produced by reducing the size of each individual pixel. Similarly, employing better optics or changing to more appropriate optics for the

application is required to increase resolution in this manner. Both routes can be financially prohibitive and in some cases technologically limited.

To overcome these challenges, to some extent, one can use post-acquisition processing power instead. Post-processing of images can provide image enhancements (e.g. resolution, contrasting, false coloring, etc.) to improve the interpretation of the individual or series of images obtained. To increase the spatial resolution, one can employ super-resolution reconstruction (SRR) techniques.<sup>9-12</sup> While an overview of these SRR techniques were provided in Chapter 1 of this dissertation, this chapter will provide an in-depth discussion and evaluation of dithering based image reconstruction. This is performed by oversampling the imaging area and using algorithms and statistics to elucidate the high frequency information (i.e. the details that are smaller than the pixel information obtained). Oversampling of the image area requires the acquisition of multiple images of the same sample location; each slightly dithered from the previous image. This is typically performed with sub-resolution or sub-pixel movements. SRR can then be accomplished through three main steps: registration, interpolation, and reconstruction of the multiple images (see Figure 3.1). Briefly, in the first step of registration, the orientation and spatial location of each image is correlated with respect to the others. Next, interpolation infers the location of each image with respect to all other images on a singular high resolution grid. Finally, the reconstructed image is algorithmically determined based on the registration and interpolation of the series of images to create a statistically viable higher-resolution image typically through minimization of some criteria. Figure 3.2 illustrates the SRR concept in a cartoon



**Figure 3.1** Registration of the images provides the spatial orientation and location between each of the images based on one image as a reference. Interpolation transfers each registered image onto a higher-resolution grid in the correct orientation with respect to a reference image (Image 1). Finally, reconstruction uses a statistical algorithm to provide the statistically most viable image based on the inputs.

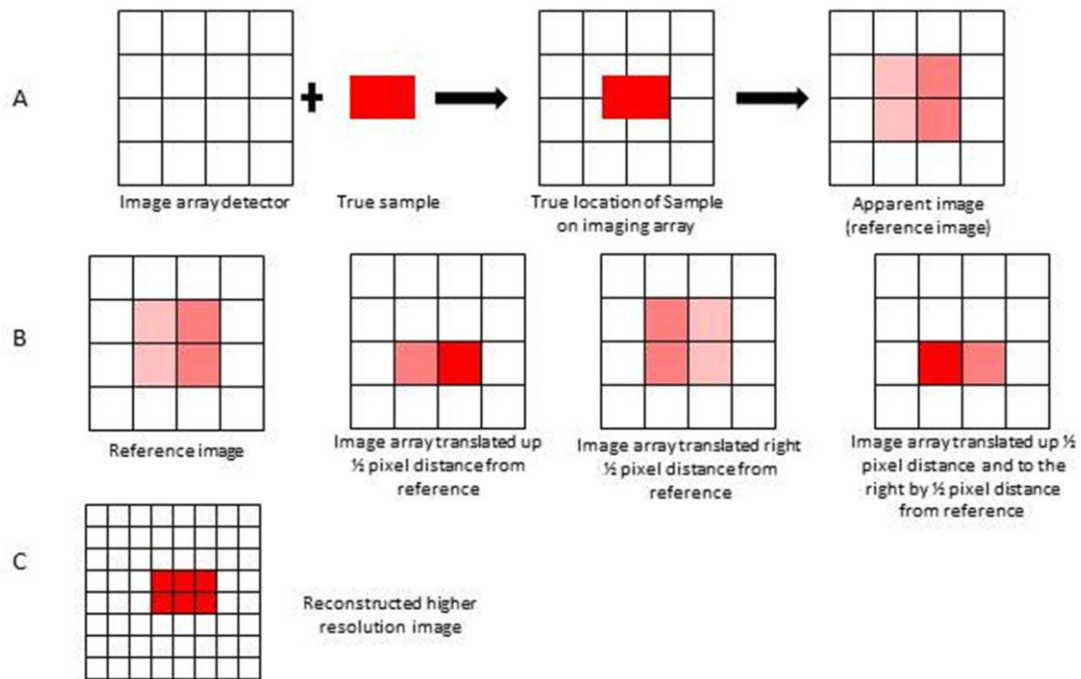
representation of an array of imaging detector pixels and an object that is to be “imaged” and will be discussed in detail in the following sections.

### 3.1.1 Image Registration

To employ SRR, first a series of multiple lower resolution images (LRI) are obtained that have been spatially offset from one another in sub-pixel increments (see Figure 3.2B). Sub-pixel or sub-resolution shifts are required for this process in order to elucidate the high frequency information lost when obtaining an image with optical components. Each of the translations or sub-pixel shifts in the example provided (Figure 3.2B) would be one-half pixel distance in the x-, y-, and x and y-directions with respect to the reference (Figure 3.2A). Having full pixel shifts will simply be obtaining the same light intensity

information, and each successive full-pixel shift will result in the same loss of high-frequency information without the ability to recover it.

The LRI are combined often using an algorithm to estimate the translation between each of the LRI, using one LR image as a reference.<sup>12-16</sup> Alternatively, the translations between each image, if known accurately, can be incorporated directly into the reconstruction analysis without an estimation of their locations. The known translations provide an accurate spatial orientation with respect to a reference image, which is typically the first image in the series obtained. Much of the progress in SRR recently has been efficient incorporation of a registration estimator within the reconstruction algorithm in an attempt to decrease the computational load in the reconstruction process.<sup>17</sup>



**Figure 3.2** (A) Using a 4x4 pixel array to image a red block results in a blurred and pixelated image. (B) A reference and several sub-pixel sifted images translated in the x-, the y-, and the -x and y- directions. (C) Resulting higher-resolution grid from the super-resolution process providing an image that better represents the red block.

### 3.1.2 Image Interpolation

After the images have been registered with respect to each other, they are placed on a high-resolution grid. The high-resolution grid is determined by the number of sub-pixel shifted images obtained by  $\sqrt{n}$ , where  $n$  is the number of images obtained. Therefore, the high-resolution array of pixels is effectively made larger (i.e. the individual pixels effectively made smaller with respect to the original image grid).

### 3.1.3 Image reconstruction

The increase in resolution through SRR is realized between Figure 3.2A and Figure 3.2C where the size of the object being imaged is most closely related to the size of the object prior to imaging and the contrast is consistent with where the object lies within the array.

To successfully accomplish the increase in resolution with respect to a reference image, algorithms based on either iterative, statistical, or iterative and statistical models are employed.<sup>16-18</sup> The most intuitive, robust, and flexible methods employed for reconstruction are in the spatial domain where each LRI is considered a blurred ( $B_k$ ), down sampled ( $D_k$ ), and translated ( $M_k$ ) image with additive noise ( $N$ ). Based on this concept, an analytical relationship between each of the LRI ( $Y_k$ ) and the HRI ( $X$ ) exists, where:<sup>19</sup>

$$Y_k = D_k B_k M_k X + N \quad (\text{Eq. 3.1})$$

$Y_k$  and  $X$  are vectors of intensity values in lexicographical order while  $D_k$ ,  $B_k$ ,  $M_k$ , and  $N$  are matrices of their respective values. Extending this relationship, for each LRI into a linear system of equations provides:

$$\begin{bmatrix} Y_1 \\ \vdots \\ Y_k \end{bmatrix} = \begin{bmatrix} D_1 B_1 M_1 \\ \vdots \\ D_k B_k M_k \end{bmatrix} X + N \quad (\text{Eq. 3.2})$$

In an ideal scenario (i.e. perfectly spaced translations, known blur, and perfectly decimated individual images), this system of linear equations can then be solved via a non-iterative interpolation-restoration manner in the spatial domain, in which  $B_k$  for each image is assumed to be linearly spatial invariant, and is the same for all observations and therefore becomes  $B$ . This is true when the same set of imaging optics are used for each LRI obtained, there are few or no aberrations in the images, and that the displacement (i.e. movement) of any object in the sample is slower than the image acquisition itself. This approach is further simplified when only translations are occurring between observations. Eq 3.1 then becomes:

$$\underline{Y_k} = D_k M_k \mathbf{H} + \underline{N} \quad (\text{Eq. 3.3})$$

Where  $\mathbf{H}$  is the product of  $X$  and  $B$ , and  $\underline{Y_k}$  and  $\underline{N}$  are concatenated vectors. In general, to solve Eq. 3.3, the LRI are registered with respect to one another, a nonuniform interpolation algorithm is used to obtain  $\mathbf{H}$ . Finally, through an iterative process whereby the differences between a reference or estimated higher-resolution image are minimized, and a deblurring and noise removal algorithm is used to obtain  $X$  back from  $\mathbf{H}$ .

While the above example provides the most straight-forward approach to solving the SRR problem, it is not without a computational cost. Furthermore, real-world applications will seldom have the perfect scenario providing a system of equations that can be solved without iterative methods. Therefore, in this chapter, the mathematical treatment for solving the analytical relationship while reaching the high-resolution image



used is a variation of alternating projection onto convex sets, or POCS.<sup>20-23</sup> Herein is a brief summary of how POCS is applied in this reconstruction analysis.

#### 3.1.4 The POCS Algorithm

In POCS, a high-resolution image (i.e. image reconstruction solution), which is considered a convex set,  $C$ , is made up of pixels from LRI that are themselves convex sets. An argument of POCS is that alternating POCS among  $N$  convex sets with non-empty intersection will converge to a point common to all convex sets, regardless of initial conditions, though initial conditions can change the convergence. Since pixels of lower-resolution images are sub-pixel shifted and all part of the original scene (i.e. ground truth image or non-pixelated analog information) the convex sets (low resolution images and ground truth) will intersect and all converge to produce a higher-resolution image.

In SRR, this variation of the POCS algorithm works by first registering the LRIs on a high-resolution grid, based on the translations ( $M_k$ ), creating a convex set  $C_1$ . Next, a second higher-resolution image is compiled in a mirror-image, also based on  $M_k$  as well as the blurring kernel ( $B$ ), creating a second convex set  $C_2$ . The norms of images (i.e. the square root of the sum of the absolute squares of each element within the matrix) are minimized with respect to iteratively comparing the two images with increasing amounts of de-blurring. Despite POCS being computationally taxing, this algorithm works in the spatial domain allowing for the inclusion of *a priori* information, such as unique image registration, and is not a complex modeling technique, making POCS an adaptable algorithm.<sup>24, 25</sup>

In this chapter, it is shown that an imaging bundle consisting of 30,000 individual fiber elements, when magnified to over-fill each pixel on the imaging detector, can be used for super-resolution reconstruction. Specifically, the diameter of a calibration standard was shown to approach the true value of the calibration standard upon dithering with the transmission of a single atomic line (546nm) and reconstruction when using the imaging bundles. These results pave the way for using the bundles in this geometry for the spectroscopic evaluation of materials from the microscale to the nanoscale.

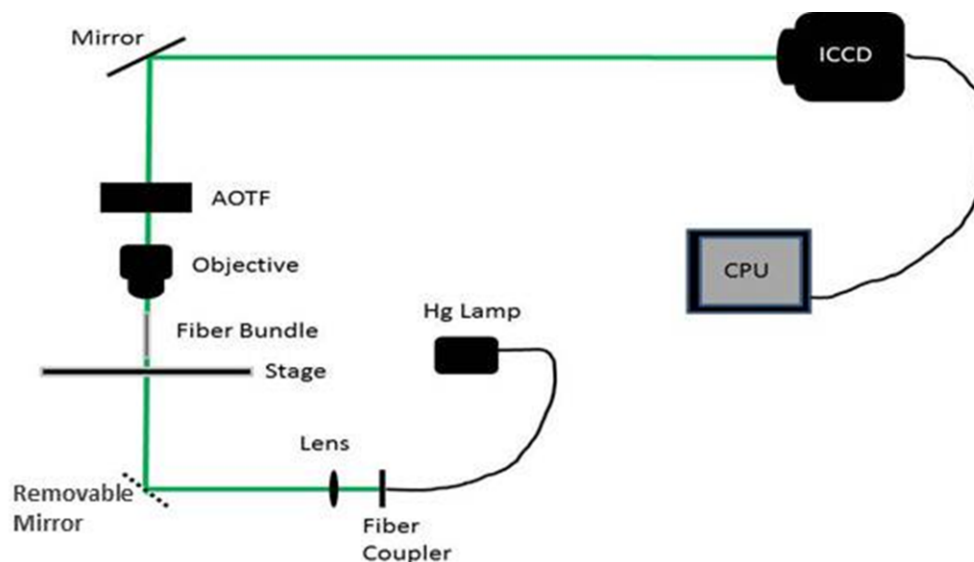
## **3.2 Materials and Methods**

### *3.2.1 Fiber bundle Preparation*

Fiber bundles consisting of 30,000 individual fiber elements were purchased from Sumitomo Electric Industries (IGN08/30) and cut to a length of 7.5 cm. Each bundle had the protective polymer silicone outer-layer mechanically removed with a glass-scoring tool on both ends and were polished to be optically flat via lapping paper with grits of 5 $\mu$ m, 3 $\mu$ m, 1 $\mu$ m and 0.5 $\mu$ m. The overall bundle is approximately 1mm in diameter (with silicone shield) and can be mounted into any sub-miniature #1 (SM1) style fiber optic mount via a custom made fiber adapter previously described.<sup>26</sup> The fiber bundle is coherent (i.e., each fiber is correlated from end-to-end) allowing for image transfer.

### *3.2.2 Imaging System*

A diagram of the instrumental set up used to obtain the lower resolution images is shown in Figure 3.3. Light emitted from an Hg-Ar source is collimated from a fiber optic by an F/2 lens into a 1cm diameter and reflects it off of a removable mirror. The collimated light then passes through the sample at the center of the aperture on a Nano-Drive 3



**Figure 3.3:** Schematic diagram of the instrumental set up used in these experiments. Descriptions of the various components are found within the text.

piezo-electric stage (PES; Mad City Labs) which allows for x-, y-, and z-axis translations with 0.4nm resolution over a range of 200 $\mu$ m. A microscope slide mount is attached to the face of the PES, allowing for the attachment of a standard microscope calibration target (bar size from 160 $\mu$ m - 20 $\mu$ m). The fiber bundle (described above) then collects the transmitted light from the calibration target. A microscope objective (Nikon, S Plan Fluor ELWD40xC WD 3.6-2.8mm) is used to collect the light transmitted through the fiber probe array and collimate it prior to being directed into an acousto-optic tunable filter (AOTF; Brimrose TEAF7-0.5-0.9-UH/H). The AOTF is used to select the desired wavelength of light to be imaged and the resulting image is detected through a Nikon DS, AF-S Nikkor camera lens attached to an intensified charged coupled device (ICCD; Princeton Instruments PIMax). A general description of how the AOTF works is found in

section 1.2.2 in Chapter 1 of this dissertation. Additionally, the characterization of the AOTF used in this document is found in Appendix C.

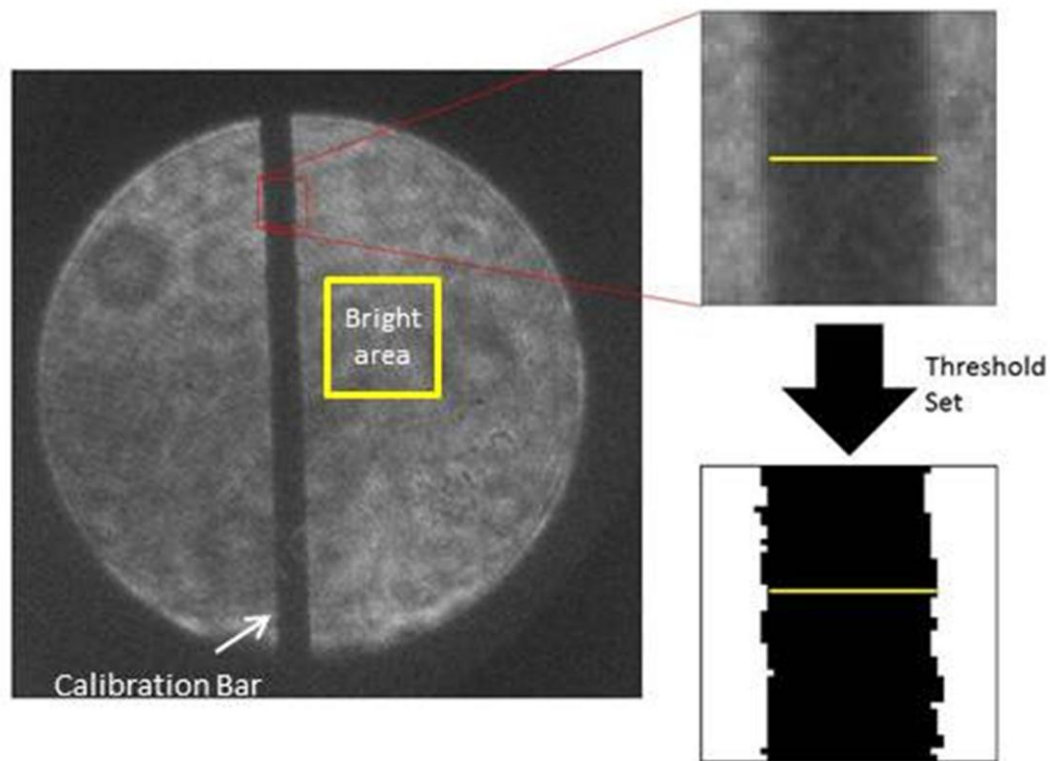
### *3.2.3 Data Processing*

Images were collected using Winspec/32 version 2.5.21.0. Additional image pre-processing was completed using ImageJ version 1.47 to convert the 16-bit images to 8-bit images (for computational reasons) for super-resolution reconstruction in MATLAB R2014a. Reconstruction was completed using a modified free-ware program available online<sup>12</sup> that is coded to employ the POCS reconstruction algorithm. See Appendix D for the modified algorithm in full. Translational motion from the PES, was estimated from the built-in, continuous monitoring interface provided by the manufacturer (Mad City Labs), and the specific point spread function associated with each fiber array probe employed, discussed in Sections 3.3.1 and 3.3.2 respectively, were incorporated into the reconstruction algorithm. Post-processing procedures for the analysis of the reconstructed images (e.g., cross sections, averaging, etc.) were performed using ImageJ.

## **3.3 Results and Discussion**

### *3.3.1 Translational Calibration*

Calibrating the translations of the PES to the pixel movements is essential for an adequate registration of the reference image and subsequent image reconstructions. Reconstruction algorithms require measurements in pixels (or fraction thereof) while the stage readout outputs in microns. In addition, the calibration takes into account the total magnification of the system by the objective imaging the fiber bundle and the magnifying compound lens on the ICCD. As such, a calibration target was used to identify the apparent pixel



**Figure 3.4** Captured image of 20 micron bar with 40X microscope objective. A sampled area of the 20 micron bar for a cross section of the total number of pixels and the applied threshold used to determine the number of pixels in the 20 micron bar.

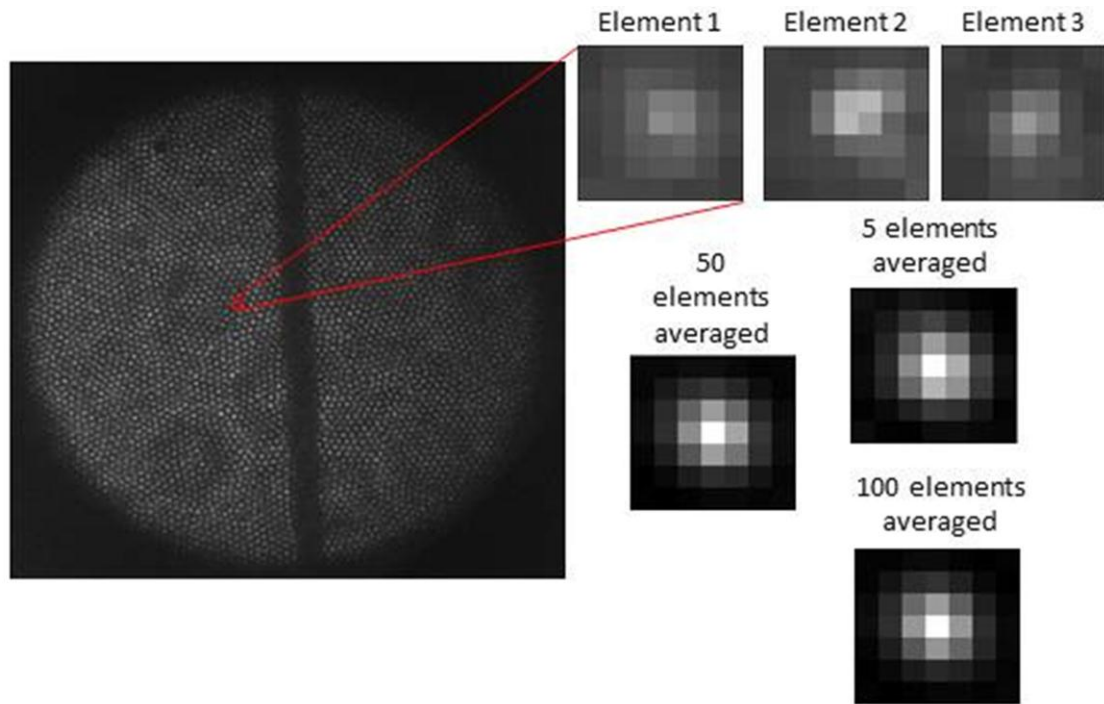
distance across an optical microscope resolution target as seen in Figure 3.4. The 20-micron bar was found to be  $27.1 \pm 0.4$  pixels across at the 95% confidence interval, based on 50 cross-sectional measurements taken at random on the target bar. This corresponds to an image-to-pixel ratio of  $0.7\mu\text{m}/\text{pixel}$ , and an image magnification of approximately 27 fold. The conversion from the distance movements of the PES to pixel movements as represented on the ICCD provides the necessary information for dithering each LRI by the desired amount.

To ensure no bias with the gray scale images in determining the cross sections, a threshold was set when using ImageJ by using the average and standard deviation of 5

sets of pixels from the areas around the calibration bar. To set the threshold value, images as shown in Figure 3.4 recorded the illuminated calibration target with an Hg-Ar pen lamp and was used to provide the “bright” areas around the calibration bar (high intensity, see Figure 3.4). An average intensity value of 2700 arbitrary units was calculated for the bright, unblocked region by averaging these five areas together. The threshold value of 2500 arb. units was therefore set allowing for greater than 99% certainty that the pixel intensity values that have less than the threshold value were associated with the 20-micron calibration bar on the calibration standard. Using this threshold value of 2500 arb. units the calibration bar was measured from one edge to the other edge 50 times at random to obtain the above value of  $27.1 \pm 0.4$  pixels, as shown in Figure 3.4. 50 cross-sections were chosen to ensure that any small variation within the target bar could be accounted for.

### *3.3.2 Point Spread Function*

The point spread function of the current system is no longer defined by an infinitesimally small point and how that point appears on the detector. It is, however, a convolution of the traditional optical components (i.e., lenses, detector, etc.) and the imaging bundle, and can be defined by the distribution of light from an individual fiber element of the probe onto the ICCD. This is due to the over-filling of each fiber element on the detector such that there are several pixels per fiber element. When an infinitesimally small point of light is present in the sample, it will propagate up the fiber element in contact with the sample at that location resulting in a PSF the size of the individual fiber element. The resulting transmission of light from the point source through the fiber element and onto the ICCD is then used to determine the point spread function of the system.



**Figure 3.5:** An image of the 20micron bar through the fiber bundle and three separate plots of the luminous output of the fiber element.. Below that are 5, 50, and 100 fiber element PSFs averaged together to highlight how quickly the averaged PSF appears to converge to a reproducible PSF.

A 7x7 block (49 pixels) was chosen as the area defining each fiber element and therefore the point spread function, as seen in Figure 3.5. Because one fiber element is not necessarily representative of what a PSF of the system would be, an average of 5 to 100 fiber element PSFs were obtained. As can be seen in Figure 3.5, the average PSF quickly converges to an “ideal” PSF for the system (i.e. two-dimensional Gaussian distribution). The averaging of the fiber elements also provides a threshold value for what is considered unobstructed light propagating through the fiber bundle which allows for a discriminative measure of the 20 micron bar through the fiber elements since this was done in transmission geometry as previously discussed.

The PSF is the low-pass filter that is used in the POCS reconstruction algorithm used in this paper whereby it is typically estimated. However, if the PSF (blur,  $B_k$ ) is known accurately, it can be incorporated into the algorithm. In the case of this paper, the PSF is the last factor not controlled by the user. The PSF is a 7x7 array, as described above in Figure 3.5 and is a normalized probability density of an average of 100 individual fiber elements with intensity values ranging from 0-1. Since the PSF is a result of the intensity distribution of light in each fiber element, the cladding is taken into account on the outside edges of the PSF.

### *3.3.3 Reconstruction*

16 images that were sub-fiber element shifted were obtained with known translational data in order to reconstruct them into a higher-resolution image. The reconstruction process and analysis were broken into two sections: section one utilized  $B_k$  as the standard blurring kernel while section two utilizes a PSF associated with an average of 100 fiber elements (i.e. a custom blurring kernel).

#### *3.3.3.1 Standard blurring kernel*

Using the standard blurring kernel (seen in Figure 3.6A) in this dithering technique and our well-characterized fiber bundles, an increase in resolution was achieved. A threshold value was again determined by examining the intensity values of the light transmitted through the fiber elements following illumination of the calibration standard with the Hg-Ar light source. Threshold was established again because the fiber-bundle was put in place and, because the bundle is hexagonally packed, some of the light will be blocked and must be accounted for. The AOTF was tuned to image the 546.04nm Hg atomic emission line and a series of images were obtained. The center pixel of the PSF of 10



A

0.25	0.5	0.25
0.5	1	0.5
0.25	0.5	0.25



B

0.370797	0.369308	0.383303	0.387641	0.372931	0.362046	0.368488
0.369907	0.408022	0.465043	0.484508	0.439408	0.383564	0.362278
0.387037	0.458712	0.619692	0.747538	0.592079	0.432811	0.373273
0.393242	0.476733	0.737654	1	0.74008	0.469179	0.383494
0.375246	0.432599	0.577898	0.732773	0.612178	0.45295	0.382714
0.362856	0.381692	0.424185	0.458873	0.441411	0.402416	0.372679
0.36887	0.359127	0.366751	0.377153	0.376091	0.369242	0.375784



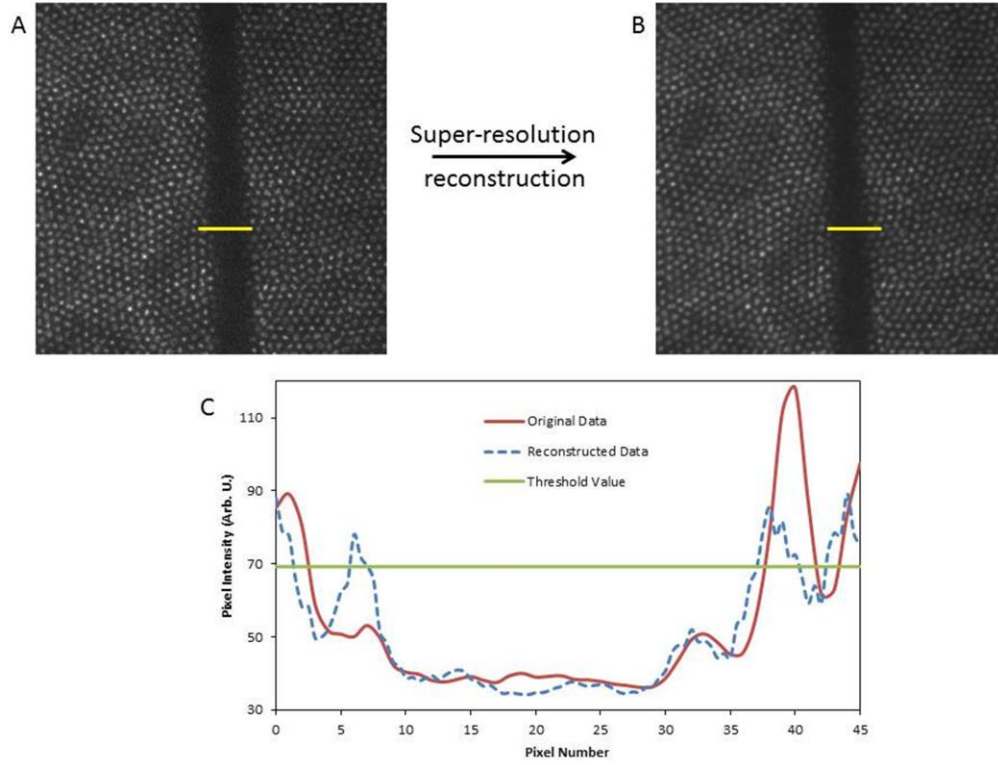
**Figure 3.6:** A representation of a standard blurring kernel used in a step-wise fashion through the entire matrix of an image (A) and a custom blurring kernel derived from the point spread function of the system being employed for use in a step-wise fashion through the entire matrix of an image (B). The blurring kernel is normalized intensity values with respect to the central, most intense value.

individual fiber elements not blocked by the calibration line on the non-dithered image were chosen as reference and the different signal intensity values for the center pixel ([4,4] in the 7x7 matrix of the PSF) were averaged and found to be 167 arb. units (in the 8 bit image). Three times the standard deviation provides us a discriminatory measure of over 99% certainty and can be used to find a minimum threshold for what is considered light propagating through each fiber element. As such, the minimum threshold value for unobstructed light propagating through the fiber element was found to be 69 arb. units.

To determine the spatial resolution of the final reconstructed image, cross-sectional intensity profiles across the 20 micron bar were examined, as depicted in Figure 3.7 as a representative example. The pixel intensity of the cross-sectional intensity profile was plotted as a function of pixel number, which can be converted back to absolute distance

via the initial calibration step. Since the fiber-elements over-filled the pixels and there is cladding around each fiber element, a pattern emerges in the cross-sectional intensity profiles, resulting in an “up and down” periodic events as seen in Figure 3.7. As such, the fiber element peak crossing the threshold at any point in either the reference image or the reconstructed image is indicative of the unobstructed light propagating through the fiber element. As shown, there is a significant and real increase in spatial resolution associated with the reconstructed image (dashed line), resulting in a measured bar width of  $22.6\mu\text{m}$ , while the LRI reference image corresponds to a bar width of  $26.6\mu\text{m}$ . As expected, both values are greater than the  $20\mu\text{m}$  calibration bar, with the reconstructed image providing a significantly more accurate size at several cross sections. The LRI provided a cross-section that was 11.4% larger than the true value of  $20\mu\text{m}$ , while the reconstructed image provided a cross-sectional value that was a relative increase in resolution of 15.3%.

The percent-differences were determined relative to the reference image for the relative increase in resolution. This highlights how much the reconstruction processes improves the image resolution with respect to a single LRI as a reference. This was determined by using this relationship:



**Figure 3.7:** (A) One of several low-resolution images for the (B) super-resolution reconstructed image using a projection over convex sets algorithm found in reference [12]. Cross section of data represented by line in A and B. Solid line is original data, dotted line is the reconstructed data and the horizontal solid line is the threshold.

$$\left( \frac{D_{ref} - D_{rec}}{D_{ref}} \right) \times 100 \quad (\text{Eq. 3.4})$$

Where  $D_{ref}$  is the distance (in microns) that the reference image is representing the target calibration bar,  $D_{rec}$  is the distance (in microns) that the reconstructed image is representing the target calibration bar. Alternatively, a comparison can be made between the reconstructed image and the known, true size of the calibration bar. This was determined through the following relationship:

$$\left( \frac{D_{rec} - D_{GT}}{D_{rec}} \right) \times 100 \quad (\text{Eq. 3.5})$$

Where  $D_{GT}$  is the distance (in microns) of the ground-truth calibration bar. Fifteen cross-sectional measurements chosen at random over the length of the calibration bar in the image were obtained. Using Eq. 3.4 and Eq. 3.5, and a threshold set from light passing through the fiber elements, it was found that over 90% of the cross-sectional measurements yielded an increase in resolution. The average relative increase in resolution (using Eq. 3.4,  $n = 15$ ) was found to be  $12\% \pm 5\%$  at the 95% confidence level. Alternatively, the reconstructed images appeared to be  $13\% \pm 7\%$  larger than the ground truth image at the 95% confidence interval. The reference images appeared to be  $23\% \pm 5\%$  larger than the ground truth image at the 95% confidence interval. Over 93% of the total cross-sectional profiles obtained resulted in a significant increase in relative resolution. Literature values report up to 65% relative increase in resolution using a line-spread function in a similar manner as used in this document.<sup>27</sup>

While the total increase seen here is over all less than what has been reported elsewhere,<sup>11, 27</sup> one of the major differences between the studies is the use of a fiber bundle over-filling pixels on the image detector. The areas where the cladding is present (as seen as the dark areas of Figure 3.5) represent an area where the underlying information is not known. Dithering with sub-fiber element shifts still provide high-frequency information but do not fill the high-resolution grid as well as an image without void spaces can. Two approaches can be used moving forward: 1) regularization parameters can be introduced into the POCS algorithm in order to help take into account the void space present by the cladding or 2) a lower magnification microscope objective can be used to avoid the need for regularization parameters. This will result in an overall decrease in the observed resolution of the bundle (the resolution will no longer be defined

by the fiber-elements of the fiber bundle), but can be matched such that it is very close. The second approach (lower objective magnification) is discussed in Chapter 4 of this thesis where the fiber bundles are used to obtain dithered chemical-specific information from a solid-substrate.

#### *3.3.3.2 Custom Blurring Kernel*

Obtaining the cross-sectional profile in the same way as section 3.3.3.1 and using the custom blurring kernel, as seen in Figure 6B, the reconstruction did not provide a statistically different result. The relative percent increase in resolution from the lower-resolution images to the higher-resolution reconstructed image was found to be  $2\% \pm 6\%$  at the 95% confidence interval ( $n = 15$ ) and appeared to be  $30\% \pm 8\%$  larger than the calibration target bar at the 95% confidence interval. Approximately 73% of the cross-sectional profiles obtained resulted in a relative percent increase in resolution of 1.2% - 4.7%. Approximately 27% of the cross-sectional profiles did not yield an increase in resolution. It should be noted, however, that the overall percentage of cross-sectional profiles resulting in an increase in relative resolution was smaller with the custom blurring kernel, suggesting that the size of the kernel does in fact influence the reconstruction. This is expected, considering as the size of the kernel increases, the chances of inter-element blurring increases (i.e. blurring is occurring in more than one element at a time in the step-wise implementation of the blurring kernel).

### **3.4 Conclusions**

The use of fiber-bundles in the post-processing of images when the fiber-elements are over filling the pixels on the image-detector array is a viable process for enhancing the resolution past the inherent resolution of the fiber-elements of the bundle. Using an

atomic emission line from an HgAr source, a calibration target bar of 20 $\mu$ m was illuminated. After obtaining 16 lower-resolution images at sub-pixel shifts in the 2-dimensional x- and y-plane, the reconstructed higher-resolution image using a standard blurring kernel and known translations yielded an overall relative percent increase in resolution (from a reference, lower resolution image) of  $12\% \pm 5\%$  at the 95% confidence level. Alternatively, using a custom blurring kernel that incorporated the point spread function of the fiber-elements within the fiber bundle did not yield a statistically difference relative increase in resolution and was found to be a  $2\% \pm 6\%$  at the 95% confidence interval. Overall, using a standard blurring kernel and an imaging bundle that has over-filled the imaging detector pixels does in fact show an average increase in resolution showing for the first time that these imaging bundles can be used with post-processing methods to increase the resolution of the image beyond that of the inherent resolution of the fiber-bundle elements. While using a custom blurring kernel (i.e. PSF for the system being used), care must be taken in utilizing one of appropriate size.

### 3.5. References

1. Hell SW. (2007) Far-Field Optical Nanoscopy. *Science* 316 (5828): 1153-1158.
2. Betzig E, Patterson GH, Sougrat R, Lindwasser OW, Olenych S, Bonifacino JS, Davidson MW, Lippincott-Schwartz J, Hess HF. (2006) Imaging Intracellular Fluorescent Proteins at Nanometer Resolution. *Science* 313 (5793): 1642-1645.
3. Weiss PS. (2014) Nobel Prizes for Super-Resolution Imaging. *ACS Nano* 8 (10): 9689-9690.

4. Willets KA. (2014) Super-resolution imaging of SERS hot spots. *Chemical Society Reviews* 43 (11): 3854-3864.
5. Schmid T, Opilik L, Blum C, Zenobi R. (2013) Nanoscale Chemical Imaging Using Tip-Enhanced Raman Spectroscopy: A Critical Review. *Angewandte Chemie International Edition* 52 (23): 5940-5954.
6. Fernandez-Suarez M, Ting AY. (2008) Fluorescent probes for super-resolution imaging in living cells. *Nat Rev Mol Cell Biol* 9 (12): 929-943.
7. Izeddin I, Specht CG, Lelek M, Darzacq X, Triller A, Zimmer C, Dahan M. (2011) Super-Resolution Dynamic Imaging of Dendritic Spines Using a Low-Affinity Photoconvertible Actin Probe. *PLoS ONE* 6 (1): e15611.
8. Hankus ME, Li H, Gibson GJ, Cullum BM. (2006) Surface-Enhanced Raman Scattering-Based Nanoprobe for High-Resolution, Non-Scanning Chemical Imaging. *Analytical Chemistry* 78 (21): 7535-7546.
9. Elad M, Feuer A. (1997) Restoration of a single superresolution image from several blurred, noisy, and undersampled measured images. *Image Processing, IEEE Transactions on* 6 (12): 1646-1658.
10. Farsiu S, Robinson M, Elad M, Milanfar P. (2004) Fast and robust multiframe super-resolution. *IEEE Transactions on Image Processing* 13 (10): 1327 - 1344.
11. Duponchel L, Milanfar P, Ruckebusch C, Huvenne J-P. (2008) Super-resolution and Raman chemical imaging: From multiple low resolution images to a high resolution image. *Analytica Chimica Acta* 607 (2): 168-175.

12. Vandewalle P, Susstrunk S, Vetterli M. (2006) A Frequency Domain Approach to Registration of Aliased Images with Application to Super-resolution. *EURASIP Journal on Advances in Signal Processing* 2006 (1): 071459.
13. Tsai R, Huang T. (1984) Multiframe image restoration and registration. *Advances in Computer Vision and Image Processing* 1: 317 - 339.
14. Zitova B, Flusser J. (2003) Image registration methods: a survey. *Image and Vision Computing* 21 (11): 977 - 1000.
15. Stone H, Orchard M, Ee-Chien C. (1999) Subpixel registration of images. *Proc. Signals, Systems, and Computers, 1999. Conference Record of the Thirty-Third Asilomar Conference on*, 2:1446-1452 vol.1442.
16. Park S, Park M, Kang M. (2003) Super-resolution image reconstruction: a technical overview. *IEEE Signal Processing Magazine* 20 (3): 21 - 36.
17. (2011) *Super-Resolution Imaging*. Boca Raton, FL: CRC Press,
18. Farsiu S, Robinson MD, Elad M, Milanfar P. (2004) Fast and robust multiframe super resolution. *Image Processing, IEEE Transactions on* 13 (10): 1327-1344.
19. Yang J, Huang T. (2011) Image Super-Resolution: Historical Overview and Future Challenges. In *Super-Resolution Imaging*, ed. P Milanfar. Boca Raton, FL: CRC Press, 1-33 pp.
20. Stark H, Oskoui P. (1989) High-resolution image recovery from image-plane arrays, using convex projections. *J. Opt. Soc. Am. A* 6 (11): 1715-1726.
21. Marks RJI. (1997) Alternating Projections onto Convex Sets. In *Deconvolution of Images and Spectra*, ed. PA Jansson: Academic Press, 476-501 pp.



22. Sezan MI. (1992) An overview of convex projections theory and its application to image recovery problems. *Ultramicroscopy* 40 (1): 55-67.
23. Youla D. (1978) Generalized Image Restoration by the Method of Alternating Orthogonal Projections. *IEEE Transactions on Circuits and Systems* 25 (9): 694-702.
24. Feng S, Dong F, Sun S, Zou Y, Zhou C. (2014) Performance analysis for two typical spatial domain super-resolution reconstruction algorithms. *Proc. 2014 7th International Congress on Image and Signal Processing*:353-358.
25. Malczewski K, Stasiński R. (2009) Super Resolution for Multimedia, Image, and Video Processing Applications. In *Recent Advances in Multimedia Signal Processing and Communications*, ed. M Grgic, K Delac, M Ghanbari. Berlin, Heidelberg: Springer Berlin Heidelberg, 171-208 pp.
26. Kiser JB, Cullum BM. (2009) Tunable fiber-optic imaging bundle SERS substrates, 7313:73130E-73130E-73138.
27. Offroy M, Moreau M, Sobanska S, Milanfar P, Duponchel L. (2015) Pushing back the limits of Raman imaging by coupling super-resolution and chemometrics for aerosols characterization. 5: 12303.

## **Chapter 4: Surface Enhanced Raman Based Dithering**

### **4.1 Introduction**

Increasing the resolution of an image with either optical or geometric techniques are becoming increasingly popular, providing a more intricate look into many disciplines from cell biology to satellite imagery.<sup>1, 2</sup> Super-resolution imaging (SRI), a relatively recent group of techniques that rely on optical equipment to increase spatial resolution of the resulting images, has been used extensively in microscopy/nanoscopy.<sup>3, 4</sup> These powerful techniques, including stimulated emission by depletion, tip-enhanced Raman imaging, and reversible saturable optical fluorescent transition often require advanced optics and are highly sensitive to the instrumentation being used to obtain the measurement. Often, these techniques are a scanning in nature, resulting in reduced temporal resolution. Although, they can be limited in temporal resolution, they can typically provide tens of nanometers to single nanometer spatial resolution.<sup>3, 5, 6</sup>

Many super-resolution techniques also employ geometric or, more generally, post-processing as a means to unveil the high frequency information lost in an image that is projected on a CCD due to optical aberrations or physical limitations in both the equipment and the wave-behavior of light. Included in this high frequency information are the details that provide the user with the information necessary to achieve sub-diffraction-limited spatial resolution. Major techniques that use post-processing include stochastic optical reconstruction microscopy (STORM), photo activated luminescence microscopy (PALM), and other optically modulated techniques.<sup>4, 7, 8</sup> In all of these techniques, series of images are obtained when the field of view is sparsely populated by the analyte of interest allowing single analytes to be isolated or the stochastic nature of

individual molecules to be utilized to isolate the resulting signals. Upon collection of large amounts of data, the individual molecules can be registered between the different images obtained, allowing for a reconstruction based on the individually illuminated point sources (analytes) present in each image. The reconstruction processes rely on the use of statistical estimations, allowing for the use the high frequency information by over sampling an area.<sup>9-11</sup>

Alternatively, techniques strictly reliant on post processing, not the inherent nature of an analyte of interest or the system used, are becoming increasingly useful. Super-resolution reconstruction (SRR) techniques, defined by the use of post-processing techniques, are used to extract the high-frequency information from a series of lower-resolution images.<sup>12-14</sup> These techniques are used in an array of disciplines including surveillance, medicine, remote sensing, biological imaging, and materials imaging, of which most rely on this technique for diagnosis, treatment and/or safety.<sup>3, 15-19</sup> In general, computer vision algorithms are employed as a means of statistically interpolating the image to provide the high-frequency information from multiple images (from less than five to greater than 1000).

Combining the power of super-resolution post processing techniques with a vibrational imaging technique such as Raman or more specifically surface enhanced Raman scattering (SERS) (to compensate for small analyte concentrations in the small measurement volumes) provides an inherent chemical fingerprint allowing for a sensitive and selective detection technique with high spatial resolutions. In fact, relative resolution increases of approximately 30% have been obtained using a confocal Raman instrument when combined with SRR techniques. An extension to this idea would be to employ a

non-scanning technique to improve the temporal resolution when imaging as well. Furthermore, Raman is an inherently weak phenomenon; utilizing plasmonics can enhance the signal obtained thereby increasing sensitivity and reducing imaging time. Additionally, using a wide-field imaging system provides the opportunity to increase temporal resolution as well as the ability to obtain multi- or hyperspectral images. As with all super-resolution techniques though, an increase of resolution comes at a cost of a decrease in temporal resolution. With the use of multi-frame, sub-pixel shifted images, the temporal capabilities of a system are limited to the time it takes to obtain a series of images.

This chapter provides the first case, to the best of our knowledge, of a dithered plasmonic array for achieving resolution improvements via SRR. Additionally, the signal-to-noise (S/N) relationship between reconstructions and spatial resolution enhancement is explored. Sixteen sub-pixel shifted images are used to reconstruct a higher-resolution SERS image using the imaging fiber bundles. Synthetic data were created and used to analyze the way S/N and the number of images obtained affects reconstructions. The S/N is an important factor to explore as the imaging fiber bundles have the ability to be tapered in such a manner that provides individual fiber optics with diameters of 30-50nm (resulting in a bundle diameter of approx. 17 $\mu$ m). At tapered diameters, there are a smaller number of physical molecules present in each sub-diffraction-limited area, resulting in a an overall lower S/N. Additionally, since the temporal resolution is dependent on the time it takes to obtain a series of images, the number of images used in a reconstruction and how it affects the relative increase in resolution is explored.

## 4.2 Materials and Methods

### 4.2.1 Fiber Bundle Preparation

Imaging fiber bundles consisting of 30,000 individual fiber elements were purchased from Sumitomo Electric Industries (IGN08/30). The bundles are 980 $\mu\text{m}$  in diameter with each element measuring 4 $\mu\text{m}$  in diameter. The lapping film (Thor Labs) used for polishing consisting of decreasing grits of 5 $\mu\text{m}$ , 3 $\mu\text{m}$ , 1 $\mu\text{m}$ , and 0.3 $\mu\text{m}$ . After each lapping film was used, the partially polished bundle was rinsed with water and visually inspected for any scratches or chips.

Following polishing, the bundles were etched in a 25% (v/v%) aqueous HF solution. The tips of the bundles were carefully placed in the etchant at a constant depth for 30 seconds. Etching was then quenched by submerging the tip of the bundle into deionized water (DI H<sub>2</sub>O), with sonication and/or manual agitation for at least 120 seconds.

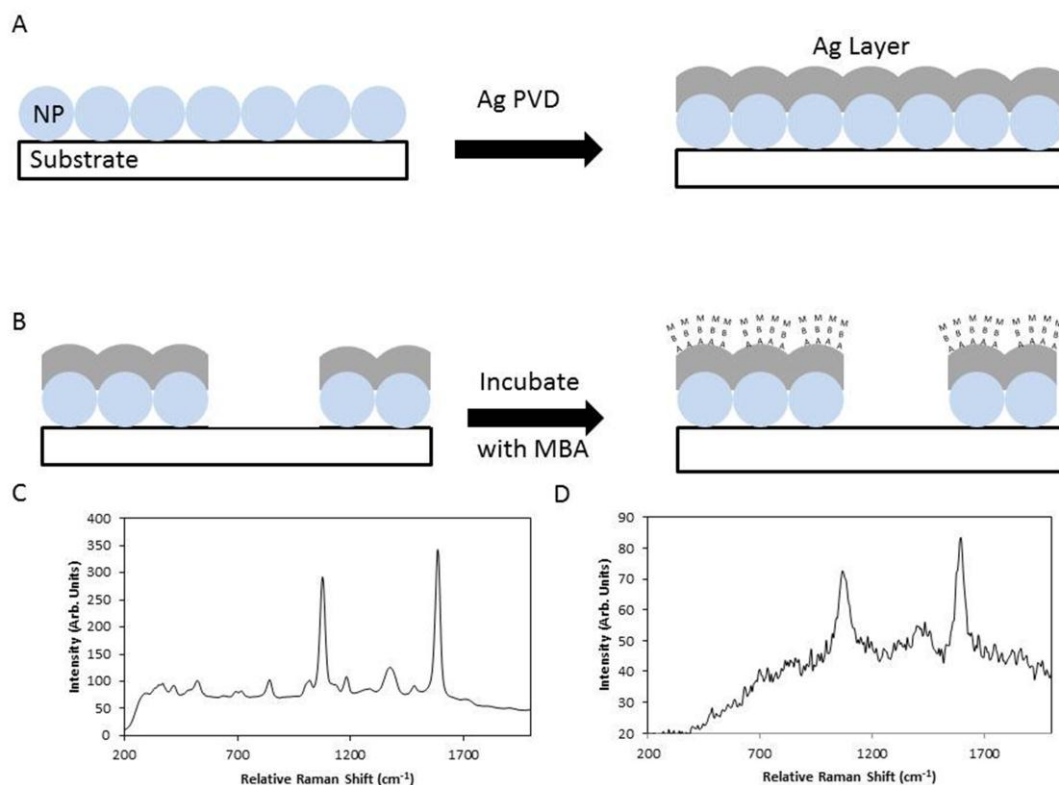
Each polished and etched bundle was then prepared for metal deposition using a Denton Vacuum Explorer physical deposition system. Each bundle was secured to a rotating motor and then mounted into the physical deposition system. Appendix B explains at more length the process by which the system works. Bundles were coated with 20nm of Ag (99.99% pure, Kurt J. Lesker Company)), according to the quartz crystal microbalance mounted inside the instrument. The motor rotated under high vacuum at  $<5 \times 10^{-6}$  torr at about 10,000 rotations per minute (RPM) and metal was deposited on the fibers at approximately 0.5 $\text{\AA}/\text{s}$ . The bundles were then removed from the physical vapor deposition instrument and placed under vacuum until ready for use.

### 4.2.2 Substrate Preparation

Substrates were prepared for imaging, as described below. A schematic representation of the preparation is also found in Figure 4.1. The substrates have mercaptobenzoic acid (MBA) bound to the exposed Ag for chemical specific boundaries on the substrate.

#### 4.2.2.1 Slide Preparation

Slides were prepared for use via cleaning and acidification of the silica surface. Standard



**Figure 4.1:** Schematic representation of the substrate preparation for analysis with imaging fiber bundles and super resolution reconstruction. A) First a thin metallic film is deposited over nanospheres. B) Metal-coated substrates where then scratched and incubated with MBA to provide complete coverage of the metallic area, while leaving the area with no metal free from MBA. C) Spectrum of substrate with MBA bound acquired with the spectrometer described in Chapter 2. D) Spectrum of substrate measured through the imaging system used in this chapter with a 980μm bundle and a 10-second exposure.

microscope slides were cut to approximately 1cm wide and washed with DI H<sub>2</sub>O. The slides were then soaked for one hour in a solution of NH<sub>4</sub>OH, H<sub>2</sub>O<sub>2</sub> and H<sub>2</sub>O in a 1:1:5 ratio (the trade name for this solution is RCA-1). The slides were then rinsed with DI H<sub>2</sub>O and soaked in 1M HCl for at least 1 hour. Slides were then washed with copious amounts of DI H<sub>2</sub>O (at least 6 times), rinsed with ethanol and then placed in a 60 °C oven to dry until use.

#### *4.2.2.2 Microsphere Preparation*

0.39 $\mu$ m silica microspheres (MicroSil™ Microspheres, 10% solids, Bangs Laboratory, Inc #SS02N) were washed and prepared for use to ensure homogenous dispersion. A 250 $\mu$ L aliquot of the stock solution was added with 750 $\mu$ L of DI H<sub>2</sub>O in a micro centrifuge tube and centrifuged for at least five minutes or until a pellet formed. The supernatant was then decanted and replaced with one milliliter DI H<sub>2</sub>O. This mixture was sonicated for 20 minutes and then vortexed for 60 seconds. Centrifugation, re-suspension, sonication, and vortexing was repeated three times for a total of four washes in DI H<sub>2</sub>O and then repeated two times using ethanol in place of the DI H<sub>2</sub>O. After the final centrifugation, the supernatant was decanted, re-suspended in 2mL of ethanol and sonicated for 20 minutes. Prior to use, the microsphere mixture was re-sonicated for 20 minutes and vortexed for 60 seconds. 10 $\mu$ L of prepared microspheres were drop-coated on the prepared slides and then dried in 60 °C oven overnight.

#### *4.2.2.3 Physical Vapor Deposition*

The prepared substrates received a thin film of silver metal for SERS capabilities, shown as a cartoon representation in Figure 4.1A. The slides were suspended in a holder above a tungsten evaporating boat and rotated between 10-15 RPM. Once the slides were under

high vacuum ( $2 \times 10^{-6}$  torr), they were coated with approximately 200nm of Ag (99.99% pure, Kurt J. Lesker Company), according to the quartz crystal microbalance mounted inside the instrument, depositing at a rate of ca. 1.0 Å/s. The slides were kept under vacuum until ready for use.

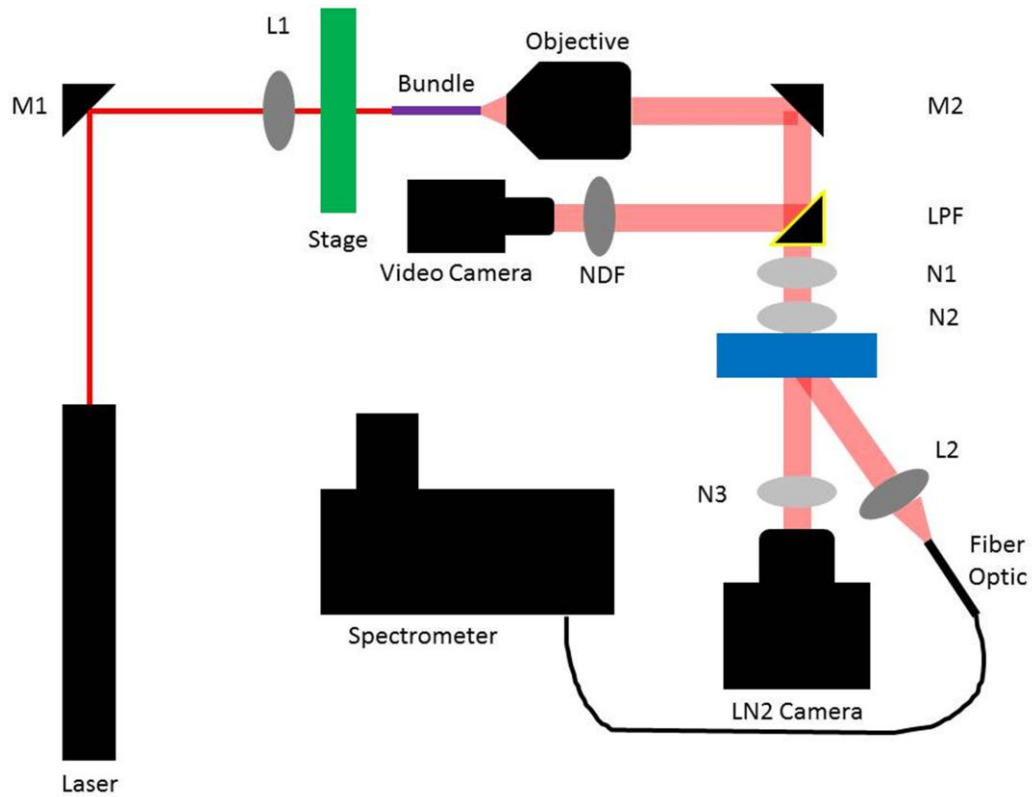
#### *4.2.2.4 Pattern Formation and Analyte Incubation*

A pattern was formed on the surface of the Ag coated substrates using a cleaned razor blade. A design similar to the letter “A” was scratched into the surface, removing the microspheres from the region resulting in void-space, pictorially shown in Figure 4.1B. The slides were then incubated with four 2µL aliquots of 2mM MBA and allowed to air-dry. The unbound MBA was washed away with five 10 mL aliquots of DI H<sub>2</sub>O, and three 6 mL aliquots of 200-proof ethanol sequentially.

#### *4.2.3 Instrumental Arrangement*



A diagram of the instrumental arrangement is seen in Figure 4.2. All optics and instrumentation were secured to a vibration-isolation table for dampening and isolation from unwanted vibrations. A 20mW HeNe laser (ThorLabs, HNL225R) is used for sample interrogation. The collimated laser light is passed through an f/4 lens, focusing through a central opening in the Nano-Drive 3 piezo-electric stage (PES, Mad City Labs) which allows for x-, y- and z-axis translation with 0.4nm resolution, in 5 nm increments over a range of 200 $\mu$ m. The focal point is situated at the face of the fiber bundle, where the bundle collects the scatter from the substrate/bundle interface, and then the



**Figure 4.2:** Schematic diagram of the optical system used for analysis. L1 and L2 are lenses for focusing the laser light. M1 and M2 are mirrors for directing the light. LPF is a long pass filter used to direct the shorter wavelengths (i.e. laser wavelength) towards a camera for real-time alignment and allow the Raman scattering to pass through. N1, N2, and N3 are notch filters for the HeNe being used.

transmitted light is collected by a 10 X microscope objective (Nikon Plan 10 X/0.25). A long-pass filter (640nm) is used direct the laser light towards a video camera (JVC TKC72OU color video camera) with a neutral density filter in front of a camera lens (Nikon, AF Nikkor) and used for monitoring the placement of the bundle in real time. The collimated scattered light then passes through two Holographic Notch-Plus filters (Kaiser Optical Systems, Inc. HNPF-632.8-1.0) prior to entering an acousto-optic tunable filter (AOTF; Brimrose TEAF7-0.5-0.9-UH/H) for wavelength modulation. The AOTF's characteristics are discussed in detail in Appendix C.

The modulated output of the AOTF (i.e. selected wavelength, 1<sup>st</sup> order diffraction) passes through a third notch filter and then was incident on a liquid nitrogen (LN2) cooled detector (model 7509-0002, Princeton Instruments, SPEC-10 System with an ST-133A controller) with a mounted camera lens (Nikon DS, AF-S Nikkor) for chemical-specific imaging. The non-modulated output of the AOTF (0-order diffraction) was directed towards an f/2 lens, coupled to a fiber optic. The fiber optic is coupled with a spectrometer (Princeton Instruments; SpectraPro 2300i with a PIMAX 2 ICCD model #7483-0015) for simultaneous monitoring the spectral output of the bundle while obtaining chemical specific images.

#### *4.2.5 Data Processing*

All images were collected using Winspec/32 with an acquisition rate of 600 seconds, and an analog to digital conversion rate of 100KHz. Additional pre-processing of the images was completed using ImageJ (version 1.47) to crop and convert the 16-bit images to 8-bit images for computational considerations while using a super-resolution reconstruction algorithm in MATLAB R2014a. Post-processing of the reference image and

reconstructed images were processed in both MATLAB R2014a and in ImageJ whereby MATLAB was used primarily for the programmatic extraction and fitting of cross-sectional information ( $n \geq 15$ ) from the images. ImageJ was primarily used for the visualization of the cross-sectional information and adjusting image contrast, threshold, etc. for visual acuity.

Translational stage movements were programmatically captured. In short, stage locations were obtained for the x-, y-, and z-axis in real-time at the beginning of an image acquisition and logged with LabVIEW 2010 (version 10.0). MATLAB R2014a was used thereafter to programmatically extract the average information from each file. Each position was then registered with respect to the first image in the series of images obtained.

Reconstructions were produced using a free-ware program available online<sup>20</sup> utilizing the projection over convex sets (POCS) algorithm. In short, reconstructions were completed using 4-16 images all registered with respect to the first image in the series. Depending on the number of used for the reconstruction, the interpolation factor (i.e. the increase in number of pixels) could be adjusted accordingly, at a maximum of  $\sqrt{n}$ ,  $n$  being the number of images obtained.

Each group of synthetic images were reconstructed into a higher-resolution image using a POCS algorithm. The registered down sampled and shifted images were selected in such a way to maximize the input from the lower-resolution image. After reconstruction, the images were analyzed at a step-edge to define the resolution of the reconstructed images, as described further in the Results and Discussion section.

## 4.3 Results and Discussion

### 4.3.1 Translational Calibration

Translational calibrations are required to relate stage movements, measured in distance units ( $\mu\text{m}$ ) to pixel movements needed in the reconstruction algorithms. Many super-resolution reconstruction techniques use a built-in estimation algorithm for realizing the sub-pixel movements since one of the drives for research in these algorithms are increased computation efficiency without *a priori* knowledge.<sup>13, 21-23</sup> However, in a controlled environment (i.e. vibration-controlled laboratory), the sub-pixel movements are provided by a nano-positioning stage and calibrating the translations of the PES is essential to registering the reference images with respect to one-another. Furthermore, as objectives or magnifying optics are changed or modified, the calibration must be updated for adequate reconstruction.

A process similar to what was described in Chapter 3 of this document was performed for the calibration. An optical microscope calibration target was used to identify the pixels per micron in the magnified system. A  $160\mu\text{m}$  calibration line was used, and identified at greater than the 99% confidence interval through a threshold of 130.8 arb. units, representing light being blocked by the calibration target. This threshold was identified by analyzing an area within the calibration bar (light being blocked) and an area outside of the calibration bar (light passing freely past) whereby the average and standard deviation of hundreds of pixels was used. A total pixel-distance relationship of  $2.1 \pm 0.2 \mu\text{m}/\text{pixel}$  was identified based on six individual cross-sections of the calibration bar.

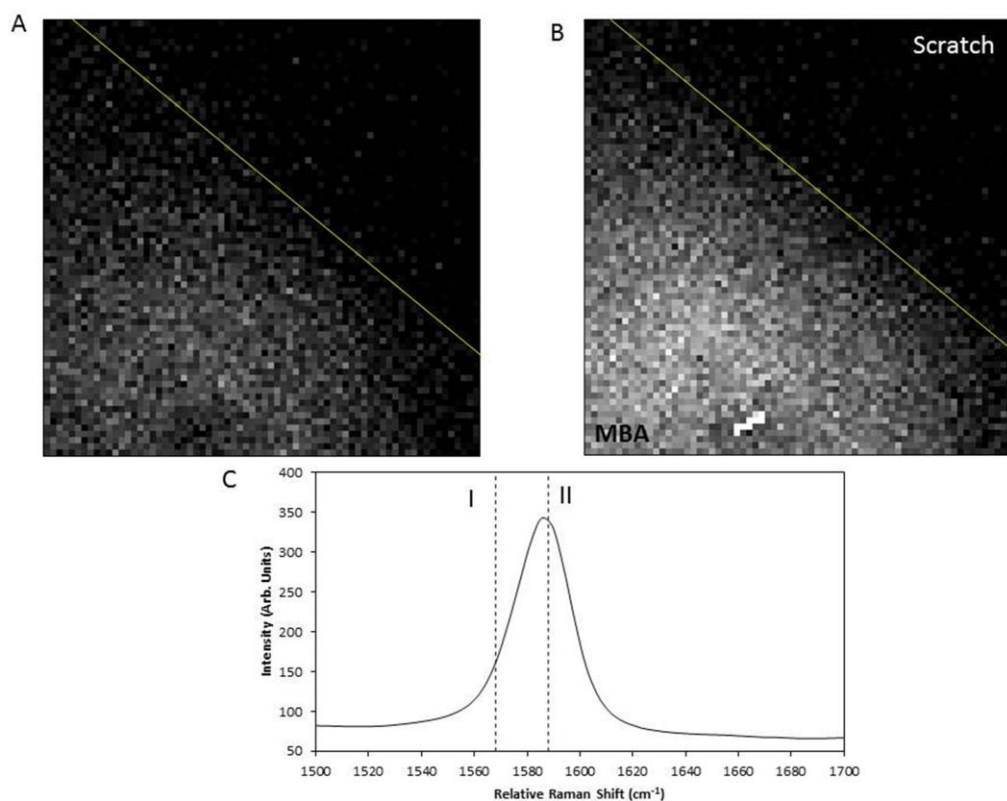
#### *4.3.2 Substrate Analysis*

The prepared substrates had four-2 $\mu$ L aliquots (for a total of 8 $\mu$ L) of 2mM MBA drop-coated on them sequentially to extend the time that MBA was solvated and interacting with the metallic surface to ensure binding prior to evaporating. As the ethanol was seen to evaporate away, a new drop was placed; this process lasted several minutes total. After the ethanol completely evaporated, the substrates were washed with DI H<sub>2</sub>O and ethanol in succession to clean and wash away any non-bound MBA that was on the surface or in the void space. Furthermore, the substrates were inspected with an optical microscope and spectrally to ensure the pattern was formed appropriately and to confirm that the MBA was bound to the Ag metal. As seen in Figure 4.1D, the two main peaks of MBA (aromatic ring breathing; 1075cm<sup>-1</sup> and 1588cm<sup>-1</sup>) are clearly visible.

#### *4.3.3 Reconstruction Analysis*

Since spheres were physically scraped away from the surface of the substrate to create an edge, the theoretical limit of what the edge distance can be established. The spheres are hexagonally packed on the surface, being held in place by electro-static interactions. Furthermore, since the spheres were coated in silver, only photons originating from the MBA on the surface of the silver will provide signal. When the sphere is scraped away, as seen in Figure 4.1, one-half of the diameter of the sphere will be the drop-off of the edge. In this study, the spheres used had a diameter of 390nm, resulting in an edge drop-off of approximately 195nm.

Prior to analysis, the bundle was brought close to the substrate and chemical-specific images were obtained to ensure that the bundle is situated above the scratch providing the sharp edge desired for dithering analysis. In Figure 4.3B the demarcation is the step edge



**Figure 4.3:** A) Image of MBA substrate off the main peak (I in C). B) Image of the MBA substrate on the main peak (II in C). C) Peak used in analysis with I at the off-peak location and II at the on-peak location.

from metal film over nanoparticles to a bare area via manual removal of the nanoparticles, as described in Section 4.2.2.4 and Figure 4.1. MBA was physically bound to the Ag and subsequently washed away from the rest of the non-metal coated surface. Therefore, it is expected that areas with MBA bound will result in an area in the image that has a higher intensity with interrogating with a laser for SERS. As described in Figure 4.1, the two main SERS peaks of MBA are at  $1075\text{cm}^{-1}$  and  $1588\text{cm}^{-1}$ . As seen in Figure 4.3A, an image when the AOTF is tuned to  $1568\text{cm}^{-1}$ , which is not directly on the peak of the  $1588\text{cm}^{-1}$  shown in Figure 4.3C I, is compared to an image when the AOTF is tuned to the center peak of  $1588\text{cm}^{-1}$  (Figure 4.3B) and is shown to be more illuminated.

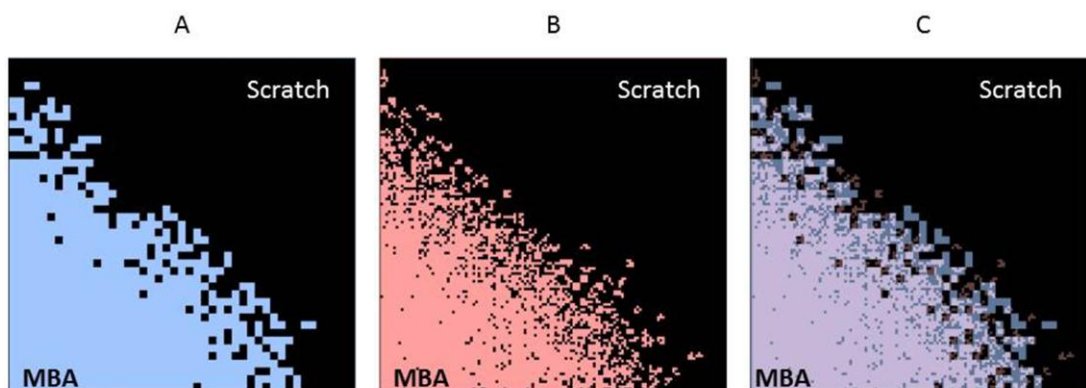
Each image is contrasted with the same intensity values as to make them directly comparable with one-another. As expected, when the AOTF is tuned to the center of  $1588\text{cm}^{-1}$  (Figure 4.3CII), the image intensity is greater (Figure 4.3B) than when tuned to  $1568\text{cm}^{-1}$  (Figure 4.3A). This therefore validates the presence of MBA, as observed with SERS spectrally, in the imaging area where dithering occurred.

Once it was confirmed that the bundle was placed over an edge and MBA was present, 16 images were obtained with sub-pixel movement shifts, as determined by the calibration of the translational stage; Table 4.1 tabulates the stage movements and their corresponding pixel movements. After the images were obtained, the images were loaded and registered into a program utilizing the projection onto convex sets (POCS) algorithm (see Appendix D) for super-resolution reconstruction. As seen in Figure 4.4, the reference image (Figure 4.4A) and the reconstructed image (Figure 4.4B) are shown together for a direct visual comparison. Figure 4.4B has four times as many pixels for the same imaging area as Figure 4.4A. Figure 4.4B does visually appear to have a higher resolution than that of the reference image, especially when they images are overlaid with each other as in Figure 4.4C. In the overlay, many of the single-pixels transitions (i.e. high intensity areas with only one or few pixels illuminated) in the low resolution image are reinforced closely along the step edge by the high resolution image, while areas further from the step edge tend to show less reinforcement. However, visual appearance can be highly subjective ultimately requiring a quantitative and objective analysis.

To provide a more objective evaluation, a line profile taken across this edge interface was extracted from the initial and reconstructed images, as shown in Figure 4.5A, whereby the yellow line shows one such diagonal crossing from the high intensity to low intensity

**Table 4.1:** Translational movements of the piezo electric stage for dithering, highlighting both axis in distance measurements and in pixel measurements.

Image Number	Distance ( $\mu\text{m}$ )		Pixels	
	x-axis	y-axis	x-axis	y-axis
1	0	0	0	0
2	0.752	0	0.362	0
3	0	0.369	0	0.178
4	0.752	0.747	0.362	0.359
5	0.377	0.368	0.181	0.177
6	1.125	0.369	0.541	0.178
7	0.377	1.17	0.181	0.563
8	1.125	1.121	0.541	0.539
9	0	0.747	0	0.359
10	0.752	0.37	0.362	0.178
11	0	1.121	0	0.539
12	0.752	1.121	0.362	0.539
13	0.377	0	0.181	0
14	1.125	0	0.541	0
15	0.377	0.746	0.181	0.359
16	1.124	0.746	0.541	0.359

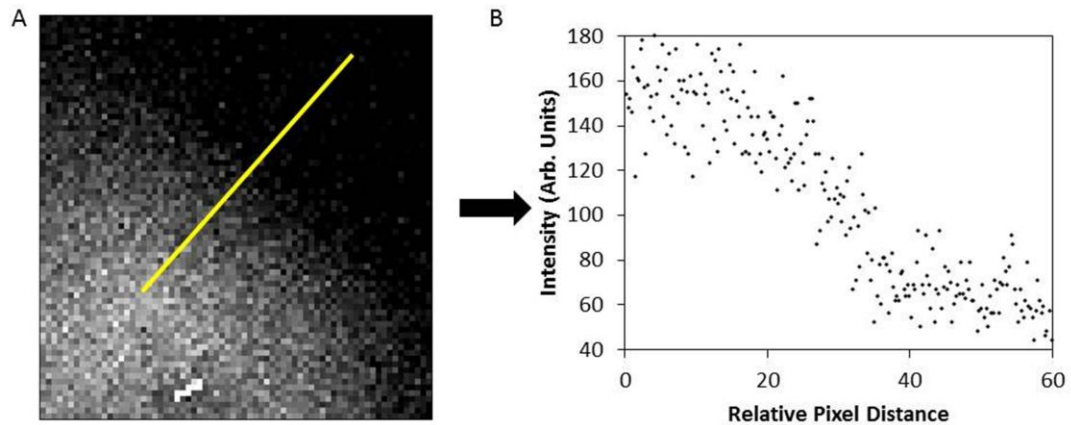


**Figure 4.4:** A) lower resolution contrasted based on threshold for direct comparison of B) reconstructed higher-resolution image. C) An overlay of the two images to show where they coincide and where there is more information afforded through reconstruction.



portion of the image. To ensure comparative measures between the low resolution images and the high resolutions images, each cross-section was initially located on the low resolution image. To obtain the coinciding cross-section on the high resolution image, the low resolution image can be multiplied by the factor that was given at the start of this. This was completed by creating a square region of interest across the edge to be evaluated resulting in a matrix of intensity units. In this case, the anti-diagonal of the matrix (i.e. lower left to upper right) was then used for the analysis. As the reconstructed images scale in size with the interpolation factor, using a region of interest allows for a scaling of the analysis area of both the reference and the reconstructed images in a systematic way. The anti-diagonal cross-sectional data information from the matrix can then be analyzed in an objective manner. To extract the appropriate information, a line spread function (LSF) is used to determine comparable parameters.

The LSF, which takes on sigmoidal characteristics, uses the full-width of the half-maximum (FWHM) from the first derivative of the cross-sectional profile across a step-

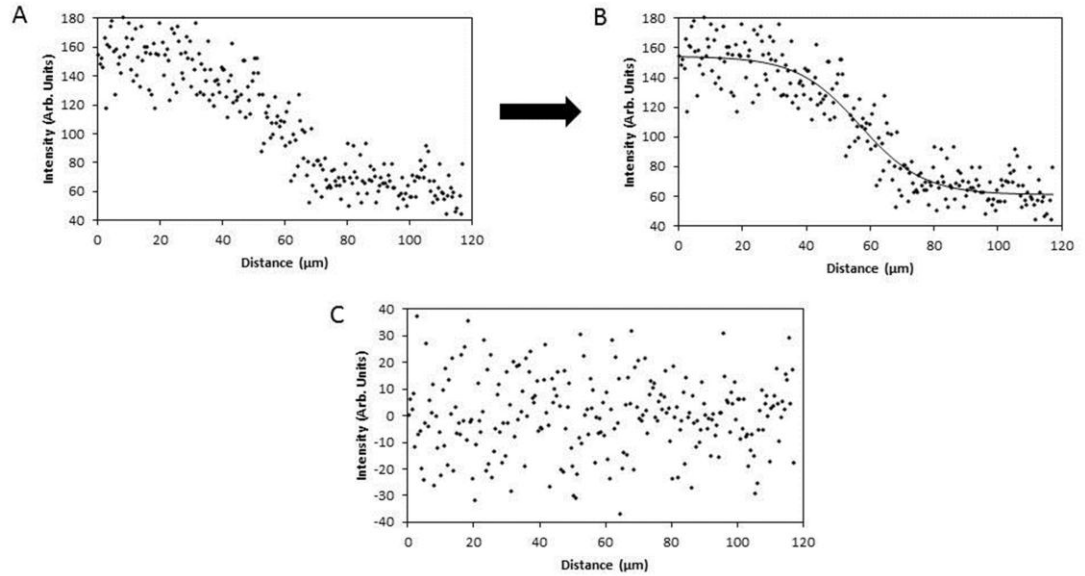


**Figure 4.5:** A) Higher resolution reconstructed image with a cross sectional line profile (yellow line) across the step-edge to create a line-spread function. B) The representative data from the cross-section.

edge to obtain comparable measures (see Figure 4.6 and Figure 4.7).<sup>14, 24</sup> The data provided by the step-edge line profile (i.e. cross-section) in the different images have noise (See Figure 4.5A) providing a first derivative that is fit with a sigmoidal function. The first derivative of the sigmoidal fit is then obtained, resulting in a distribution that can be fit to a Gaussian, Equation 4.1, as seen in Figure 4.7:

$$f(x) = Ae^{-\frac{(x-b)^2}{2c^2}} \quad (\text{Eq. 4.1})$$

Where  $A$  describes the amplitude or scaling factor of the distribution,  $b$  describes the offset (i.e. center x-value) of the distribution and  $c$  describes the width of the distribution. Using the  $c$ -fit parameters and minimizing the least squares residuals of the Gaussian fit to the first derivative of the sigmoidal function, the FWHM for each image's edge width can be defined, as illustrated below in scheme 1.<sup>25</sup> The full width as described at the half-



**Figure 4.6:** A) The noisy, raw data from the cross-sectional line profile fit to a sigmoidal function (B) to represent a non-noisy form of the data. D) A residual's plot to confirm that the sigmoidal function is in fact fitting the data well.

maximum is when  $f(x) = 0.5$  or  $f(x) = 2^{-1}$  and the scaling factor can be ignored because it is a constant factor that appears in both sides of the equation when solving and as a result, cancels each other out. Therefore:

$$2^{-1} = e^{-\frac{(x-b)^2}{2c^2}}$$

$$-\ln(2) = \frac{-(x-b)^2}{2c^2}$$

$$-2c^2 \ln(2) = -(x-b)^2$$

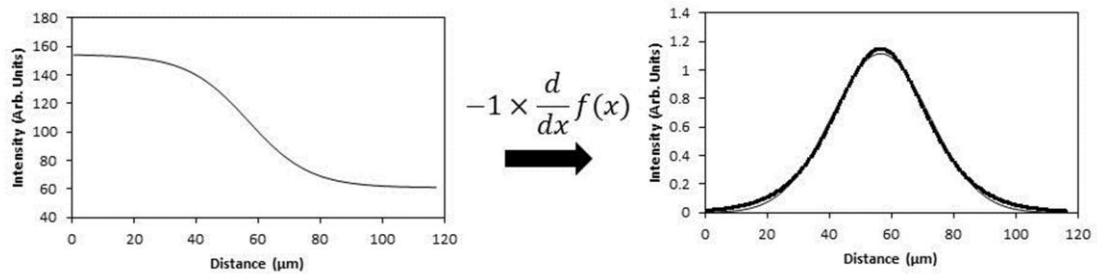
$$\pm c\sqrt{2 \ln(2)} = x - b$$

$$b \pm c\sqrt{2 \ln(2)} = x$$

And because  $x$  is at the half-maximum point and  $b$  defines the center value:

$$b_+ - b_- = c\sqrt{2 \ln(2)}$$

When comparing two LSFs, a plot of the FWHM can be used as comparative measures as seen in Figure 4.8. Figure 4.8A shows the Gaussian distributions from a line profile at the

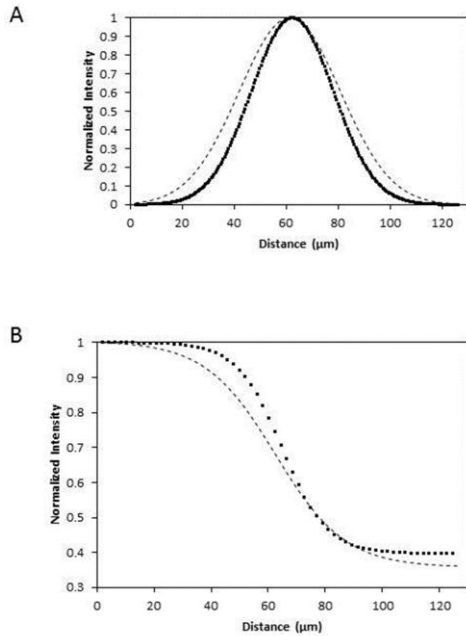


**Figure 4.7:** The sigmoidal function has its first derivative taken to provide a distribution that can be fit to Gaussian function whereby the full-width half-max can be extracted to provide a objective measure of comparison.

same spatial locations where the dashed line (- - -) is from the reference image, while the dotted line (•••) is from the reconstructed image, clearly showing a decreased width at the center. The plots were normalized to make them more directly comparable. Alternatively, a plot of the intensity cross-sectional profile for the original raw data that were fit to a sigmoidal function (Figure 4.8B, dashed line; - - -) and the reconstructed image (Figure 4.8B, dotted line; •••) reveals a sharper edge for the higher resolution reconstructed image. Thereby demonstrative that either method can be used for validation and quantification of image resolution improvement. The cross-sectional (i.e. line profile) analysis of the substrate at several different location ( $n = 4$ ) across the step-edge provides a relative increase in resolution of 20%. While there is quite a bit of variability, we see that the cross-section, analyzed as described yield an overall increase in the resolution compared to that of the reference image.

#### 4.3.4 Signal-to-noise Limitations to Image Reconstruction

To validate the reconstruction method and evaluate the effect of low signal-to-noise ratios

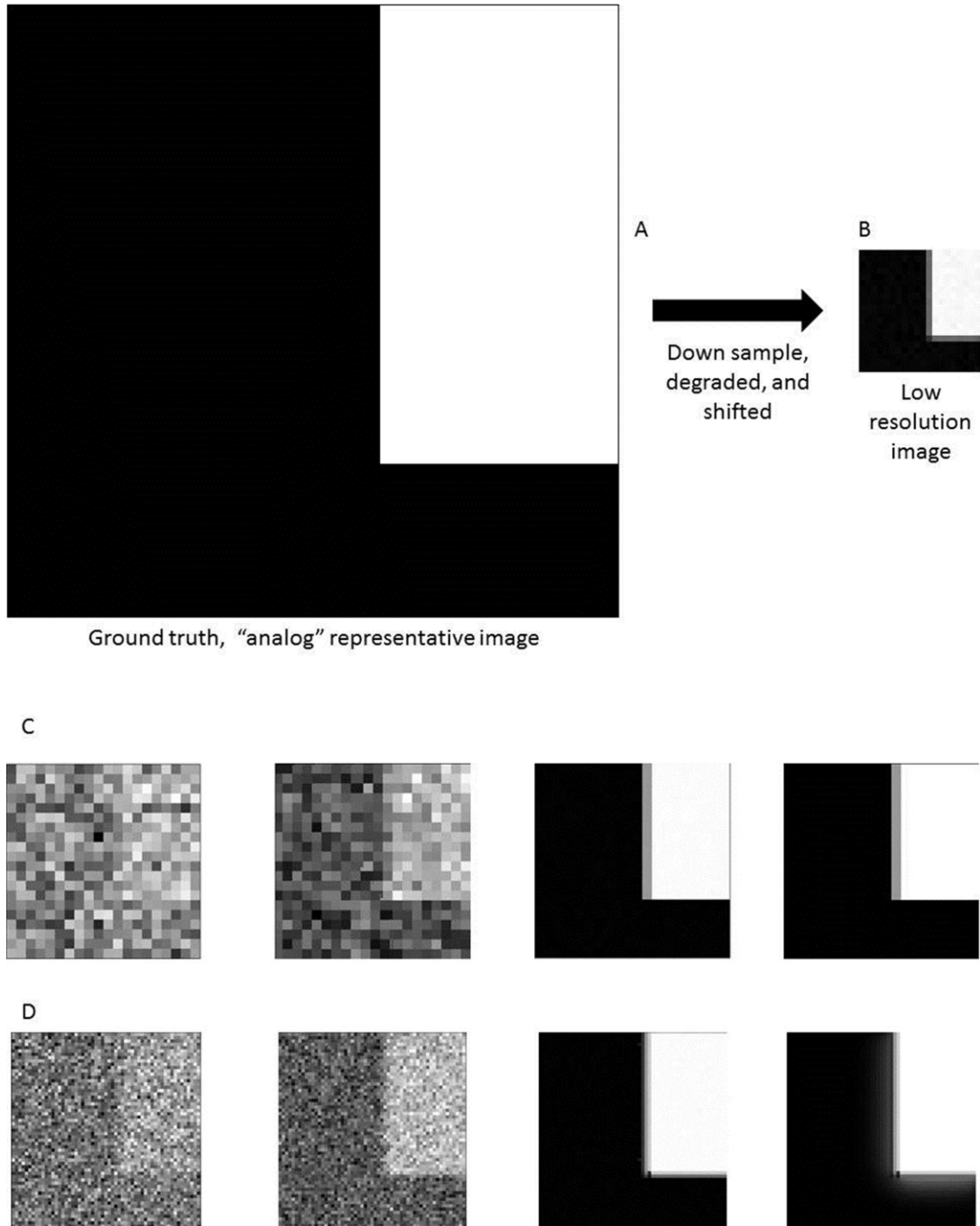


**Figure 4.8:** Exemplifying increase in resolution by virtue of the decrease in the full-width half-max (FWHM) of the Gaussian distribution (A, top) and by examining the slope of the lines in the fit Logistic function (B, bottom) whereby the square points represent the higher-resolution data and the dashed line is the lower-resolution data.

on the resolution improvement capabilities of this technique, synthetic data were employed to create a higher resolution reconstructed image. First, synthetic data were produced using MATLAB R2014b based on a higher resolution binary image, considered the ground truth image, and is approximated as a non-pixelated, analog object; see Figure 4.9A. The ground truth image was then down sampled into 25 individual images that have been sub-pixel shifted in increments of 0.2 pixels in the x- and y-planes. White Gaussian noise was added to each of the 25 down sampled and shifted images in various amounts to simulate signal-to-noise ratios (S/N) ranging from  $S/N = 1$  to  $S/N = 1000$ . One such downgraded, degraded, and shifted image is shown in Figure 4.9B, with a S/N of 40.

To relate the decimation ratio to reconstruction and evaluate the affect S/N has on it, the synthetic data were grouped by number of images used in the reconstruction. The groupings used were 4, 9, 16, and 25 images for a factor increase of 2, 3, 4, and 5 respectively. Each analysis was completed at every S/N and factor for each group.. Because increasing the factor is equivalent to an increase in pixels, each group was analyzed with respect to any factor less than the maximum achievable factor (i.e., 25 images were analyzed at a factor of 5, 4, 3, 2, and 1 while 16 images were analyzed at factors of 4, 3, 2, and 1). This resulted in 98 reconstructions. Once the images were produced, they were analyzed in the same way as described in Section 4.3.3.

Reconstruction successfully took place, regardless of the S/N of the original, lower resolution images. However, when the number of images used in the reconstruction and S/N remained low (e.g., four images,  $S/N = 1$ ), the reconstruction did not yield an image with visual acuity. An example of this can be seen in Figure 4.9C, the left most image

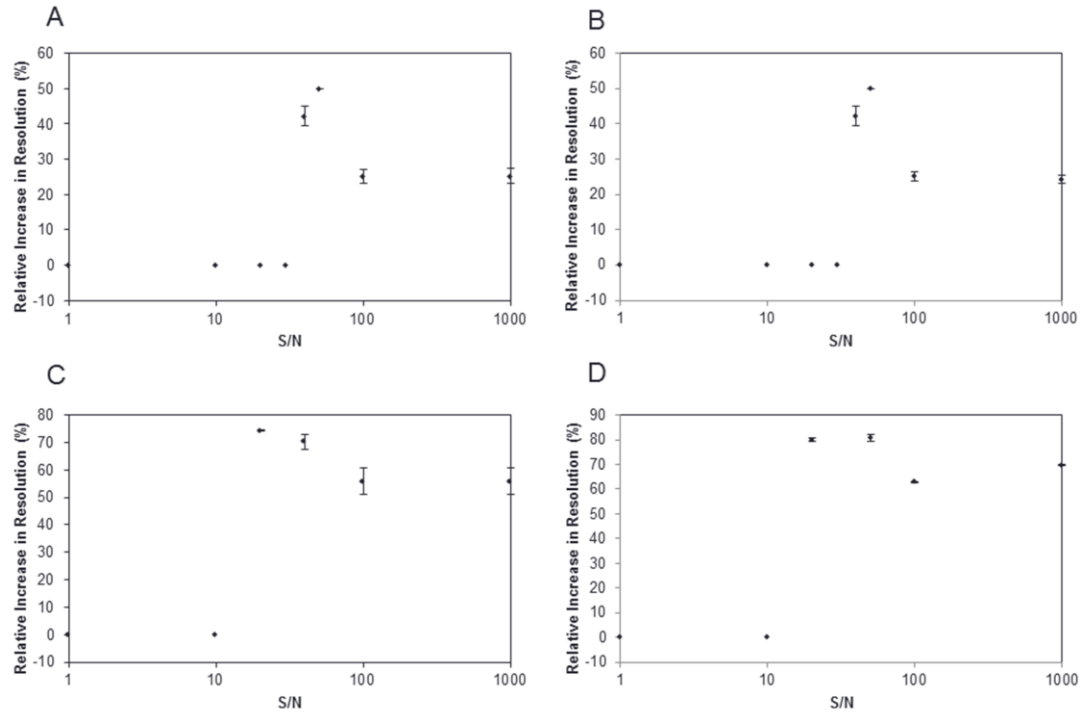


**Figure 4.9:** A) The ground truth image (100 x 100 pixels) and B) a representative image of the down sampled, degraded, and shifted images (20 x 20 pixels) with a total S/N of 40. C) lower-resolution images used in reconstructions with a total 25 images, arranged such that the S/N increases from left to right with  $S/N = 1, 10, 50, 1000$ . D) Corresponding high resolution reconstructed images from the row directly above it.

shows a down sampled and shifted image with a S/N of 1. The left most image in Figure 4.9D is a higher-resolution reconstruction of 25 down sampled, shifted, and noisy images, one of which is above it in Figure 4.9C. The lack of visual acuity is more likely due to the lack of detail in the down sampled and shifted images. In fact, the object can be faintly distinguished in the reconstructed image but undoubtedly cannot be *objectively* evaluated due to the amount of noise present. This is a testament to the subjective nature of image appearance and why an objective technique, such as a line-spread function, must be used to compare and contrast data.

Generally, as the number of images used increased (i.e. higher factor) in the reconstruction, the relative increase in resolution also grew. Specifically, 25 images with  $S/N = 50$  resulted in the highest relative increase in resolution with an increase of 80%. This was measured with the same method as in section 4.3.2. Briefly, a cross-section of the edge of an object was obtained, fit with a sigmoidal function and the first derivative of the sigmoidal function was obtained. The resulting data were then fit with a Gaussian function whereby the FWHM of the Gaussian was used as the objective comparative measure with the referenced down sampled image. Furthermore, images with  $S/N < 40$  did not consistently provide adequate fitting of the sigmoidal function. This was due to the magnitude of the noise with respect to the background resulting in cross-sections that generally did not correlate with the object present.

As seen in Figure 4.10 though, the maximum relative percent increase in resolution appears to occur with a S/N value of 40 – 50. This is due to the blurring kernel having more of an effect on images with  $S/N > 50$  due to the limited noise in the reconstruction process. At higher S/N the image appears binary with very little to no noise actually



**Figure 4.10:** Plots of relative percent increase in resolution as a function of S/N. A) Reconstructed with 4 images; B) reconstructed with 9 images; C) reconstructed with 16 images; and D) reconstructed with 25 images.

present. This results in an increase in the blurring of the edge when the blurring kernel is used in the estimation of the high-resolution image. In the images with  $S/N < 50$ , there is enough noise in the binary areas (i.e. areas where the background should be 0 or the area where the object should be 255) that the blurring kernel effectively blends with the noise already present. While this is shown for the synthetic data, this anomaly would not be expected in any imaging experiment because there is inherent shot noise in the analog-to-digital conversion resulting in some variability. Additionally, as expected, reconstructions completed with fewer images yielded relative percent increases in resolution that were overall less than those completed with more images. As seen in Figure 4.10A (corresponding to four images in a reconstruction), the maximum relative percent



increase in resolution is about 50%, while in Figure 4.10D (corresponding to 25 images in a reconstruction), the maximum relative percent increase in resolution is approximately 80%. This therefore validates that the use of additional images in the reconstruction processes has the potential to provide higher relative percent increases in resolution.

To draw a comparison between the synthetic data and the SERS data obtained, the comparison must be between images with a similar S/N. The SERS data obtained provided comparable S/N to synthetic data at a S/N of 20. Major differences between the synthetic data and the SERS data obtained is the spread of the noise that is present. In the SERS data, the spread of the noise (i.e. standard deviation across a small region of interest) does not fluctuate greatly while the S/N in the synthetic data does fluctuate quite a bit providing hot-pixels that tax the fitting procedures. Therefore, this verifies that the low S/N data obtained with SERS can be reconstructed and analyzed properly. Furthermore, it would be expected that SERS data with a higher S/N would make the reconstruction process result in a higher reconstructed resolution. However, it is also expected that decreasing the S/N will not provide data a good fit for the reconstruction, and will provide reconstructions with less detail. Therefore, moving to the nanoscale with the tapered imaging fiber bundles using the current equipment is not advisable because the overall signal will decrease as the aperture of the fiber optics decrease.

#### **4.4 Conclusions**

This chapter shows that wide-field, non-scanning imaging fiber bundles can be used for super-resolution reconstruction SERS imaging. Improvements in relative resolution increases of up to 20% provide an additional means of resolving power other than tapering the individual fiber bundles. Additionally, this chapter shows that S/N does have

an influence on the reconstructed image. It was shown increasing the S/N and increasing the number of images used in a reconstruction generally produced a reconstruction with a higher relative percent increase in resolution. Generally, S/N values up to 50 produce a reconstructed image with a high relative percent increase in spatial resolution. Tapering bundles to the nanoscale will result in images with lower S/N and therefore will utilize the full potential of image reconstruction analysis. Therefore, prior to going to the nanoscale with this reconstruction process, the S/N should be optimized. .

#### 4.5. References

1. Qifang X, Guoqing Y, Pin L. (2017) Super-resolution Reconstruction of Satellite Video Images Based on Interpolation Method. *Procedia Computer Science* 107 (Supplement C): 454-459.
2. Sydor AM, Czymmek KJ, Puchner EM, Mennella V. (2015) Super-Resolution Microscopy: From Single Molecules to Supramolecular Assemblies. *Trends in Cell Biology* 25 (12): 730-748.
3. Hell SW. (2009) Microscopy and its focal switch. *Nat Meth* 6 (1): 24-32.
4. Betzig E, Patterson GH, Sougrat R, Lindwasser OW, Olenych S, Bonifacino JS, Davidson MW, Lippincott-Schwartz J, Hess HF. (2006) Imaging Intracellular Fluorescent Proteins at Nanometer Resolution. *Science* 313 (5793): 1642-1645.
5. Sonntag MD, Pozzi EA, Jiang N, Hersam MC, Van Duyne RP. (2014) Recent Advances in Tip-Enhanced Raman Spectroscopy. *The Journal of Physical Chemistry Letters* 5 (18): 3125-3130.

6. Honigmann A, Mueller V, Hell SW, Eggeling C. (2013) STED microscopy detects and quantifies liquid phase separation in lipid membranes using a new far-red emitting fluorescent phosphoglycerolipid analogue. *Faraday Discussions* 161 (0): 77-89.
7. Rust MJ, Bates M, Zhuang X. (2006) Sub-diffraction-limit imaging by stochastic optical reconstruction microscopy (STORM). *Nat Meth* 3 (10): 793-796.
8. Hess ST, Girirajan TPK, Mason MD. (2006) Ultra-High Resolution Imaging by Fluorescence Photoactivation Localization Microscopy. *Biophysical journal* 91 (11): 4258-4272.
9. Rees EJ, Erdelyi M, Kaminski Schierle G, S. , Knight A, Kaminski C, F. . (2013) Elements of image processing in localization microscopy. *Journal of Optics* 15 (9): 094012.
10. Ovesný M, Křížek P, Borkovec J, Švindrych Z, Hagen GM. (2014) ThunderSTORM: a comprehensive ImageJ plug-in for PALM and STORM data analysis and super-resolution imaging. *Bioinformatics* 30 (16): 2389-2390.
11. Small A, Stahlheber S. (2014) Fluorophore localization algorithms for super-resolution microscopy. *Nat Meth* 11 (3): 267-279.
12. Farsiu S, Robinson M, Elad M, Milanfar P. (2004) Fast and robust multiframe super-resolution. *IEEE Transactions on Image Processing* 13 (10): 1327 - 1344.
13. Farsiu S, Robinson D, Elad M, Milanfar P. (2004) Advances and challenges in super-resolution. *International Journal of Imaging Systems and Technology* 14 (2): 47-57.

14. Duponchel L, Milanfar P, Ruckebusch C, Huvenne J-P. (2008) Super-resolution and Raman chemical imaging: From multiple low resolution images to a high resolution image. *Analytica Chimica Acta* 607 (2): 168-175.
15. Yang J, Huang T. (2010) Image Super-Resolution: Historical Overview and Future Challenges. In *Super-Resolution Imaging*, ed. P Milanfar: CRC Press, 1-33 pp.
16. Morin R, Basarab A, Ploquin M, Kouamé D. (2012) Post-processing multiple-frame super-resolution in ultrasound imaging. *Proc. SPIE Medical Imaging, San Diego, California*, 8320:83201G. SPIE
17. Offroy M, Roggo Y, Duponchel L. (2012) Increasing the spatial resolution of near infrared chemical images (NIR-CI): The super-resolution paradigm applied to pharmaceutical products. *Chemometrics and Intelligent Laboratory Systems* 117: 183-188.
18. Offroy M, Roggo Y, Milanfar P, Duponchel L. (2010) Infrared chemical imaging: Spatial resolution evaluation and super-resolution concept. *Analytica Chimica Acta* 674 (2): 220-226.
19. Guggenheim EJ, Khan A, Pike J, Chang L, Lynch I, Rappoport JZ. (2016) Comparison of Confocal and Super-Resolution Reflectance Imaging of Metal Oxide Nanoparticles. *PLoS ONE* 11 (10): e0159980.
20. Farsiu S, Robinson M, Milanfar P. (2004) MDSP resolution enhancement software.

21. Elad M, Hel-Or Y. (2001) A fast super-resolution reconstruction algorithm for pure translational motion and common space-invariant blur. *Image Processing, IEEE Transactions on* 10 (8): 1187-1193.
22. Farsiu S, Robinson MD, Elad M, Milanfar P. (2004) Fast and robust multiframe super resolution. *Image Processing, IEEE Transactions on* 13 (10): 1327-1344.
23. Park S, Park M, Kang M. (2003) Super-resolution image reconstruction: a technical overview. *IEEE Signal Processing Magazine* 20 (3): 21 - 36.
24. Smith SW. (1997) *The scientist and engineer's guide to digital signal processing*. San Diego, California: California Technical Pub.,
25. Weisstein EW. Gaussian Function.  
<http://mathworld.wolfram.com/GaussianFunction.html>

## Chapter 5: Concluding Remarks

### 5 Conclusion

This thesis describes the use of imaging fiber bundles for super-resolution reconstruction using surface enhanced Raman scattering (SERS) showing improvement in resolution with arrayed bundles for the first time. The effect that signal-to-noise (S/N) has on super-resolution reconstruction was evaluated by using synthetic data and was shown to influence reconstruction, but largely in a predictable manner. Additionally, the imaging fiber bundles are characterized, showing a negligible amount of cross-talk independent of imaging aperture size.

Cross-talk is defined as the amount of light leaking from a central fiber element in the imaging fiber bundle to the surrounding fiber elements. Untapered imaging fiber bundles with fiber elements of 4 $\mu\text{m}$  in diameter and fiber bundles with individual elements of 32nm in diameter were found to possess statistically the same amount of cross-talk, which was contrary to what was expected. The cross-talk across all sizes is found to be approximately 2% or less at the 95% confidence level. The protocol developed in this chapter for analyzing cross-talk is ubiquitous among any fiber optic or arrayed platform where the aperture is greater than 5nm. Additionally, a cleaning procedure is set forth to clean and strip the bundles of their metal coating and any quantum dot material providing a way to characterize cross-talk and re-use a single bundle.

The use of imaging fiber bundles in the post-processing of lower-resolution images when the fiber-elements are over filling the pixels on the image-detector array is a viable process for enhancing the resolution past the inherent resolution of the fiber-elements of

the bundle. When over-filling the pixels on the detector with each fiber element (i.e. a fiber element appears to consist of greater than 9 pixels on the detector array) a point spread function, dependent on the over filling of the detector, can be established. The reconstruction process was evaluated with a generic blurring kernel against that of a custom point spread function as the blurring kernel. Sixteen lower-resolution images were obtained with sub-pixel shifts of a 20 $\mu$ m calibration bar illuminated with a HgAr lamp and then reconstructed using the generic and custom blurring kernels. The generic blurring kernel resulted in a relative percent increase in resolution (from a reference, lower resolution image) of 12% at the 95% confidence interval. Using the custom blurring kernel (i.e. known point spread function due to over filling the detector array) resulted in a relative percent increase in resolution of only 2% at the 95% confidence level. While the custom point spread function did not provide the improvement in resolution as expected, it was determined the size of the blurring kernel plays a crucial role in resolution enhancements and despite know the point spread function and therefore blurring kernel exactly, using it with the imaging fiber bundle array is not beneficial when the face of the bundle is magnified such that the elements over fill the pixels.

In addition to showing resolution improvements with transmission imaging as previously stated, surface enhanced Raman scatter (SERS) was also employed to show for the first time using an imaging fiber array with a plasmonic substrate for dithering. 25 lower-resolution images were obtained from a step edge with mercaptobenzoic acid covalently bound to silver-coated nanospheres. Relative resolution improvements of approximately 20% are seen when using 25 images in the reconstruction process.

To aid in the understanding of how S/N affects the SERS measurements obtained, a theoretical study was completed using synthetic data with differing S/N values for each image. S/N values used were 1, 10, 20, 30, 40, 50, 100, and 1000 along with reconstruction using 4, 9, 16, and 25 images. It is shown that resolution improvements of up to 80% are seen when using 25 images in a reconstruction and a S/N of 50. It was expected that as the S/N increased the improvement in resolution would as well, however, due to the binary nature of the synthetic image used in this study, as the S/N approaches higher values (100 and 1000) the image approaches a binary form again and the blurring kernel then defines the resolution. In lower S/N images, the blurring kernel effectively blends the noise and does not extend out the step edge as it does at higher S/N values. Fortunately, no real imaging system produces binary images as there is also at least shot noise in each measurement.

Overall, the use of imaging fiber bundles in super-resolution reconstruction has been realized for improving the resolution beyond the inherent resolution of the imaging fiber bundle itself. Additionally, if temporal resolution can be sacrificed, additional lower-resolution images can be obtained to further increase the resolution. In future works, the fiber bundles can still be used and optimized for many experiments, especially relating to biology. To this end, moving towards an automated system for image acquisition when dithering would be advisable. This will decrease the time between measurements and increase the overall temporal resolution of the measurement. Additionally, when geometrically reconstructing an image, the introduction of priors in the algorithm can add robustness into both higher magnified bundles (i.e. over-filled elements on the detector array) and lower magnified bundles.



## Appendix A: Sutter P-2000 Instrument and Tapering

This appendix provides an example of a custom program used for tapering fiber bundles on the Sutter P-2000 micropipette puller and outlines the adjustable parameters and their functions for tapering such bundles. The micropipette puller has been modified (through the manufacturer) to accept fiber optics less than 1mm in diameter, which includes the imaging fiber bundles used in this dissertation. The customizable programs can have up to 8 lines of parameters, looping until either the fiber pulls apart or the laser is on for about 50 seconds (resulting in the program timing out).

In general, the micropipette puller tapers optical fibers by symmetrically heating a fiber optic (or imaging fiber optic in our case) while gently pulling them apart at a constant force. Once the fiber optic begins to be pulled at a specified velocity, the heat source (CO<sub>2</sub> laser) is turned off for a specified amount of time. After which, a solenoid pulls the fiber optic apart with a specified force. The adjustable parameters are HEAT, FIL VEL, DEL, and PULL adjusting the heat, filament, velocity, delay, and pull, respectively, which are outlined below.

- HEAT: 0 – 999; defines the output of the laser power with larger values providing higher heat
- FIL (filament): 0 – 15; controls the scanning pattern of the beam with smaller values providing a tighter (smaller) scanning pattern
- VEL (velocity): 0 – 255; controls the velocity of the puller bar (by gravity pulling) required to move on to the next parameter with smaller values providing a slower velocity and larger values providing a higher velocity

- DEL (delay): 0 – 255; controls the timing between the HEAT parameter being engaged and the solenoid pull (PULL parameter, below) with a value of 128 being a delay of zero seconds, values greater than 128 increase the time between the VEL parameter condition being met and PULL while values below 128 extend the time the HEAT parameter is engaged while the PULL parameter is also engaged
- PULL: 0 – 255; controls the force at which the solenoid pulls the bundles apart with smaller values pulling with less force and larger values pulling with more force

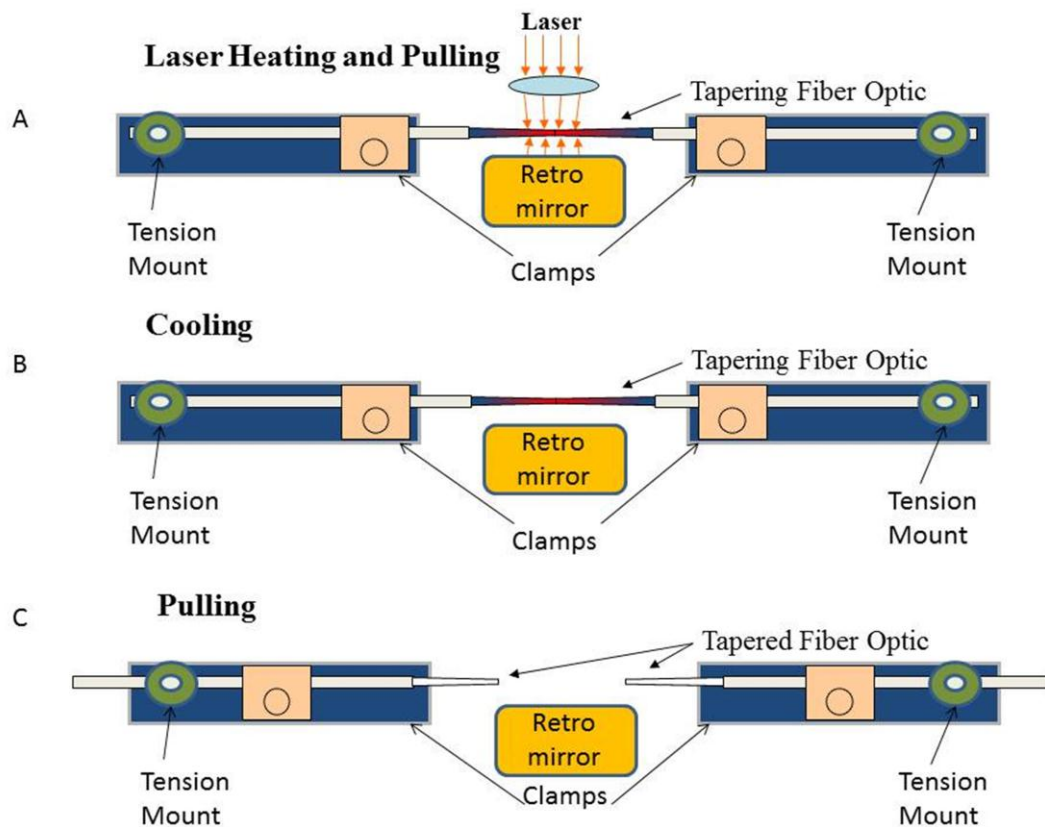
Programs created on the instrument can be saved for use at a later date. An example of one such program that was used to create imaging fiber bundles with 232nm fiber elements is described in Table A1. The general structure of this program is for lines 1-3 to provide a tapered region on the bundle that is relatively shallow in its taper (i.e. small angle of taper) providing a gradual decrease in size. Lines 4 and 5 are to produce a sharp taper with a large angle.

A pictorial representation of the micropipette puller and how it works is presented in Figure A1. The puller works by first heating the fiber optics and pulling at a constant

**Table A1:** A multi-line pulling program used to pull the imaging fiber bundle used in Chapter 2 of this dissertation with 232nm fiber elements.

Line Number	Heat	Filament	Velocity	Delay	Pull
1	500	4	18	126	150
2	450	3	19	200	200
3	450	3	20	200	250
4	600	2	60	200	75
5	700	1	60	200	75

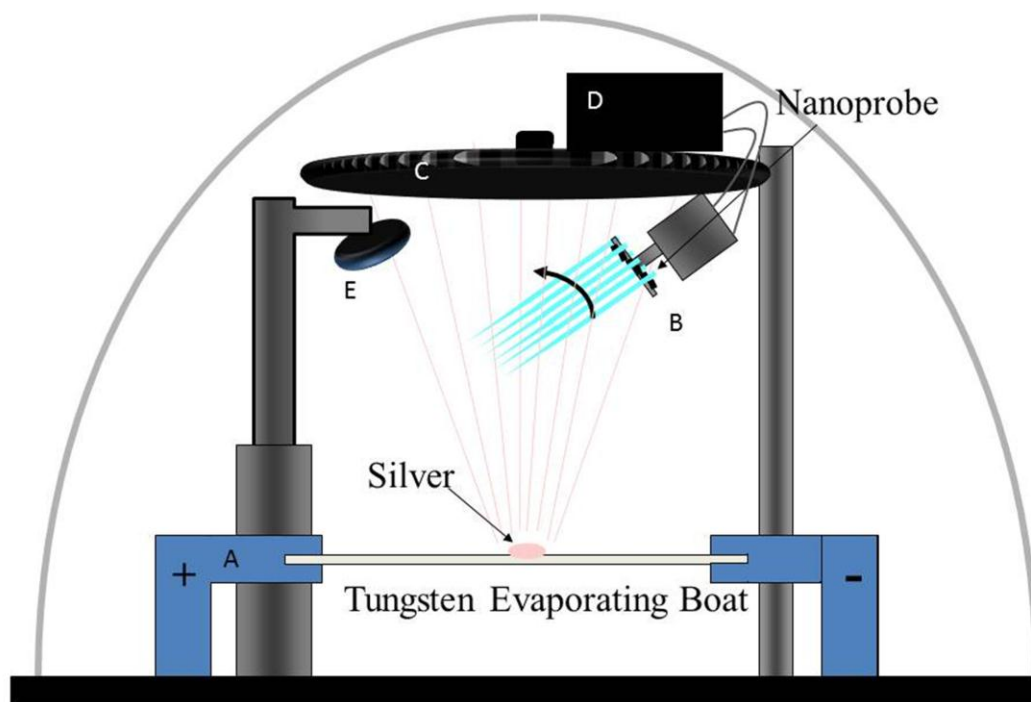
force until the velocity target is met utilizing the parameters HEAT, PUL, and VEL. This is represented in Figure A1A. After the velocity parameter has been satisfied, the laser is turned off and the system is allowed to cool for the specified time in delay using the DEL parameter and pictorial represented in Figure A1B. Finally, after the delay parameter is satisfied, the pull parameter starts, pulling a specified force, as determined by the PUL parameter, and pictorial represented in Figure A1C.



**Figure A1:** A pictorial representation of the steps the micropipette puller uses for a full pull. A) The laser is on, heating the fiber optic with a certain amount of heat and at a particular filament size until the velocity criteria is met. B) the fiber optic then cools for the set delay time followed by C) a hard pull by the solenoid.

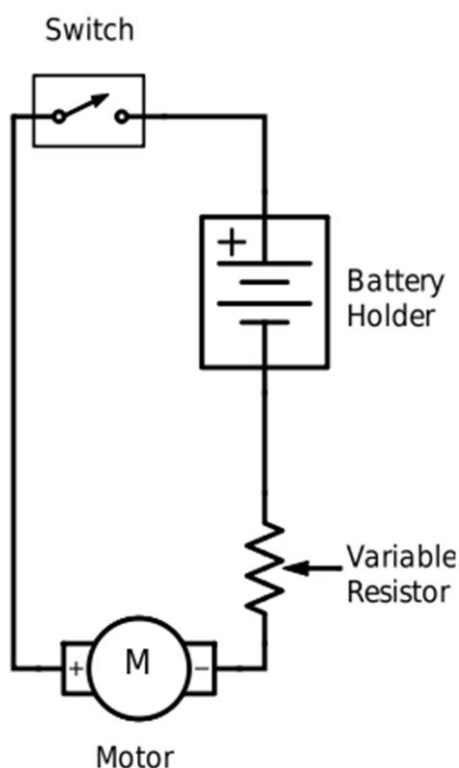
## Appendix B: Physical Vapor Deposition

A Denton Vacuum Explorer physical vapor deposition system (herein PVD system) was used for all depositions on fiber bundles. Figure B1 shows an annotated picture of the Denton Vacuum Explorer. The PVD system is composed of primarily a glass bell jar, tungsten evaporating boat, and a rotating disk. For this particular application, the rotating disk is not used. The bell jar is capable of maintaining vacuum at or below the micro-torr regime with use of a high-vacuum pump.



**Figure B1:** An annotated image of the Denton Vacuum Explorer. A) The anode and cathode connecting the tungsten evaporating boat that is loaded with silver. B) the rotating motor apparatus with attached fiber bundles mounted on an aluminum flat bar that is angled at 45° (not shown). C) rotating disk that allows for mounting above the W boat. D) power controller for the rotating motor apparatus. E) quartz-crystal microbalance for precise measurement of the amount of metal deposited on the bundles.

The fiber bundles were held in a custom-built bundle holder for the deposition process. The circuit diagram of the power controller is outlined in Figure B2. A variable resistor is used to change the speed of the motor. The motor (1.5 – 3V; 12,000RPM) was mounted at approximately 45 degrees, above and slightly offset from the tungsten evaporating boat. A pinion gear (10 teeth) was mounted at the end of the motor, and the bundles are placed between the teeth of the gear. The bundles were held in place in two ways: they are first seated between teeth with a narrow piece of double-sided tape. Once all the bundles are in place for the deposition, Kapton tape was to keep the bundles in place while rotating. Kapton tape is heat and low-pressure resistant making it ideal for use inside the PVD system. The motor apparatus is held to the rotating disk with two binder clips via an angled aluminum flat bar.



**Figure B2:** Circuit diagram of the circuit used for the rotating motor in the deposition of metals on the fiber bundles.

## **Appendix C: Characterization of the AOTF**

The AOTF was characterized in several ways to validate the images provided were at the selected wavelength and to ensure that the overlap between the wavelengths selected were negligible. The parameters evaluated were:

- Reproducibility
- Spectral resolution
- Spectral response

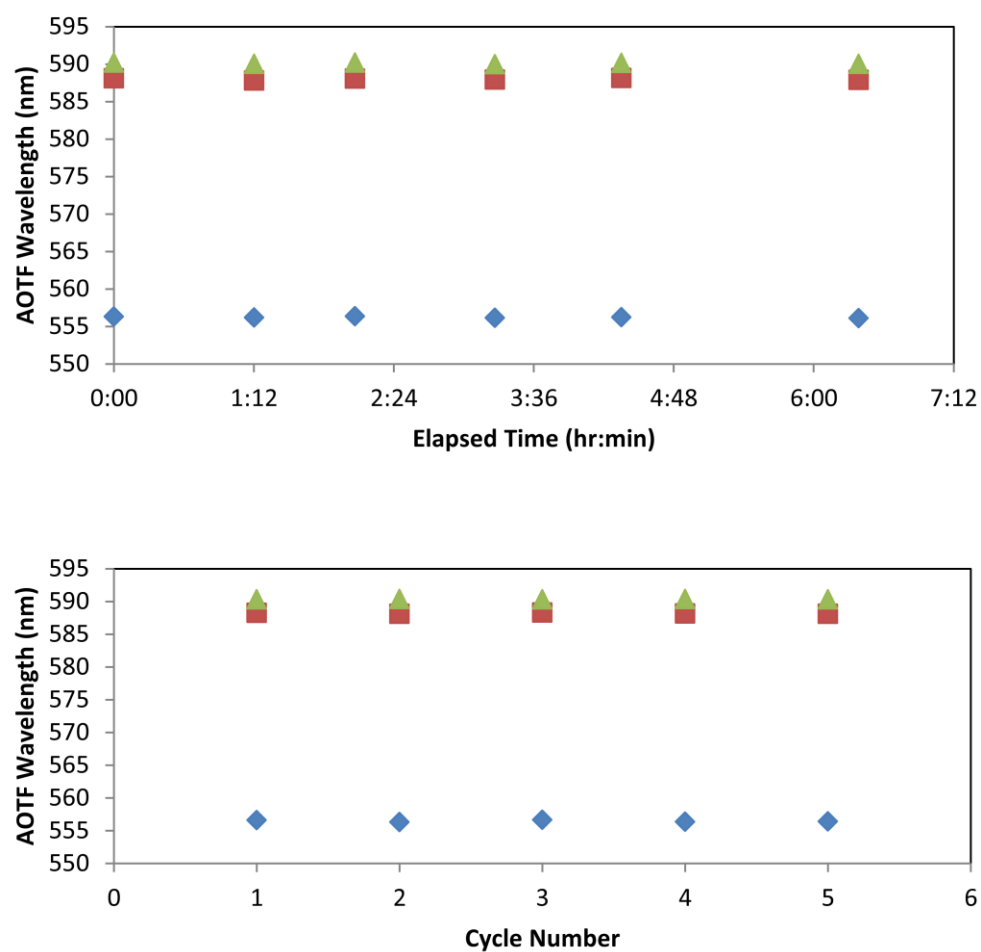
All characterizations were completed using an intensified CCD (PIMAX 1) inline with the AOTF imaging a fiber-optic coupled HgAr lamp.

### *C.1 Reproducibility*

The AOTF was evaluated for reproducibility. This was completed to ensure that the time the AOTF was on and running had no effect on the wavelength it was passing and to ensure the cycling the AOTF on and off from day-to-day did not effect to output. To evaluate the run-time effect on the AOTF, the AOTF was warmed up for the manufacturer's recommended 15 minutes. Then the AOTF was adjusted such that the highest intensity of the HgAr line was incident on the ICCD. The wavelength was then recorded. This was completed with the 546.08nm, 576.96nm and the 579.07nm atomic lines from a HgAr lamp. Over the course of seven hours, the peaks of the laser lines were evaluated. This can be seen in Figure C1A. Additionally, the number of times in which the AOTF was cycled on and off was also evaluated. The AOTF was turned on, allowed to warm up for 15 minutes, and an image was obtained. The AOTF was then turned off

and allowed to cool for a minimum of 20 minutes before turning back on again. This can be seen in Figure C1B. Both cycling and constant running had no effect on the output of the AOTF.

### C.2 Spectral Resolution



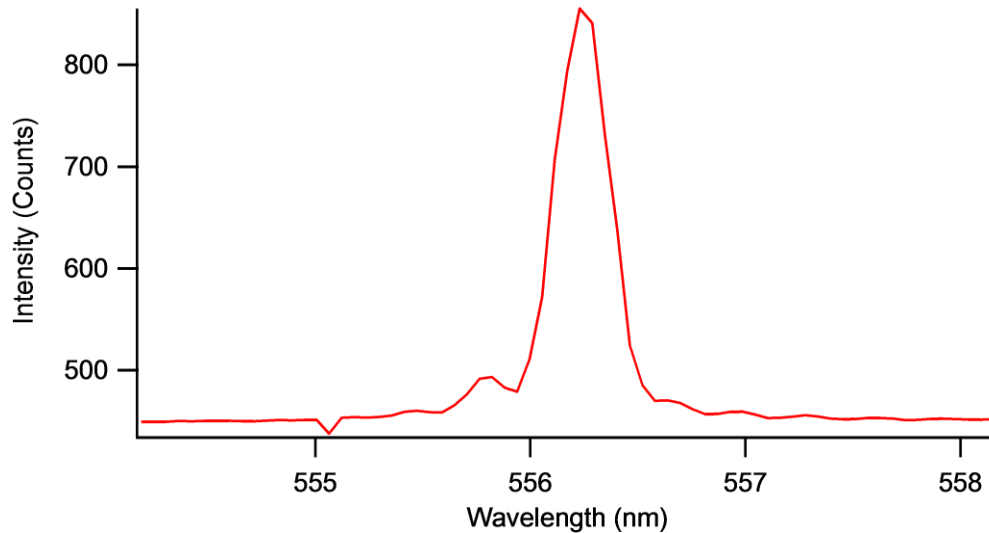
**Figure C1:** Reproducibility of the AOTF, as determined by its output. (A)

Reproducibility with respect to elapsed time of being turned on; (B) reproducibility with respect to number of cycles on and off.

In order to evaluate the spectral resolution of the AOTF and thus the system used, the width of what is being measured must be smaller than the resolution afforded by the equipment. As such, the HgAr lamp was used to determine the spectral resolution. In order to process the images for this, a program was written in order to autonomously process the files. These processes are described in detail below.

An automated program was created using IGOR Pro (version 6.1.2.1, WaveMetrics, Inc.) to do the following:

1. Obtain user input on the number of files, region of interest (ROI), and the x and y axis lengths
2. Create a wave for the wavelength function the data is plotted against
3. Make a wave for the data to be input into
4. Grab a file from a folder and upload the information into IGOR Pro
5. Unfold the matrix and capture the intensity values at each pixel
6. Define and obtain the ROI intensity values into a one-dimensional wave for analysis



**Figure C2:** A spectrally resolved atomic peak from the HgAr lamp as produced with the AOTF used for the analysis of the spectral resolution.



7. Average the intensity values and input into wave for graph
8. Plot the intensity of the ROI as a function of wavelength

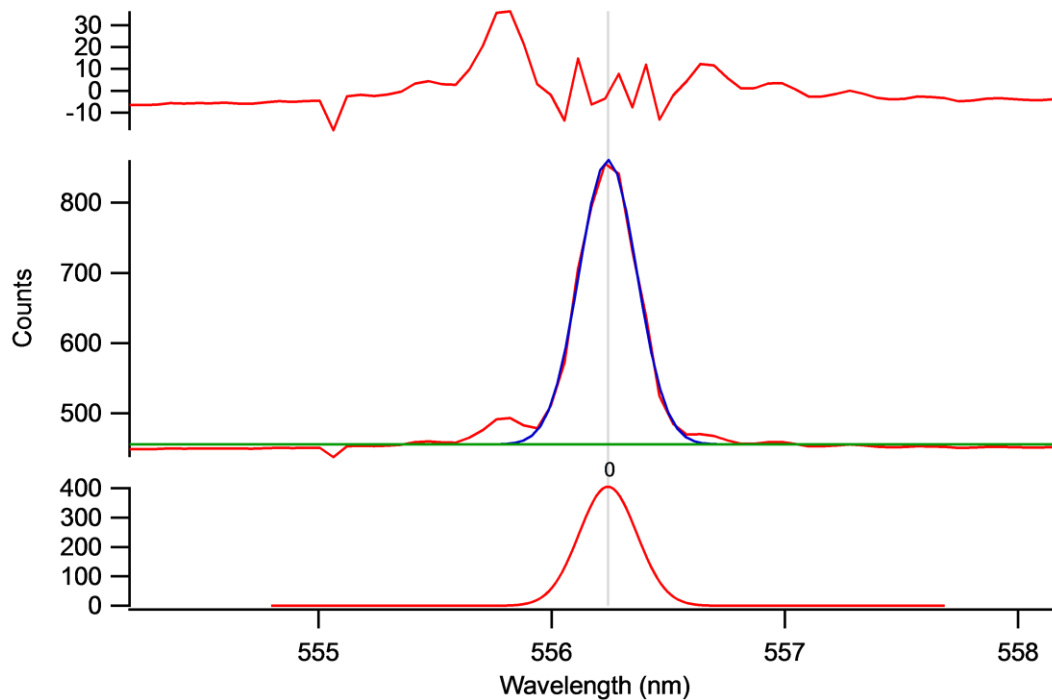
Figure C2 is a representative sample of output from the program discussed above. This particular graph was made from the analysis of 69 files from wavelengths 554.191-558.239 nm according to the AOTF interface (this is offset from the actual wavelength of 546nm from a Hg/Ar lamp).

Each file contains 262,144 pixels of information, of which a ROI was obtained consisting of 24,564 pixels, incorporating the entire region of contrastable information that is wavelength dependent on our ICCD. Once this information was captured from the ROI, the intensity values were averaged and output into the wave for inclusion into the graph. This was then repeated for the remaining 68 files, creating the graph as seen in Figure C2.

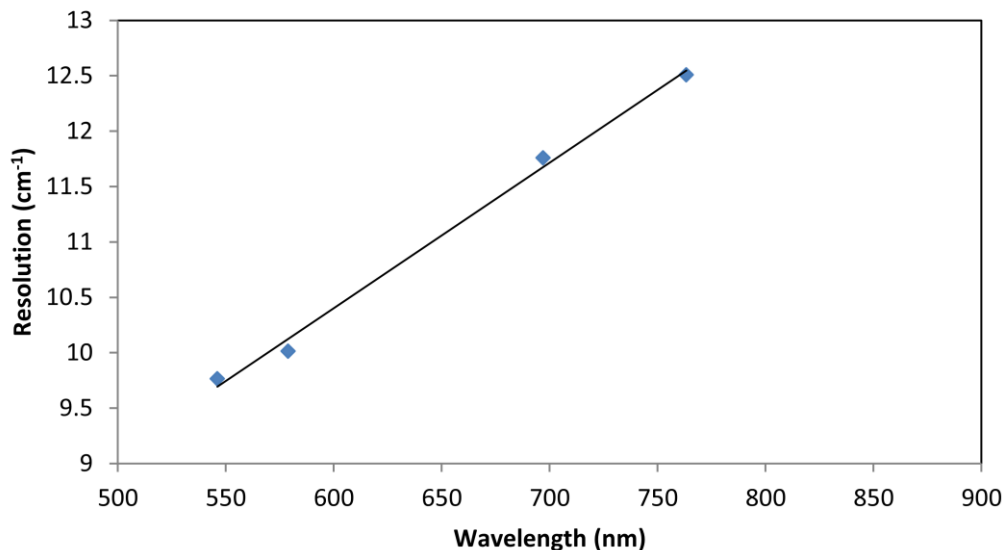
Next, the Multipeak Fitting package in IGOR Pro was used to analyze the curve that that the custom program output, as seen in Figure C3. This package automatically finds each peak and provides the peak location, amplitude, area, full width of the peak at half the maximum peak height (FWHM), width, height and the associated uncertainties associated with these values. Furthermore, it provides a graph with the residuals (Figure C3, top), the Gaussian fit to the data (Figure C3, middle) and the Gaussian by its self (Figure C3, bottom). The baseline (Figure C3, green, middle) is automatically calculated by the package, but can be modified into a constant value, or some function.

Figure C4 is the spectral resolution as a function of wavelength. The spectral resolution for each point was obtained by using the Multipeak fitting package in IGOR Pro, and analyzing the output of the fitted data. This computation was completed in Excel as follows:

1. The peak location was found
2. The FWHM was then divided in two, and both added and subtracted from the peak location yielding a range of wavelengths that incorporated the FWHM (i.e. 545.963-546.254nm).



**Figure C3:** The Gaussian fit output from the analysis. The bottom is the Gaussian fit by minimizing the adjustable parameters, as seen in the middle section, which is an overlay of the fit (blue) and data (red). The top is the residuals to show the goodness of fit.



**Figure C4:** The spectral resolution of the AOTF as a function of the wavelength employed.

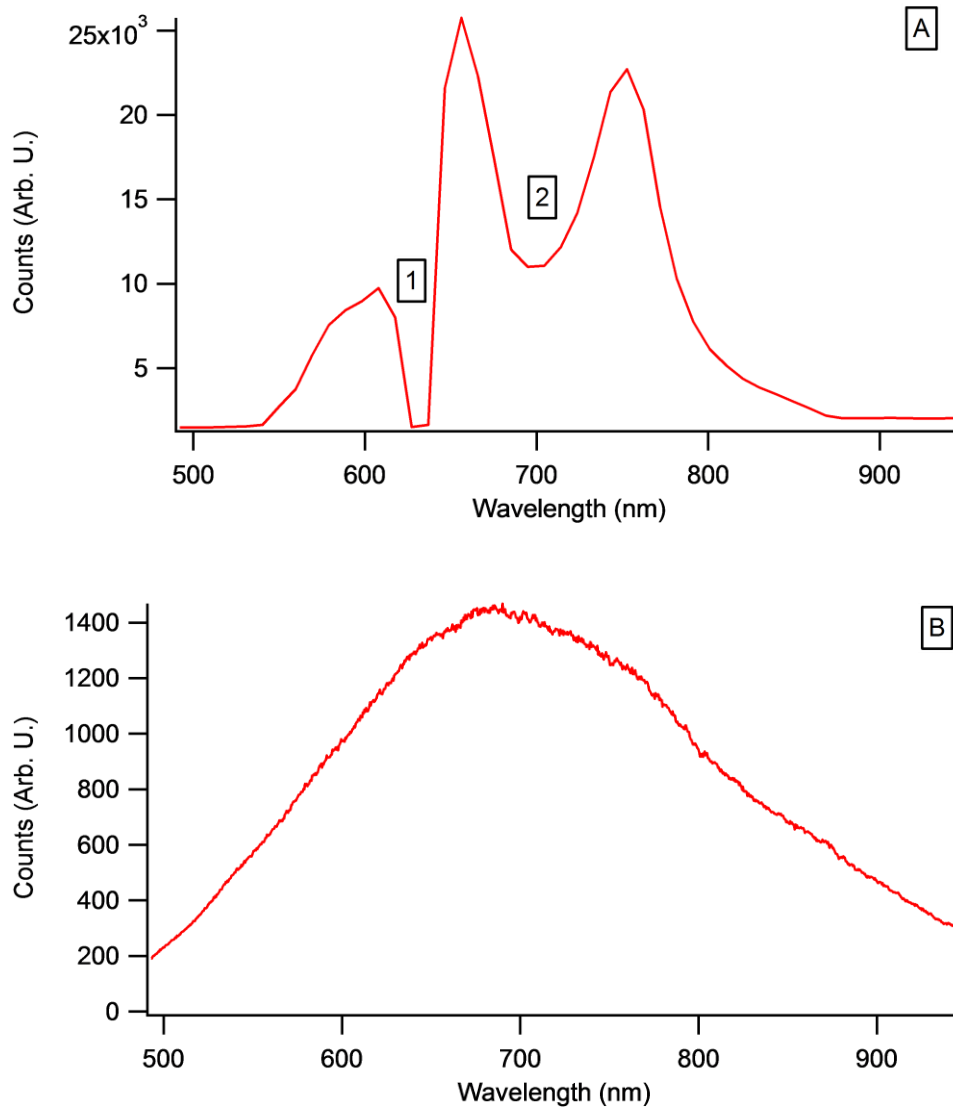
3. This wavelength range was then converted into wavenumbers (i.e. 18316.27-18306.50cm<sup>-1</sup>).
4. The difference of these wavenumbers is the spectral resolution at 50% contrast between two adjacent peaks.
5. Plotting these differences as a function of wavelength and using a best fit line via the LINEST function on Excel yields Figure C3.

The spectral resolution is increasing as a function of wavelength, from approximately 9.5 – 12.5cm<sup>-1</sup>, as expected. Furthermore, the range of wavelengths incorporated in this study was from 546 – 760nm.

### *C.3 Spectral Response*

Finally, the spectral responsivity of this system was obtained. This was completed by tuning the AOTF from its minimum (501.146nm) to its maximum (969.107nm) in 10nm increments while illuminating with an Ocean Optics Micropack UV-VIS-NIR deuterium

tungsten light source, whereby only the tungsten light source was used for the broadband emission. As seen in Figure 5, there are two areas of interest. The first decrease in the observed values in area 1, Figure 5, is due to the notch filter filtering 632.8nm light; this filters out 627nm-637nm light. However, there is an additional decrease in intensity, seen in area 2, Figure 5 which is not due to any filters. The source of this decrease is actually



**Figure C5:** (A) The spectral response as obtained through the AOTF. (B) A spectrum of the tungsten source used to create (A).

an artifact of the AOTF itself, and is not due to any filters. This was confirmed with the manufacturer.

#### *C.4 IgorPro Program for Spectral Resolution*

//This Procedure plots each image individually in succession

//Modified by Eric Languirand on 07/30/2014

#pragma rtGlobals=3 // Use modern global access method and strict wave access.

Macro Pierreimaging2(numend, cstart, cend, rstart, rend, SFile, EFile) // Put all the variables in the parenthesis

Variable numend // Variable for the number of data points

Variable cstart // Variable for the column number start for ROI

Variable Cend // Variable for the column number end for ROI

Variable Rstart // Variable for the starting row for the ROI

Variable Rend // Variable for the ending row for the ROI

Variable SFile // Starting file number

Variable EFile // Ending File number

Prompt SFile, "Starting File"

Prompt Efile, "Ending File"

Prompt numend, "Number of Data points in each axis"

Prompt Cstart, "Column Start for ROI"

Prompt Cend, "Column end for ROI"

Prompt Rstart, "Row Start for ROI"

Prompt Rend, "Row end for ROI"

string specres

string FileName

Variable i = Sfile

Variable j = 0

Variable k = 0

Variable Avg

Variable inc

Inc = 1

```

//make/n = (((efile - sfile)/inc) + 1) lambda763
// increment for file number
//make/o /n = (((Efile - SFile)/inc) + 1) SpecRes763 // empty
matrix for storing data for plot for spectral resolution
Variable BB=0

//lambda763 = (0.072704*x)+778.46

//do loop for adding data to open matrix
do
    Loadwave /P=Nasa /A /J /K=1 num2str(i)+".txt" // To load each .txt
    file name from the path selected

    Duplicate /o wave2, Zaxis
    // Duplicating the wave permits to not confuse Igor with the inherent file
    appellation (wave0...)
    Make /n=(numend,numend) Mainmatrix //
    WHILE LOOP For image propagation from raw data

        // WHILE LOOP
        Do
            // WHILE LOOP

                Mainmatrix[][BB]=Zaxis
            // WHILE LOOP
            BB=BB+1
        // WHILE LOOP

        While (BB<numend)
    // WHILE LOOP

        Duplicate /o Mainmatrix, $(SpecRes+num2istr(k))
        // Duplicating the matrix into the name of the image matrix to perform
        several imaging in the same time without taking one for another one

        //duplicate/r = (rstart, rend)(cstart, cend) outBName, ROI
    //Grabbing ROI from image matrix
        //Redimension/n = ((rend -rstart+1) * (cend -cstart+1)) ROI
    //Redimensioning from large matrix to XY matrix
        //wavestats ROI;
        //obtaining average and standard deviation from all points in ROI
        //Avg = V_avg

    //SpecRes763 [j] = Avg
    //specRes [][k] = ((Sfile + i)*0.001)
    display; appendimage $(specres+num2istr(K))

```

```

i=i+inc
j= j+1
k=k+1
BB=0
killwaves mainmatrix, wave0, wave1, wave2
// To avoid errors

//incoproate new graph for spectral resolution
While (i<=Efile)
//display specres763 vs lambda763

//Display;AppendImage $(outBName) // To plot the image without using the tool bar

```

## Appendix D: POCS Algorithm

This appendix provides the projection over convex sets (POCS) super resolution reconstruction algorithm used in MATLABR2014b to provide the high-resolution images in Chapter 3 and Chapter 4 of this dissertation. The inputs required for this program to run are:

1. 8-bit low-resolution TIFF image files, sequentially numbered
2. Translational movements in pixel values in an excel file in specified cells with 'x' translations in the first column and 'y' translations in the second column

The adjustable parameters described below. The name of the adjustable parameter is listed first, along with the type of variable it is, separated by a colon. The types of variables are integers (*i*), strings (*s*) and cell arrays (*c*).

base : *s* The non-changing first part of the file name for loading images. This must match the beginning of the filenames for the low-resolution images

ext : *s* The extension of the filename, including any non-changing filename that comes after the iteration of the file number; the extension should always end with '.tiff'

list : *c* The list is a cell array of the integers of the file numbers to be included in the reconstruction. For example, if 18 images are obtained, but only every



other image is to be included in the list for analysis, the list parameter would read “list = {1 3 5 7 9 11 13 15 17};”

fn : *s* This is a complete filename for the Excel file that lists the translations

delta\_est : *s* This variable loads the Excel file defined by fn, loading the sheet the data is on (Sheet1) in the specified cells (H6:I21). Both sheet and specified cells should be changed as needed

factor : *i* Defines the decimation ratio for the reconstruction algorithm and increases the matrix from the size of the lower-resolution images by a factor of ‘factor’.

numIm = *i* Defines the number of images used in the reconstruction process

base2A : *s* Defines the first part of the filename for the saved image prior to number of images used total

base2B : *s* Defines the second part of the filename for the saved image file

The output of this algorithm is a reconstructed, high-resolution image that has a factor times more pixels in it than the original lower-resolution images input in the program and is saved as the user-specified file name of the concatenated form of:

base2A,num2str(numIm), base2B, num2str(factor),ext.

## Projection of Convex Sets Super Resolution Reconstruction Algorithm

```
% Commented out from original program; inputs further in program

% function y = pocs(s,delta_est,factor)
% POCS - reconstruct high resolution image using Projection On Convex Sets
%   y = pocs(s,delta_est,factor)
%   reconstruct an image with FACTOR times more pixels in both dimensions
%   using Papoulis Gerchberg algorithm and using the shift and rotation
%   information from DELTA_EST and PHI_EST
%   in:
%   s: images in cell array (s{1}, s{2},...)
%   delta_est(i,Dy:Dx) estimated shifts in y and x
%   factor: gives size of reconstructed image

% -----
% SUPERRESOLUTION - Graphical User Interface for Super-Resolution Imaging
% Copyright (C) 2005-2007 Laboratory of Audiovisual Communications (LCAV),
% Ecole Polytechnique Federale de Lausanne (EPFL),
% CH-1015 Lausanne, Switzerland
%
% This program is free software; you can redistribute it and/or modify it
% under the terms of the GNU General Public License as published by the
% Free Software Foundation; either version 2 of the License, or (at your
% option) any later version. This software is distributed in the hope that
% it will be useful, but without any warranty; without even the implied
% warranty of merchantability or fitness for a particular purpose.
% See the GNU General Public License for more details
% (enclosed in the file GPL).
%
% Latest modifications: August 29, 2017, by Eric Languirand
```

## Image Loading

```
%%%%%%%%%%%%%%%%%%%%%%%%%%%%%%%%%%%%%%%%%%%%%%%%%%%%%%%%%%%%%%%%%%%%%%%%
% List images in a cell array here %
%%%%%%%%%%%%%%%%%%%%%%%%%%%%%%%%%%%%%%%%%%%%%%%%%%%%%%%%%%%%%%%%%%%%%%%%

clear all; % Clears all variables from workspace

base = 'DitherHgArLamp'; % Base for filename
ext = '_1.tif'; % Extension for filename
```

```

% List of number iteration in group of images to be loaded
list = {1 2 3 4 5 6 7 8 9 10 11 12 13 14 15 16};
% Modify 'list', 'base', 'ext' as needed
% base = 'B';
% ext = '_NN50.tif';
% list = {1 2 3 4 5 6 7 8 9 10 11 12 13 14 15 16 17 18 19 20 21 22 23 24 25};
% list = {1 3 5 6 7 9 11 13 15 16 17 19 20 21 23 25};
% list = {1 3 5 11 13 15 21 23 25};
% list = {1 3 11 14};
% for loop to create cell array of images
for i=1:numel(list(:))
    s{i} = mat2gray(imread(strcat(base, num2str(list{i}),ext)));
end
% Note: Images must be in current folder to load

```

## Image Translations

```

%%%%%%%%%%%%%%%%%%%%%%%%%%%%%%%%%%%%%%%%%%%%%%%%%%%%%%%%%%%%%%%%%%%%%%%%
% List shifts here %
%%%%%%%%%%%%%%%%%%%%%%%%%%%%%%%%%%%%%%%%%%%%%%%%%%%%%%%%%%%%%%%%%%%%%%%%

% Excel file name that lists shift; must be in workspace to load
fn = 'ShiftParameters_3_2_15.xlsx';
% Reading of the Excel file; H6:I21 is the x and y column listing the
% shifts in pixels
delta_est = xlsread(fn,'Sheet1','H6:I21');

% fn = uigetfile;
% fn = 'MockDataDisplacements25Images.xlsx';
% delta_est = xlsread(fn);

```

## Miscellaneous Initializations

```

%%%%%%%%%%%%%%%%%%%%%%%%%%%%%%%%%%%%%%%%%%%%%%%%%%%%%%%%%%%%%%%%%%%%%%%%
% Provide Factor here %
%%%%%%%%%%%%%%%%%%%%%%%%%%%%%%%%%%%%%%%%%%%%%%%%%%%%%%%%%%%%%%%%%%%%%%%%

% Decimation ratio between high resolution grid and low resolution images
factor = 2;
% Number of images used in analysis
numIm = 16;

```

```
% Maximum iterations for convergences of the minimization criteria
max_iter = 1000;
```

## Initial High-resolution Grid

```
% Using first image in cell array of images to be placed on high resolution
% grid, upsamples by a factor of 'factor'.
temp = upsample(upsample(s{1}, factor)', factor)';
y = zeros(size(temp));
coord = find(temp);
y(coord) = temp(coord);

% Loading remaining images onto high resolution grid, translated by the
% known amount in Excel file ('delta_est').
for i = 2:length(s)
    temp = upsample(upsample(s{i}, factor)', factor)';
    temp = shift(temp, round(delta_est(i, 2)*factor), round(delta_est(i, 1)*factor));
    coord = find(temp);
    y(coord) = temp(coord);
end

y_prev=y;

E=[];      % Initializing empty matrix for iter and error logging
iter=1;    % Defining iteration variable
%
```

## Kernel Definition

```
% Custom PSF blurring kernel
blur = [0.016596235    0.016529564    0.017155952    0.017350107    0.016691736
        0.016204545    0.01649285;...
0.016556367    0.018262322    0.020814498    0.02168572    0.019667134    0.017167664
        0.016214906;...
0.017323079    0.020531148    0.027736296    0.033458476    0.026500414    0.019371846
        0.016707052;...
0.017600798    0.021337726    0.033016108    0.044758231    0.033124673    0.020999644
        0.017164511;...
0.016795345    0.019362386    0.025865692    0.032797627    0.027400016    0.02027325
        0.017129599;...
0.016240809    0.017083876    0.018985788    0.020538356    0.019756779    0.018011407
```

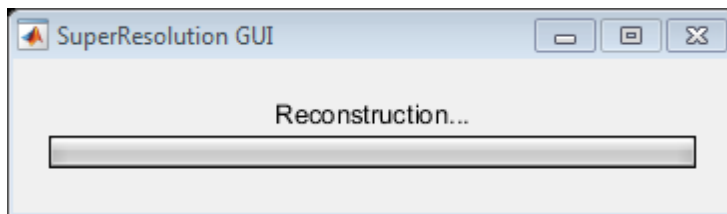
```

0.016680474;...
0.016509968    0.016073907    0.016415143    0.016880711    0.016833185    0.016526636
0.016819446];

% Standard blurring kernel
% blur =[ 1 2 1;...
%        2 4 2;...
%        1 2 1];

% Initialization of wait bar for progress of reconstruction
blur = blur / sum(blur(:));
wait_handle = waitbar(0, 'Reconstruction...', 'Name', 'SuperResolution GUI');

```



## Iterations for Reconstruction

```

% While loop proceeds from iter = 1 through max_iter (=1000), blurring
% image matrix y with blurring kernel.
while iter < max_iter
    waitbar(min(4*iter/max_iter, 1), wait_handle);
    y = imfilter(y, blur);
    % Secondary comparative image matrix formed based on translations,
    % loaded last image to reference
    for i = length(s):-1:1
        temp = upsample(upsample(s{i}, factor)', factor)';
        temp = shift(temp, round(delta_est(i, 2)*factor), round(delta_est(i, 1)*factor));
        coord = find(temp);
        y(coord) = temp(coord);
    end

    % Euclidean norm of the original, blurred image compared with the
    % Euclidean norm of the secondary comparative image matrix. The norms
    % are a column-sum total of the magnitude of the values present within
    % the matrix; minimizing the difference between the two norms provides
    % a reconstruction most closely resembling the the true image

```

```

delta= norm(y-y_prev)/norm(y);
E=[E; iter delta];
iter = iter+1;
% Iterate until difference is less than 1x10-6
if iter>3
    if abs(E(iter-3,2)-delta) <1e-6
        break
    end
end
y_prev=y;
% if mod(iter,10)==2
%     disp(['iteration ' int2str(E(iter-1,1)) ', error ' num2str(E(iter-1,2))])
% end
end

```

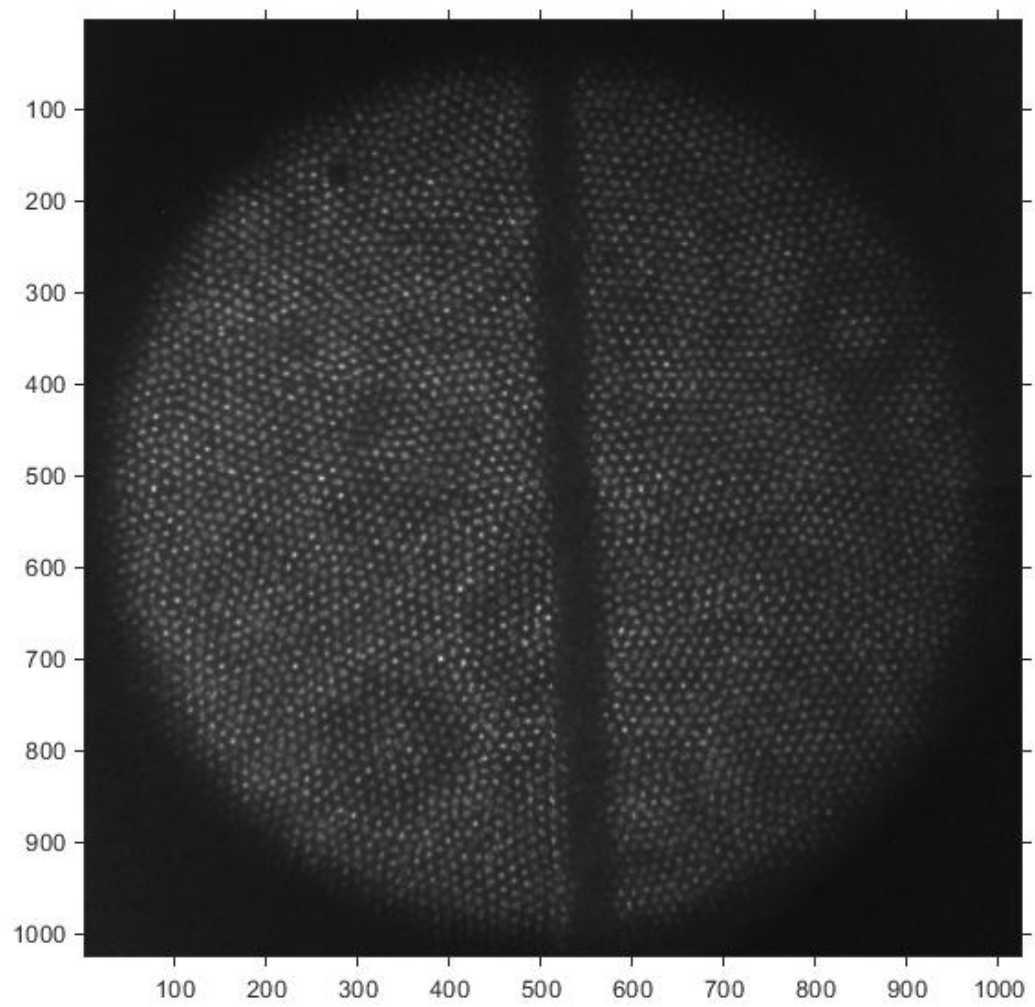
## Saving Data

```

% Base filenames for the saved imgae
base2A = 'TEST_';
base2B = 'Images_Factor';
% Assigning reconstructed image matrix y to matrix A and converting the
% values to 8-bit and reducing to values normalized to 1 (i.e. all
% intensity values are represented from 0 -> 1.)
A = mat2gray(y);
imshow(A)
% Writing an image file as a .tif
imwrite(A, strcat(base2A, num2str(numIm), base2B, num2str(factor), ext));
% Closing the handle associated with the wait bar
close(wait_handle);

Warning: Image is too big to fit on screen; displaying at 50%

```



*Published with MATLAB® R2014b*

## Bibliography

Aslan K, Geddes CD. (2010) Metal-Enhanced Fluorescence: Progress Towards a Unified Plasmon-Fluorophore Description. In Metal-Enhanced Fluorescence: John Wiley & Sons, Inc., 1-23 pp.

Betzig E, Lewis A, Harootunian A, Isaacson M, Kratschmer E. (1986) Near Field Scanning Optical Microscopy (NSOM): Development and Biophysical Applications. Biophysical journal 49 (1): 269-279.

Betzig E, Lewis A, Harootunian A, Isaacson M, Kratschmer E. (1986) Near Field Scanning Optical Microscopy (NSOM): Development and Biophysical Applications. Biophysical journal 49 (1): 269-279.

Betzig E, Patterson GH, Sougrat R, Lindwasser OW, Olenych S, Bonifacino JS, Davidson MW, Lippincott-Schwartz J, Hess HF. (2006) Imaging Intracellular Fluorescent Proteins at Nanometer Resolution. Science 313 (5793): 1642-1645.

Boyack R, Le Ru EC. (2009) Investigation of particle shape and size effects in SERS using T-matrix calculations. Phys. Chem. Chem. Phys. 11 (34): 7398-7405.

Carminati R, Greffet JJ, Henkel C, Vigoureux JM. (2006) Radiative and non-radiative decay of a single molecule close to a metallic nanoparticle. Optics Communications 261 (2): 368-375.



Centeno A, Xie F. (2014) Towards optimizing metal enhanced fluorescence (MEF) for improved detection of disease biomarkers. *Biointerface Research in Applied Chemistry* 4 (3): 731-735.

Chan KLA, Hammond SV, Kazarian SG. (2003) Applications of Attenuated Total Reflection Infrared Spectroscopic Imaging to Pharmaceutical Formulations. *Analytical Chemistry* 75 (9): 2140-2146.

Chang Y-F, Tsao K-C, Liu Y-C, Chen Y-C, Yu P-C, Huang Y-C, Chou C. (2015) Diagnosis of human metapneumovirus in patients hospitalized with acute lower respiratory tract infection using a metal-enhanced fluorescence technique. *Journal of Virological Methods* 213 (0): 151-156.

Chen B-C, Legant WR, Wang K, Shao L, Milkie DE, Davidson MW, Janetopoulos C, Wu XS, Hammer JA, Liu Z, English BP, Mimori-Kiyosue Y, Romero DP, Ritter AT, Lippincott-Schwartz J, Fritz-Laylin L, Mullins RD, Mitchell DM, Bembenek JN, Reymann A-C, Böhme R, Grill SW, Wang JT, Seydoux G, Tulu US, Kiehart DP, Betzig E. (2014) Lattice light-sheet microscopy: Imaging molecules to embryos at high spatiotemporal resolution. *Science* 346 (6208).

Chen X, Reichenbach KL, Xu C. (2008) Experimental and theoretical analysis of core-to-core coupling on fiber bundle imaging. *Opt. Express* 16 (26): 21598-21607.

Cheng H, Wang C, Xu Z, Lin H, Zhang C. (2015) Gold nanoparticle-enhanced near infrared fluorescent nanocomposites for targeted bio-imaging. *RSC Advances* 5 (1): 20-26.

Corsi C. (2015) New frontiers for infrared. In *Opto-Electronics Review*, p. 3

Cristani M, Cheng DS, Murino V, Pannullo D. (2004) Distilling information with super-resolution for video surveillance. In *Proceedings of the ACM 2nd international workshop on Video surveillance & sensor networks*, pp. 2-11. New York, NY, USA: ACM

Crivoi A, Duan F. (2014) Three-dimensional Monte Carlo model of the coffee-ring effect in evaporating colloidal droplets. *Scientific Reports* 4: 4310.

Cullum BM, Li H, Hankus ME, Schiza MV. (2007) Characterization of multilayer-enhanced surface-enhanced raman scattering (SERS) substrates and their potential for SERS nanoimaging. *Nanobiotechnol* 3 (1): 1-11.

Daghestani HN, Day BW. (2010) Theory and Applications of Surface Plasmon Resonance, Resonant Mirror, Resonant Waveguide Grating, and Dual Polarization Interferometry Biosensors. *Sensors* 10 (11): 9630.

Darvill D, Centeno A, Xie F. (2013) Plasmonic fluorescence enhancement by metal nanostructures: shaping the future of bionanotechnology. *Physical Chemistry Chemical Physics* 15 (38): 15709-15726.

Deng W, Xie F, Baltar HTMCM, Goldys EM. (2013) Metal-enhanced fluorescence in the life sciences: here, now and beyond. *Physical Chemistry Chemical Physics* 15 (38): 15695-15708.

Doering WE, Nie S. (2002) Single-Molecule and Single-Nanoparticle SERS: Examining the Roles of Surface Active Sites and Chemical Enhancement. *The Journal of Physical Chemistry B* 106 (2): 311-317.

Dubertret B, Skourides P, Norris DJ, Noireaux V, Brivanlou AH, Libchaber A. (2002) In Vivo Imaging of Quantum Dots Encapsulated in Phospholipid Micelles. *Science* 298 (5599): 1759-1762.

Duponchel L, Milanfar P, Ruckebusch C, Huvenne J-P. (2008) Super-resolution and Raman chemical imaging: From multiple low resolution images to a high resolution image. *Analytica Chimica Acta* 607 (2): 168-175.

Elad M, Feuer A. (1997) Restoration of a single superresolution image from several blurred, noisy, and undersampled measured images. *Image Processing, IEEE Transactions on* 6 (12): 1646-1658.

Elad M, Hel-Or Y. (2001) A fast super-resolution reconstruction algorithm for pure translational motion and common space-invariant blur. *Image Processing, IEEE Transactions on* 10 (8): 1187-1193.

Emmons ED, Tripathi A, Guicheteau JA, Christesen SD, A. W. Fountain I. (2009) Raman Chemical Imaging of Explosive-Contaminated Fingerprints. *Applied Spectroscopy* 63 (11): 1197-1203.

Eustis S, El-Sayed MA. (2006) Determination of the aspect ratio statistical distribution of gold nanorods in solution from a theoretical fit of the observed inhomogeneously broadened longitudinal plasmon resonance absorption spectrum. *Journal of Applied Physics* 100 (4): 044324.

Evans CL, Xie XS. (2008) Coherent Anti-Stokes Raman Scattering Microscopy: Chemical Imaging for Biology and Medicine. *Annual Review of Analytical Chemistry* 1 (1): 883-909.

Farkas DL. (2003) Invention and commercialization in optical bioimaging. *Nat Biotech* 21 (11): 1269-1271.

Farsiu S, Robinson D, Elad M, Milanfar P. (2004) Advances and challenges in super-resolution. *International Journal of Imaging Systems and Technology* 14 (2): 47-57.

Farsiu S, Robinson M, Elad M, Milanfar P. (2004) Fast and robust multiframe super-resolution. *IEEE Transactions on Image Processing* 13 (10): 1327 - 1344.

Farsiu S, Robinson M, Milanfar P. (2004) MDSP resolution enhancement software.

Feng S, Dong F, Sun S, Zou Y, Zhou C. (2014) Performance analysis for two typical spatial domain super-resolution reconstruction algorithms. Proc. 2014 7th International Congress on Image and Signal Processing:353-358.

Fernandez-Suarez M, Ting AY. (2008) Fluorescent probes for super-resolution imaging in living cells. Nat Rev Mol Cell Biol 9 (12): 929-943.

Flusberg BA, Cocker ED, Piyawattanametha W, Jung JC, Cheung ELM, Schnitzer MJ. (2005) Fiber-optic fluorescence imaging. Nat Meth 2 (12): 941-950.

Geddes C, Lakowicz J. (2002) Editorial: Metal-Enhanced Fluorescence. J Fluoresc 12 (2): 121-129.

Geddes, C. D. (2010) Metal-Enhanced Fluorescence. Hoboken, New Jersey: John Wiley & Sons

Giepmans BNG, Adams SR, Ellisman MH, Tsien RY. (2006) The Fluorescent Toolbox for Assessing Protein Location and Function. Science 312 (5771): 217-224.

Gowen AA, O'Donnell CP, Cullen PJ, Bell SEJ. (2008) Recent applications of Chemical Imaging to pharmaceutical process monitoring and quality control. European Journal of Pharmaceutics and Biopharmaceutics 69 (1): 10-22.

Guggenheim EJ, Khan A, Pike J, Chang L, Lynch I, Rappoport JZ. (2016) Comparison of Confocal and Super-Resolution Reflectance Imaging of Metal Oxide Nanoparticles. PLoS ONE 11 (10): e0159980.

Hankus ME, Cullum BM. (2006) SERS probes for the detection and imaging of biochemical species on the nanoscale, 6380:638004-638004-638012.

Hankus ME, Gibson G, Chandrasekharan N, Cullum BM. (2004) Surface-enhanced Raman scattering (SERS): nanoimaging probes for biological analysis, 5588:106-116.

Hankus ME, Gibson GJ, Cullum BM. (2005) Characterization and optimization of novel surface-enhanced Raman scattering (SERS)-based nanoimaging probes for chemical imaging, 6007:600704-600704-600711.

Hankus ME, Li H, Gibson GJ, Cullum BM. (2006) Surface-Enhanced Raman Scattering-Based Nanoprobe for High-Resolution, Non-Scanning Chemical Imaging. Analytical Chemistry 78 (21): 7535-7546.

Hankus ME. (2008) Development and Characterization of Surface Enhanced Raman Scattering (SERS) Nanoimaging Probes. Masters. University of Maryland, Baltimore County, Baltimore, MD

- Haynes CL, Van Duyne RP. (2001) Nanosphere Lithography: A Versatile Nanofabrication Tool for Studies of Size-Dependent Nanoparticle Optics. *The Journal of Physical Chemistry B* 105 (24): 5599-5611.
- Hecht B, Sick B, Wild UP, Deckert V, Zenobi R, Martin OJF, Pohl DW. (2000) Scanning near-field optical microscopy with aperture probes: Fundamentals and applications. *The Journal of Chemical Physics* 112 (18): 7761-7774.
- Hell SW. (2007) Far-Field Optical Nanoscopy. *Science* 316 (5828): 1153-1158.
- Hell SW. (2009) Microscopy and its focal switch. *Nat Meth* 6 (1): 24-32.
- Hess ST, Girirajan TPK, Mason MD. (2006) Ultra-High Resolution Imaging by Fluorescence Photoactivation Localization Microscopy. *Biophysical journal* 91 (11): 4258-4272.
- Hess ST, Girirajan TPK, Mason MD. (2006) Ultra-High Resolution Imaging by Fluorescence Photoactivation Localization Microscopy. *Biophysical journal* 91 (11): 4258-4272.
- Hirano Y, Matsuda A, Hiraoka Y. (2015) Recent advancements in structured-illumination microscopy toward live-cell imaging. *Microscopy* 64 (4): 237-249.

Honigsmann A, Mueller V, Hell SW, Eggeling C. (2013) STED microscopy detects and quantifies liquid phase separation in lipid membranes using a new far-red emitting fluorescent phosphoglycerolipid analogue. *Faraday Discussions* 161 (0): 77-89.

Huang L, Oesterberg UL. (1995) Measurement of cross-talk in order-packed image fiber bundles, *2536*:480-488.

Huckabay HA, Armendariz KP, Newhart WH, Wildgen SM, Dunn RC. (2013) Near-Field Scanning Optical Microscopy for High-Resolution Membrane Studies. *Methods in molecular biology* (Clifton, N.J.) 950: 373-394.

Izeddin I, Specht CG, Lelek M, Darzacq X, Triller A, Zimmer C, Dahan M. (2011) Super-Resolution Dynamic Imaging of Dendritic Spines Using a Low-Affinity Photoconvertible Actin Probe. *PLoS ONE* 6 (1): e15611.

Jahncke CL, Paesler MA, Hallen HD. (1995) Raman imaging with near-field scanning optical microscopy. *Applied Physics Letters* 67 (17): 2483-2485.

Jérez Rozo JI, Zarow A, Zhou B, Pinal R, Iqbal Z, Romañach RJ. (2011) Complementary near-infrared and raman chemical imaging of pharmaceutical thin films. *Journal of Pharmaceutical Sciences* 100 (11): 4888-4895.



Johnson TW, Lapin ZJ, Beams R, Lindquist NC, Rodrigo SG, Novotny L, Oh S-H. (2012) Highly Reproducible Near-Field Optical Imaging with Sub-20-nm Resolution Based on Template-Stripped Gold Pyramids. *ACS Nano* 6 (10): 9168-9174.

Kalasinsky KS, Hadfield T, Shea AA, Kalasinsky VF, Nelson MP, Neiss J, Drauch AJ, Vanni GS, Treado PJ. (2007) Raman Chemical Imaging Spectroscopy Reagentless Detection and Identification of Pathogens: Signature Development and Evaluation. *Analytical Chemistry* 79 (7): 2658-2673.

Katzenmeyer AM, Holland G, Kjoller K, Centrone A. (2015) Absorption Spectroscopy and Imaging from the Visible through Mid-Infrared with 20 nm Resolution. *Analytical Chemistry* 87 (6): 3154-3159.

Kazarian SG, Chan KLA. (2013) ATR-FTIR spectroscopic imaging: recent advances and applications to biological systems. *Analyst* 138 (7): 1940-1951.

Kelly KL, Coronado E, Zhao LL, Schatz GC. (2003) The Optical Properties of Metal Nanoparticles: The Influence of Size, Shape, and Dielectric Environment. *The Journal of Physical Chemistry B* 107 (3): 668-677.

Kim H, Bryant GW, Stranick SJ. (2012) Superresolution four-wave mixing microscopy. *Opt. Express* 20 (6): 6042-6051.

Kiser JB, Cullum BM. (2009) Tunable fiber-optic imaging bundle SERS substrates, 7313:73130E-73130E-73138.

Kiser JB, Cullum BM. (2010) Optical cross-talk and surface characterization of SERS nanoimaging bundle substrates, 7674:76740D-76740D-76748.

Kneipp K, Moskovits M, Kneipp H. (2006) Surface-Enhanced Raman Scattering: Physics and Applications. Springer Berlin Heidelberg,

Knight MW, King NS, Liu L, Everitt HO, Nordlander P, Halas NJ. (2014) Aluminum for Plasmonics. ACS Nano 8 (1): 834-840.

Kong YL, Boulogne F, Kim H, Nunes J, Feng J, Stone HA. (2015) Deposition of Quantum Dots in a Capillary Tube. Langmuir 31 (45): 12560-12566.

Kovacs GTA, Maluf NI, Petersen KE. (1998) Bulk micromachining of silicon. Proceedings of the IEEE 86 (8): 1536-1551.

Kretschmann E, Raether H. (1968) Notizen: Radiative Decay of Non Radiative Surface Plasmons Excited by Light. In Zeitschrift für Naturforschung A, p. 2135

Kuhn H. (1970) Classical Aspects of Energy Transfer in Molecular Systems. The Journal of Chemical Physics 53 (1): 101-108.

Kümmerlen J, Leitner A, Brunner H, Aussenegg FR, Wokaun A. (1993) Enhanced dye fluorescence over silver island films: analysis of the distance dependence. *Molecular Physics* 80 (5): 1031-1046.

Lakowicz J. (1999) *Principles of Fluorescence Spectroscopy*. New York, Boston, Dordrecht, London, Moscow: Kluwer Academic/Plenum Publishers,

Lakowicz JR, Shen B, Gryczynski Z, D'Auria S, Gryczynski I. (2001) Intrinsic Fluorescence from DNA Can Be Enhanced by Metallic Particles. *Biochemical and Biophysical Research Communications* 286 (5): 875-879.

Lakowicz JR. (2001) Radiative Decay Engineering: Biophysical and Biomedical Applications. *Analytical Biochemistry* 298 (1): 1-24.

Le Ru EC, Blackie E, Meyer M, Etchegoin PG. (2007) Surface Enhanced Raman Scattering Enhancement Factors: A Comprehensive Study. *The Journal of Physical Chemistry C* 111 (37): 13794-13803.

Lewis A, Isaacson M, Harootunian A, Muray A. (1984) Development of a 500 Å spatial resolution light microscope: I. light is efficiently transmitted through  $\lambda/16$  diameter apertures. *Ultramicroscopy* 13 (3): 227-231.

Lichtman JW, Conchello J-A. (2005) Fluorescence microscopy. *Nat Meth* 2 (12): 910-919.

Live LS, Bolduc OR, Masson J-F. (2010) Propagating Surface Plasmon Resonance on Microhole Arrays. *Analytical Chemistry* 82 (9): 3780-3787.

Lohumi S, Kim MS, Qin J, Cho B-K. (2017) Raman imaging from microscopy to macroscopy: Quality and safety control of biological materials. *TrAC Trends in Analytical Chemistry* 93 (Supplement C): 183-198.

Lu G, Fei B. (2014) Medical hyperspectral imaging: a review. *BIOMEDO* 19 (1): 010901-010901.

Maenosono S, Dushkin CD, Saita S, Yamaguchi Y. (1999) Growth of a Semiconductor Nanoparticle Ring during the Drying of a Suspension Droplet. *Langmuir* 15 (4): 957-965.

Maier SA. (2007) *Plasmonics: Fundamentals and Applications*. Springer US,

Malczewski K, Stasiński R. (2009) Super Resolution for Multimedia, Image, and Video Processing Applications. In *Recent Advances in Multimedia Signal Processing and Communications*, ed. M Grgic, K Delac, M Ghanbari. Berlin, Heidelberg: Springer Berlin Heidelberg, 171-208 pp.

Marks RJI. (1997) Alternating Projections onto Convex Sets. In *Deconvolution of Images and Spectra*, ed. PA Jansson: Academic Press, 476-501 pp.

McMahon JM, Schatz GC, Gray SK. (2013) Plasmonics in the ultraviolet with the poor metals Al, Ga, In, Sn, Tl, Pb, and Bi. *Physical Chemistry Chemical Physics* 15 (15): 5415-5423.

Milanfar, P. (2011) *Super-Resolution Imaging*. Boca Raton, FL: CRC Press

Morin R, Basarab A, Ploquin M, Kouamé D. (2012) Post-processing multiple-frame super-resolution in ultrasound imaging. *Proc. SPIE Medical Imaging*, San Diego, California, 8320:83201G. SPIE

Moskovits M. (1985) Surface-enhanced spectroscopy. *Reviews of Modern Physics* 57 (3): 783-826.

Moskovits M. (2005) Surface-enhanced Raman spectroscopy: a brief retrospective. *Journal of Raman Spectroscopy* 36 (6-7): 485-496.

National Research Council. (2006) *Visualizing Chemistry: The Progress and Promise of Advanced Chemical Imaging*. Washington, DC: The National Academies Press,

Offroy M, Moreau M, Sobanska S, Milanfar P, Duponchel L. (2015) Pushing back the limits of Raman imaging by coupling super-resolution and chemometrics for aerosols characterization. 5: 12303.

Offroy M, Roggo Y, Duponchel L. (2012) Increasing the spatial resolution of near infrared chemical images (NIR-CI): The super-resolution paradigm applied to pharmaceutical products. *Chemometrics and Intelligent Laboratory Systems* 117: 183-188.

Offroy M, Roggo Y, Milanfar P, Duponchel L. (2010) Infrared chemical imaging: Spatial resolution evaluation and super-resolution concept. *Analytica Chimica Acta* 674 (2): 220-226.

Orendorff CJ, Gearheart L, Jana NR, Murphy CJ. (2006) Aspect ratio dependence on surface enhanced Raman scattering using silver and gold nanorod substrates. *Phys. Chem. Chem. Phys.* 8 (1): 165-170.

Otto A. (1968) Excitation of nonradiative surface plasma waves in silver by the method of frustrated total reflection. *Z. Physik* 216 (4): 398-410.

Ovesný M, Křížek P, Borkovec J, Švindrych Z, Hagen GM. (2014) ThunderSTORM: a comprehensive ImageJ plug-in for PALM and STORM data analysis and super-resolution imaging. *Bioinformatics* 30 (16): 2389-2390.

Palombo F, Danoux CB, Weinberg PD, Kazarian SG. (2009) Measurement of drug and macromolecule diffusion across atherosclerotic rabbit aorta ex vivo by attenuated total reflection-Fourier transform infrared imaging. *J. Biomed. Opt.* 14 (4): 044008.

Park S, Park M, Kang M. (2003) Super-resolution image reconstruction: a technical overview. *IEEE Signal Processing Magazine* 20 (3): 21 - 36.

Patterson G, Davidson M, Manley S, Lippincott-Schwartz J. (2010) Superresolution Imaging using Single-Molecule Localization. *Annual Review of Physical Chemistry* 61 (1): 345-367.

Peddie CJ, Domart MC, Snetkov X, O'Toole P, Larijani B, Way M, Cox S, Collinson LM. (2017) Correlative super-resolution fluorescence and electron microscopy using conventional fluorescent proteins in vacuo. *Journal of Structural Biology*. 199(2):120-130

Phinn S, Roelfsema C, Dekker A, Brando V, Anstee J. (2008) Mapping seagrass species, cover and biomass in shallow waters: An assessment of satellite multi-spectral and airborne hyper-spectral imaging systems in Moreton Bay (Australia). *Remote Sensing of Environment* 112 (8): 3413-3425.

Pohl DW, Denk W, Lanz M. (1984) Optical stethoscopy: Image recording with resolution  $\lambda/20$ . *Applied Physics Letters* 44 (7): 651-653.

Qifang X, Guoqing Y, Pin L. (2017) Super-resolution Reconstruction of Satellite Video Images Based on Interpolation Method. *Procedia Computer Science* 107 (Supplement C): 454-459.

Qin J, Chao K, Kim MS, Cho B-K. (2016) Line-Scan Macro-scale Raman Chemical Imaging for Authentication of Powdered Foods and Ingredients. Food and Bioprocess Technology 9 (1): 113-123.

Qin J, Kim MS, Chao K, Schmidt WF, Cho B-K, Delwiche SR. (2017) Line-scan Raman imaging and spectroscopy platform for surface and subsurface evaluation of food safety and quality. Journal of Food Engineering 198 (Supplement C): 17-27.

Raghunathan V, Potma EO. (2010) Multiplicative and subtractive focal volume engineering in coherent Raman microscopy. J. Opt. Soc. Am. A 27 (11): 2365-2374.

Ray K, Lakowicz JR. (2013) Metal-Enhanced Fluorescence Lifetime Imaging and Spectroscopy on a Modified SERS Substrate. The Journal of Physical Chemistry C 117 (30): 15790-15797.

Rees EJ, Erdelyi M, Kaminski Schierle G, S. , Knight A, Kaminski C, F. . (2013) Elements of image processing in localization microscopy. Journal of Optics 15 (9): 094012.

Romain FL, Gabriele SKS, Sebastian van de L, Clemens FK. (2016) From single-molecule spectroscopy to super-resolution imaging of the neuron: a review. Methods and Applications in Fluorescence 4 (2): 022004.



- Ru EL, Etchegoin P. (2008) Principles of Surface-Enhanced Raman Spectroscopy: and related plasmonic effects. Elsevier Science,
- Rust MJ, Bates M, Zhuang X. (2006) Sub-diffraction-limit imaging by stochastic optical reconstruction microscopy (STORM). Nat Meth 3 (10): 793-796.
- Schmid T, Opilik L, Blum C, Zenobi R. (2013) Nanoscale Chemical Imaging Using Tip-Enhanced Raman Spectroscopy: A Critical Review. Angewandte Chemie International Edition 52 (23): 5940-5954.
- Schwartz B, Robbins H. (1976) Chemical Etching of Silicon: IV . Etching Technology. Journal of The Electrochemical Society 123 (12): 1903-1909.
- Serrano AL, Ghosh A, Ostrander JS, Zanni MT. (2015) Wide-field FTIR microscopy using mid-IR pulse shaping. Opt. Express 23 (14): 17815-17827.
- Sezan MI. (1992) An overview of convex projections theory and its application to image recovery problems. Ultramicroscopy 40 (1): 55-67.
- Shaner NC, Campbell RE, Steinbach PA, Giepmans BNG, Palmer AE, Tsien RY. (2004) Improved monomeric red, orange and yellow fluorescent proteins derived from *Discosoma* sp. red fluorescent protein. Nat Biotech 22 (12): 1567-1572.

Sharma H, Wood JB, Lin S, Corn RM, Khine M. (2014) Shrink-Induced Silica Multiscale Structures for Enhanced Fluorescence from DNA Microarrays. *Langmuir* 30 (37): 10979-10983.

Silva WR, Graefe CT, Frontiera RR. (2016) Toward Label-Free Super-Resolution Microscopy. *ACS Photonics* 3 (1): 79-86.

Small A, Stahlheber S. (2014) Fluorophore localization algorithms for super-resolution microscopy. *Nat Meth* 11 (3): 267-279.

Smith SW. (1997) The scientist and engineer's guide to digital signal processing. San Diego, California: California Technical Pub.,

Sonntag MD, Pozzi EA, Jiang N, Hersam MC, Van Duyne RP. (2014) Recent Advances in Tip-Enhanced Raman Spectroscopy. *The Journal of Physical Chemistry Letters* 5 (18): 3125-3130.

Sonntag MD, Pozzi EA, Jiang N, Hersam MC, Van Duyne RP. (2014) Recent Advances in Tip-Enhanced Raman Spectroscopy. *The Journal of Physical Chemistry Letters* 5 (18): 3125-3130.

Stark H, Oskoui P. (1989) High-resolution image recovery from image-plane arrays, using convex projections. *J. Opt. Soc. Am. A* 6 (11): 1715-1726.

Stender AS, Marchuk K, Liu C, Sander S, Meyer MW, Smith EA, Neupane B, Wang G, Li J, Cheng J-X, Huang B, Fang N. (2013) Single Cell Optical Imaging and Spectroscopy. *Chemical Reviews* 113 (4): 2469-2527.

Stone H, Orchard M, Ee-Chien C. (1999) Subpixel registration of images. *Proc. Signals, Systems, and Computers, 1999. Conference Record of the Thirty-Third Asilomar Conference on*, 2:1446-1452 vol.1442.

Stranahan SM, Willets KA. (2010) Super-resolution Optical Imaging of Single-Molecule SERS Hot Spots. *Nano Letters* 10 (9): 3777-3784.

Strobbia P, Languirand E, Cullum BM. (2015) Recent advances in plasmonic nanostructures for sensing: a review. *OPTICE* 54 (10): 100902-100902.

Sydor AM, Czymmek KJ, Puchner EM, Mennella V. (2015) Super-Resolution Microscopy: From Single Molecules to Supramolecular Assemblies. *Trends in Cell Biology* 25 (12): 730-748.

Szmacinski H, Toshchakov V, Piao W, Lakowicz J. (2013) Imaging of Protein Secretion from a Single Cell Using Plasmonic Substrates. *BioNanoSci.* 3 (1): 30-36.

Tachikawa T, Yamashita S, Majima T. (2011) Evidence for Crystal-Face-Dependent TiO<sub>2</sub> Photocatalysis from Single-Molecule Imaging and Kinetic Analysis. *Journal of the American Chemical Society* 133 (18): 7197-7204.

Tian X, Guo J, Tian Y, Tang H, Yang W. (2014) Modulated fluorescence properties in fluorophore-containing gold nanorods@mSiO<sub>2</sub>. RSC Advances 4 (18): 9343-9348.

Toma M, Knoll W, Dostalek J. (2012) Bragg-Scattered Surface Plasmon Microscopy: Theoretical Study. Plasmonics 7 (2): 293-299.

Tripathi A, Emmons ED, Guicheteau JA, Christesen SD, Wilcox PG, Emge DK, Fountain AW. (2010) Trace explosive detection in fingerprints with Raman chemical imaging. Proc. SPIE Defense, Security, and Sensing, 7665:76650N. SPIE

Tripathi A, Jabbour RE, Guicheteau JA, Christesen SD, Emge DK, Fountain AW, Bottiger JR, Emmons ED, Snyder AP. (2009) Bioaerosol Analysis with Raman Chemical Imaging Microspectroscopy. Analytical Chemistry 81 (16): 6981-6990.

Tsai R, Huang T. (1984) Multiframe image restoration and registration. Advances in Computer Vision and Image Processing 1: 317 - 339.

Vandewalle P, Susstrunk S, Vetterli M. (2006) A Frequency Domain Approach to Registration of Aliased Images with Application to Super-resolution. EURASIP Journal on Advances in Signal Processing 2006 (1): 071459.

Walt DR. (2010) Fibre optic microarrays. Chemical Society Reviews 39 (1): 38-50.

Wang D, Neyenhuis B, de Miranda MHG, Ni KK, Ospelkaus S, Jin DS, Ye J. (2010) Direct absorption imaging of ultracold polar molecules. *Physical Review A* 81 (6): 061404.

Wang J-F, Li H-J, Zhou Z-Y, Li X-Y, Liu J, Yang H-Y. (2010) Tunable surface-plasmon-resonance wavelength of silver island films. *Chin. Phys. B* 19 (11): 117310/117311-117310/117317.

Weber ML, Litz JP, Masiello DJ, Willets KA. (2012) Super-Resolution Imaging Reveals a Difference between SERS and Luminescence Centroids. *ACS Nano* 6 (2): 1839-1848.

Weber-Bargioni A, Schwartzberg A, Cornaglia M, Ismach A, Urban JJ, Pang Y, Gordon R, Bokor J, Salmeron MB, Ogletree DF, Ashby P, Cabrini S, Schuck PJ. (2011) Hyperspectral Nanoscale Imaging on Dielectric Substrates with Coaxial Optical Antenna Scan Probes. *Nano Letters* 11 (3): 1201-1207.

Weiner J. (2009) The physics of light transmission through subwavelength apertures and aperture arrays. *Reports on Progress in Physics* 72 (6): 064401.

Weiss PS. (2014) Nobel Prizes for Super-Resolution Imaging. *ACS Nano* 8 (10): 9689-9690.

Weisstein EW. Gaussian Function.

<http://mathworld.wolfram.com/GaussianFunction.html>

White DJ, Mazzolini AP, Stoddart PR. (2008) First-approximation simulation of dopant diffusion in nanostructured silica optical fibres. *Photonics and Nanostructures - Fundamentals and Applications* 6 (2): 167-177.

Willems KA, Stranahan SM, Weber ML. (2012) Shedding Light on Surface-Enhanced Raman Scattering Hot Spots through Single-Molecule Super-Resolution Imaging. *The Journal of Physical Chemistry Letters* 3 (10): 1286-1294.

Willems KA, Stranahan SM. (2012) Super-resolution imaging of diffusing analyte in surface-enhanced Raman scattering hot-spots, 8228:82280P-82280P-82288.

Willems KA. (2013) Super-resolution imaging of interactions between molecules and plasmonic nanostructures. *Physical Chemistry Chemical Physics* 15 (15): 5345-5354.

Willems KA. (2014) Super-resolution imaging of SERS hot spots. *Chemical Society Reviews* 43 (11): 3854-3864.

Wolfe J, Exline DL. (2003) Characterization of condom lubricant components using Raman spectroscopy and Raman chemical imaging. *J Forensic Sci* 48 (5): 1065-1074.

Wong C, Olivo M. (2014) Surface Plasmon Resonance Imaging Sensors: A Review. *Plasmonics* 9 (4): 809-824.

Wu C, Bull B, Szymanski C, Christensen K, McNeill J. (2008) Multicolor Conjugated Polymer Dots for Biological Fluorescence Imaging. *ACS Nano* 2 (11): 2415-2423.

Xu H, Aizpurua J, Käll M, Apell P. (2000) Electromagnetic contributions to single-molecule sensitivity in surface-enhanced Raman scattering. *Physical Review E* 62 (3): 4318-4324.

Yang J, Huang T. (2011) Image Super-Resolution: Historical Overview and Future Challenges. In *Super-Resolution Imaging*, ed. P Milanfar. Boca Raton, FL: CRC Press, 1-33 pp.

Youla D. (1978) Generalized Image Restoration by the Method of Alternating Orthogonal Projections. *IEEE Transactions on Circuits and Systems* 25 (9): 694-702.

Zapata F, Ortega-Ojeda FE, García-Ruiz C. (2017) Revealing the location of semen, vaginal fluid and urine in stained evidence through near infrared chemical imaging. *Talanta* 166 (Supplement C): 292-299.

Zitova B, Flusser J. (2003) Image registration methods: a survey. *Image and Vision Computing* 21 (11): 977 - 1000.

